



Computer Aided Diagnosis system for prostatic biopsy guidance and follow-up fusing multi-modal imaging.

Guillaume Lemaître

LE2I - ViCOROB

Université de Bourgogne - Universitat de Girona

Supervised by:

Jordi Freixenet Bosch (ViCOROB - UdG), Fabrice Mériadeau (CISIR - UTP)

Robert Marí Marly (ViCOROB - UdG), Paul Michael Walker (LE2I - UBFC)

A thesis submitted for the degree of

Philosophiae Doctor (PhD)

November 2016

Work submitted to the Universitat de Girona and Université de Bourgogne in partial
fulfillment of the requirements for the degree of Doctor of Philosophy

Reviewers:

Su Ruan, Professor at Université de Rouen - LITIS

Reyer Zwiggelaar Ir, Professor at Aberystwyth University - Vision, Graphics, and Visualisation Group

Soumya Ghose, Research Associate at Case Western Reserve University

Day of the defense: December 2016

Signature from head of PhD committee:

Abstract

Put your abstract or summary here, if your university requires it.

To ...

Acknowledgements

I would like to acknowledge the thousands of individuals who have coded for the LaTeX project for free. It is due to their efforts that we can generate professionally typeset PDFs now.

Contents

List of Abbreviations	vi
List of Figures	xi
List of Tables	xiii
1 Introduction	1
1.1 Prostate anatomy	1
1.2 Prostate carcinoma	2
1.3 prostate cancer (CaP) screening and imaging techniques	3
1.4 Computer-aided systems for CaP	5
1.5 Research motivation	7
1.6 Thesis outline	7
2 MRI Principles and Imaging Techniques	9
2.1 MRI principles	9
2.2 MRI imaging techniques	9
2.2.1 T ₂ -W MRI	11
2.2.2 T ₂ map	11
2.2.3 DCE magnetic resonance imaging (MRI)	14
2.2.4 DW MRI	16
2.2.5 ADC Map	18
2.2.6 MRSI	20

CONTENTS

3 Review of CADe and CADx for CaP	23
3.1 Image regularization framework	25
3.1.1 Pre-processing	25
3.1.2 Segmentation	39
3.1.3 Registration	44
3.2 Image classification framework	50
3.2.1 Computer-aided detection (CADe): region of interests (ROIs) detection/selection	50
3.2.2 Computer-aided diagnosis (CADx): Feature detection	52
3.2.2.1 Image-based features	52
3.2.2.2 Dynamic contrast-enhanced (DCE)-based features .	57
3.2.2.3 Magnetic resonance spectroscopy imaging (MRSI)-based features	60
3.2.3 CADx: Feature selection and feature extraction	61
3.2.3.1 Feature selection	61
3.2.3.2 Feature extraction	64
3.2.4 CADx: Classification	67
3.2.4.1 Classifier	67
3.2.5 Model validation	81
3.2.6 Evaluation measure	82
3.3 Discussion	84
3.3.1 Results reported	84
3.3.2 Comparison	85
3.3.3 General discussion	87
4 Materials	89
5 Normalization/Standardization of T2W-MRI and DCE-MRI Images	91
5.1 Normalization of T ₂ Weighted (T ₂ -W)-MRI images	91
5.1.1 Methodology	92
5.1.1.1 Normalization using Rician <i>a priori</i>	92

CONTENTS

5.1.1.2	Normalization using generative models in functional data analysis	94
5.1.2	Experiments and results	95
5.1.2.1	Experiments	95
5.1.2.2	Results	96
5.1.3	Discussion and conclusion	99
5.2	Normalization of DCE-MRI images	99
5.2.1	Methodology	101
5.2.1.1	Normalization of DCE-MRI images	101
5.2.1.2	Quantification of DCE-MRI	106
5.2.2	Experiment and results	111
5.2.2.1	Goodness of model fitting	112
5.2.2.2	Detection of CaP using pharmacokinetic parameters	113
5.2.2.3	Classification of the entire enhanced DCE-MRI signal	116
5.2.3	Discussion and conclusion	116
References		119

CONTENTS

List of Abbreviations

ACM active contour model

ADC apparent diffusion coefficient

AIF arterial input function

ASM active shape model

AUC area under the curve

BPH benign prostatic hyperplasia

CAD computer-aided detection and diagnosis

CADe computer-aided detection

CADx computer-aided diagnosis

CaP prostate cancer

CART classification and regression tree

CG central gland

Chap. Chapter

CMI combined mutual information

CSE chemical shift effect

CZ central zone

DCE dynamic contrast-enhanced

DCT discrete cosine transform

DFT discrete fourier transform

DW diffusion weighted

EES extravascular-extracellular space

Eq. equation

ERSSPC European Randomized Study of Screening for Prostate Cancer

ES Evolution Strategy

ETL Echo Train Length

Fig. figure

FOV field of view

FROC free-response receiver operating characteristic

FSE Fast Spin-Echo

GS Gleason score

***g*-scale** generalized scale

HOG histogram of oriented gradient

ID3 iterative dichotomiser 3

ITK Insight Segmentation and Registration Toolkit

***k*-CV** *k*-fold cross-validation

***k*-NN** *k*-nearest neighbour

LBP local binary pattern

LDA linear discriminant analysis

LLE locally linear embedding

LOOCV leave-one-out cross-validation

LOPO CV Leave-One-Patient-Out Cross-Validation

CONTENTS

MANTRA multi-attribute non-initializing texture reconstruction based active shape model

MAP maximum *a posteriori*

MI mutual information

ML maximum likelihood

mp-MRI multiparametric MRI

MRF Markov random field

MRI magnetic resonance imaging

mRMR minimum redundancy maximum relevance

MRSI magnetic resonance spectroscopy imaging

MSE mean squared error

NMR nuclear magnetic resonance

PCA principal components analysis

PDF probability density function

PLCO Prostate Lung Colorectal and Ovarian

PSA prostate-specific antigen

PUN Phenomenological Universalities

PZ peripheral zone

QDA quadratic discriminant analysis

RBF radial basis function

RF Random Forest

RMS Root Mean Square

RMSD Root-Mean-Square Deviation

ROC receiver operating characteristic

ROI region of interest

RVM relevant vector machine

Sect. section

SI signal intensity

SNR signal-to-noise

SRSF Square-Root Slope Function

STAPLE simultaneous truth and performance level estimation

SVD singular value decomposition

SVM support vector machines

T₁-W T₁ Weighted

T₂-W T₂ Weighted

TE echo time

TPS thin plate spline

TR repetition time

TRUS transrectal ultrasound

TZ transitional zone

US ultrasound

WERITAS weighted ensemble of regional image textures for active shape model segmentation

CONTENTS

List of Figures

1.1	Sagittal anatomy of prostate.	1
1.2	Prostate anatomy.	2
2.1	computer-aided detection and diangosis (CAD) framework using multiparametric MRI images.	12
2.2	Rendering of T_2 -W-MRI prostate images.	13
2.3	Enhancement of DCE-MRI signal.	14
2.4	Example of diffusion weighted (DW)-MRI and DCE map.	16
2.5	Illustration of healthy and cancerous MRSI spectrum.	19
3.1	Illustration of a Gaussian and Rayleigh distributions.	27
3.2	Inhomogeneity artefacts due to perturbation of the endorectal coil. .	29
3.3	Example of linear mapping by parts as proposed by [171].	33
3.4	Illustration of the two organs used by [166, 167] to normalize T_2 -W and T_1 Weighted (T_1 -W) MRI images.	34
3.5	Illustration of phase malignant in an MRSI spectra.	35
3.6	Illustration of water and fat residues in MRSI signal after supression during acquisition.	36
3.7	Illustration of frequency misalignment in an MRSI spectra.	38
3.8	Regsitration framework.	44
3.9	Difference observed in joint histogram between aligned and misaligned images.	47
3.10	Illustration of four different Gabor filters.	53
3.11	Semi-quantitative features used for DCE-MRI.	59

LIST OF FIGURES

3.12	Representation of the capabilities of the probabilistic boosting tree algorithm to split at each node of the tree the positive and negative samples.	73
3.13	Representation of a neural network of the multilayer perceptron family.	78
3.14	Representation of a neural network of the probabilistic neural network family.	79
5.1	Visual evaluation of the goodness of fitting using Rician and Gaussian distribution.	93
5.2	Qualitative evaluation by visual inspection of the alignment of the probability density function (PDF)s for the full prostate and the CaP. .	97
5.3	Spectral evaluation using principal components analysis (PCA) decomposition: (a) evaluation considering the full prostate, (b) evaluation considering only the CaP.	98
5.4	Illustration of the inter-patient variations in 17 different patients, using the PDF representation.	101
5.5	Illustration of the heatmap in DCE-MRI images.	102
5.6	Illustration of the estimator found using the shortest-path through the graph.	103
5.7	Illustration of the correction of the time offset and the data dispersion. .	105
5.8	Illustration of the segmentation of the area used to determine the AIF.	107
5.9	ROC analysis using a RF classifier with and without normalization DCE-MRI data for different pharmacokinetic models.	113
5.10	ROC analysis using the entire DCE-MRI signal with and without normalization in conjunction with a RF classifier.	115

List of Tables

2.1	Overview of the features associated with each MRI modality used for medical diagnosis by radiologists. Acronyms: prostate cancer (CaP) - signal intensity (SI) - Gleason score (GS).	10
3.1	Overview of the different studies reviewed with their main characteristics. Acronyms: number (#) - image regularization (Img. Reg.).	26
3.2	Overview of the pre-processing methods used in CAD systems. . . .	40
3.3	Overview of the segmentation methods used in CAD systems. . . .	41
3.4	Classification of the different registration methods used in the CAD systems reviewed. Acronyms: gradient descent (GD), Nelder-Mead (NM).	49
3.5	Overview of the CADe strategies employed in CAD systems.	50
3.6	The fourteen statistical features for texture analysis commonly computed from the gray level co-occurrence matrix p as presented by [88].	55
3.7	Parameters used as features for a DCE semi-quantitative analysis in CAD systems.	58
3.8	Overview of the feature selection and extraction methods used in CAD systems.	62
3.9	Overview of the classifiers used in CAD systems.	68
3.10	Overview of the model validation techniques used in CAD systems.	81
3.11	Overview of the evaluation metrics used in CAD systems.	82
5.1	Coefficient of determination R^2 (i.e., μ ($\pm\sigma$)), while fitting data with the different quantification models.	112

LIST OF TABLES

5.2 AUC (i.e., μ ($\pm\sigma$)) for each individual pharmacokinetic parameter using a RF classifier.	114
--	-----

Chapter 1

Introduction

1.1 Prostate anatomy

The prostate is an exocrine gland of the male reproductive system having an inverted pyramidal shape, which is located below the bladder and in front of the rectum as shown in Fig. 1.1. It measures approximately three centimetres in height by two and half centimetres in depth and its weight is estimated to be between seven and sixteen grams for an adult [123]. The prostate size increases at two distinct stages during physical development: initially at puberty to reach its normal size, then again after sixty years of age leading to benign prostatic hyperplasia (BPH) [179].

A zonal classification of the prostate, depicted in Fig. 1.2, was suggested by

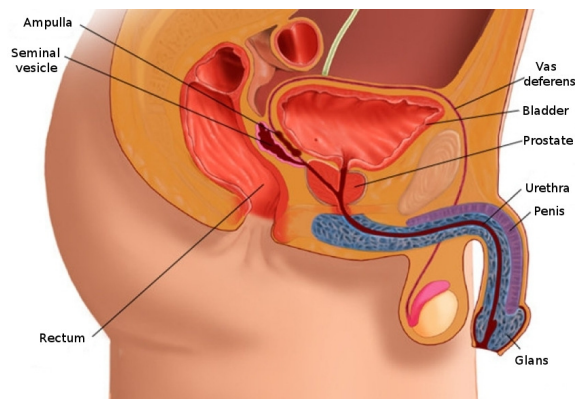
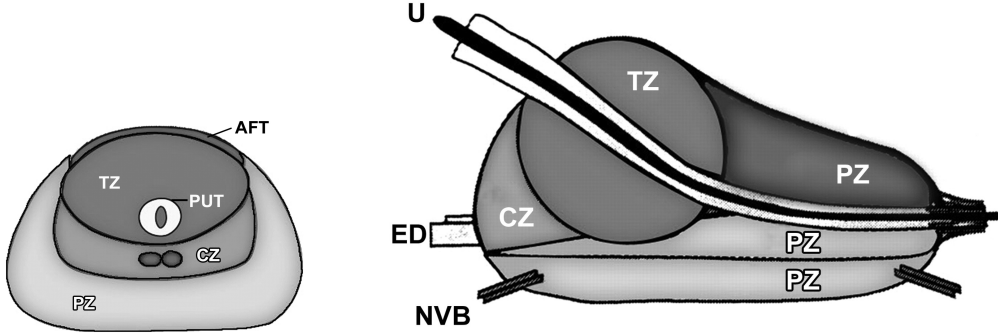


Figure 1.1: Sagittal anatomy scheme of the male reproductive system.

1. INTRODUCTION



(a) Transverse anatomy of the prostate.

(b) Sagittal anatomy of the prostate.

Figure 1.2: Prostate anatomy with division in different zones. *AFT*: anterior fibromuscular tissue, *CZ*: central zone, *ED*: ejaculatory duct, *NVB*: neurovascular bundle, *PUT*: tissue, *PZ*: peripheral zone, *U*: urethra, *TZ*: transitional zone, *B*: base, *M*: median, *A*: apex (copyright by [41]).

McNeal [156]. Subsequently, this categorization was widely accepted in the literature [43, 96, 179, 256] and is used in all medical examinations (e.g., biopsy, MRI screening). The classification is based on dividing the gland into three distinct regions: (i) central zone (CZ) accounting for 20-25% of the whole prostate gland, (ii) transitional zone (TZ) standing for 5% and (iii) peripheral zone (PZ) representing the 70%. In MRI images, tissues of CZ and TZ are difficult to distinguish and are usually merged into a common region, denominated central gland (CG). As part of this classification, the prostate can be divided in three longitudinal portions depicted in Fig. 1.2(b): (i) base, (ii) median gland and (iii) apex.

1.2 Prostate carcinoma

Prostate cancer (CaP) has been reported on a worldwide scale to be the second most frequently diagnosed cancer of men accounting for 13.6% [64]. Statistically, in 2008, the number of new diagnosed cases was estimated to be 899,000 with no less than 258,100 deaths [64]. In United States, aside from skin cancer, CaP was

1.3 CaP screening and imaging techniques

declared to be the most commonly diagnosed cancer among men, implying that approximately one in six men will be diagnosed with CaP during their lifetime and one in thirty-six will die from this disease causing CaP to be the second most common cause of cancer death among men [216], [8].

Despite active research to determine the causes of prostate cancer, a fuzzy list of risk factors has arisen [7]. The etiology was linked to the following factors [7]: (i) family history [77, 225], (ii) genetic factors [1, 11, 67], (iii) race-ethnicity [77, 93], (iv) diet [5, 77, 148], and (v) obesity [77, 200]. This list of risk factors alone cannot be used to diagnose CaP and in this way, screening enables early detection and treatment.

CaP growth is characterized by two main types of evolution [226]: slow-growing tumours, accounting for up to 85 % of all CaPs [146], progress slowly and usually stay confined to the prostate gland. For such cases, treatment can be substituted with active surveillance. In contrast, the second variant of CaPs develops rapidly and metastasises from prostate gland to others organs, primarily the bones [174]. Bone metastases, being an incurable disease, significantly affects the morbidity and mortality rate [272]. Hence, the results of the surveillance have to be trustworthy in order to distinguish aggressive from slow-growing CaP.

CaP is more likely to come into being in specific regions of the prostate. In that respect, around 70-80 % of CaPs originate in PZ whereas 10-20 % in TZ [34, 157, 224]. Only about 5 % of CaPs occur in CZ [44, 157]. However, those cancers appear to be more aggressive and more likely to invade other organs due to their location [44].

1.3 CaP screening and imaging techniques

Current CaP screening consists of three different stages. First, prostate-specific antigen (PSA) control is performed to distinguish between low and high risk CaP. Then, for confirmation, samples are taken during prostate biopsy and finally analysed to evaluate the prognosis and the stage of CaP. In this section, we present a detailed description of the current screening as well as its drawbacks.

Since its introduction in mid-1980s, PSA is widely used for CaP screening [62]. A higher-than-normal level of PSA can indicate an abnormality of the prostate

1. INTRODUCTION

either as a BPH or a cancer [92]. However, other factors can lead to an increased PSA level such as prostate infections, irritations, a recent ejaculation or a recent rectal examination [179]. PSA can be found in the bloodstream in two different forms: free PSA (about 10%), and linked to another protein (about 90%). A level of PSA higher than 10 ng.mL^{-1} is considered to be at risk [179]. If the PSA level is between 10 ng.mL^{-1} and 4 ng.mL^{-1} , the patient is considered as suspicious [17]. In that case, the ratio of free PSA to total PSA is computed; if the ratio is higher than 15%, the case is considered as pathological [179].

A transrectal ultrasound (TRUS) biopsy is carried out for cases which are considered as pathological. At least six different samples are taken randomly from the right and left parts of three different zones: apex, median and base. These samples are further evaluated using the Gleason grading system [79]. The scoring scheme to characterize the biopsy sample is composed of five different patterns which correspond to grades ranging from 1 to 5. Higher grades are associated with poor prognosis [61]. Then, in the Gleason system, two scores are assigned corresponding to (i) the grade of the most present tumour pattern, and (ii) the grade of the second most present tumour pattern [61]. A higher GS indicates a more aggressive tumour [61]. Also, it should be noted that biopsy is an invasive procedure which can result in serious infection or urine retention [42, 87].

Although PSA screening has been shown to improve early detection of CaP [42], its lack of reliability motivates further investigations using MRI-CAD. Two reliable studies, carried out in the United States [12] and in Europe [98, 211], have attempted to assess the impact of early detection of CaP, with diverging outcomes [42, 90]. The study carried out in Europe¹ concluded that PSA screening reduces CaP-related mortality by 21-44% [98, 211], while the American² trial found no such effect [12]. However, both studies agree that PSA screening suffers from low specificity, with an estimated rate of 36 % [210]. Both studies also agree that over-treatment is an issue: decision making regarding treatment is further complicated by difficulties in evaluating the aggressiveness and progression of CaP [55].

¹The European Randomized Study of Screening for Prostate Cancer (ERSSPC) started in the 1990s in order to evaluate the effect of PSA screening on mortality rate.

²The Prostate Lung Colorectal and Ovarian (PLCO) cancer screening trial is carried out in the United States and intends to ascertain the effects of screening on mortality rate.

Hence, new screening methods should be developed with improved specificity of detection as well as more accurate risk assessment (aggressiveness and progression). Current research is focused on identifying new biological markers to replace PSA-based screening [25, 28, 165]. Until such research comes to fruition, these needs can be met through active-surveillance strategy using multi-parametric MRI techniques [92, 164]. An MRI-CAD system, which is an area of active research and forms the focus of this thesis, can be incorporated into this screening strategy allowing a more systematic and rigorous follow-up.

Another weakness of the current screening strategy lies in the fact that TRUS biopsy does not provide trustworthy results. Due to its “blind” nature, there is a chance of missing aggressive tumours or detecting microfocal “cancers”, which influences the aggressiveness-assessment procedure [168]. As a consequence, over-diagnosis is estimated at up to 30 % [84], while missing clinically significant CaP is estimated at up to 35 % [231]. In an effort to solve both issues, alternative biopsy approaches have been explored. MRI/ultrasound (US)-guided biopsy has been shown to outperform standard TRUS biopsy [54]. There, multimodal MRI images are fused with US images in order to improve localization and aggressiveness assessment to carry out biopsies. Human interaction plays a major role in biopsy sampling which can lead to low repeatability; by reducing potential human errors at this stage, the CAD framework can be used to improve repeatability of examination. CaP detection and diagnosis benefit from the use of CAD and MRI techniques.

In an effort to improve the current stage of CaP diagnosis and detection, this thesis is intended to provide a multiparametric MRI CAD system. MRI principles and its different modalities are presented in Chapter (Chap.) 2.

1.4 Computer-aided systems for CaP

During the last century, physicists have focused on constantly innovating in terms of imaging techniques assisting radiologists to improve cancer detection and diagnosis. However, human diagnosis still suffers from low repeatability, synonymous with erroneous detection or interpretations of abnormalities throughout clinical

1. INTRODUCTION

decisions [76, 86]. These errors are driven by two major causes [76]: observer limitations (e.g., constrained human visual perception, fatigue or distraction) and the complexity of the clinical cases themselves, for instance due to unbalanced data (number of healthy cases more abundant than malignant cases) or overlapping structures.

Computer vision has given rise to many promising solutions, but, instead of focusing on fully automatic computerized systems, researchers have aimed at providing computer image analysis techniques to aid radiologists in their clinical decisions [76]. In fact, these investigations brought about both concepts of CADe and CADx grouped under the acronym CAD. Since those first steps, evidence has shown that CAD systems enhance the diagnosis performance of radiologists. Chan *et al.* reported a significant 4 % improvement in breast cancer detection [36], which has been confirmed in later studies [53]. Similar conclusions were drawn in the case of lung nodule detection [129], colon cancer [185] and CaP as well [86]. Chan *et al.* [36] also hypothesized that CAD systems will be even more efficient assisting inexperienced radiologists than senior radiologists. That hypothesis was tested by Hambrock *et al.* [86] and was confirmed in case of CaP detection. In this particular study, inexperienced radiologists obtained equivalent performance to senior radiologists, both using CAD whereas the accuracy of their diagnosis was significantly poorer without CAD's help.

In contradiction with the aforementioned statement, CAD for CaP is a young technology due to the fact that is based on MRI [89]. Four distinct MRI modalities are employed in CaP diagnosis which were mainly developed after the mid-1990s: (i) T₂-W MRI [95], (ii) DCE MRI [97], (iii) MRSI [116] and (iv) DW MRI [208]. In addition, the increase of magnetic field strength (from 1.5 to 3 Tesla) and the development of endorectal coils, both improved image spatial resolution [230] needed to perform more accurate diagnosis. It is for this matter that the development of CAD for CaP is still lagging behind fields stated above.

This research is aimed at first, to provide an overview of the current state-of-the-art of CAD for CaP and later, according to the drawn conclusions, to propose a CAD which takes advantage of multiparametric MRI modalities. A review of the current proposed CAD for CaP is presented in Chap. 3.

1.5 Research motivation

1.6 Thesis outline

1. INTRODUCTION

Chapter 2

MRI Principles and Imaging Techniques

2.1 MRI principles

2.2 MRI imaging techniques

MRI provides promising imaging techniques to overcome the previous mentioned drawbacks. Unlike TRUS biopsy, MRI examination is a non-invasive protocol and has been shown to be the most acute and harmless technique available currently [247]. In this section, we review different MRI techniques developed for CaP detection and diagnosis. Features strengthening each modality, will receive particular attention together with their drawbacks. Commonly, these features form the basis for developing analytic tools and automatic algorithms. However, we refer the reader to Sect. ?? for more details on automatic feature detection methods since they are part and parcel of the CAD framework. Table 2.1 provides an overview of the following discussion.

Table 2.1: Overview of the features associated with each MRI modality used for medical diagnosis by radiologists. Acronyms: prostate cancer (CaP) - signal intensity (SI) - Gleason score (GS).

Modality	Significant features	CaP	Healthy tissue	GS correlation
T ₂ -W MRI	SI Shape	low-SI in PZ [96] round or ill-defined mass in PZ [95]	intermediate to high-SI in PZ [96]	+ [269]
	SI Shape	low-SI in CG [4, 17] homogeneous mass with ill-defined edges in CG [4, 17]	low-SI in CG [4, 17]	
T ₂ map	SI	low-SI [75, 135]	intermediate to high-SI [75, 135]	+ [135, 136, 143]
DCE MRI	Semi-quantitative features [254]: – wash-in – wash-out – integral under the curve – maximum signal intensity – time-to-peak enhancement	faster faster higher higher faster	slower slower lower lower slower	0 0 0 0 0
	Quantitative features (Tofts' parameters [240]): – k_{ep} – K^{trans}	higher higher	lower lower	0 0
DW MRI	SI	higher-SI [17, 101]	lower-SI [17, 101]	+
ADC map	SI	low-SI [17]	high-SI [17]	+ [85, 103, 184]
MRSI	Metabolites: Citrate (2.64 ppm) [253]	lower concentration [16, 49, 248]	higher concentration [16, 49, 248]	+ [78]
	Choline (3.21 ppm) [253]	higher concentration [16, 49, 248]	lower concentration [16, 49, 248]	0 [78]
	Spermine (3.11 ppm) [253]	lower concentration [16, 49, 248]	higher concentration [16, 49, 248]	+ [78]

2.2.1 T_2 -W MRI

T_2 -W MRI was the first MRI-modality used to perform CaP diagnosis using MRI [95]. Nowadays, radiologists make use of it for CaP detection, localization and staging purposes. This imaging technique is well suited to render zonal anatomy of the prostate [17].

This modality relies on a sequence based on setting a long repetition time (TR), reducing the T_1 effect in nuclear magnetic resonance (NMR) signal measured, and fixing the echo time (TE) to sufficiently large values in order to enhance the T_2 effect of tissues. Thus, PZ and CG tissues are well perceptible in these images. The former is characterized by an intermediate/high-SI while the latter is depicted by a low-SI [96]. An example of a healthy prostate is shown in Fig. 2.2(a).

In PZ, round or ill-defined low-SI masses are synonymous with CaPs [95] as shown in Fig. 2.2(b). Detecting CaP in CG is more challenging. In fact both normal CG tissue and malignant tissue, have a low-SI in T_2 -W MRI reinforcing difficulties to distinguish between them. However, CaPs in CG appear often as homogeneous mass possessing ill-defined edges with lenticular or “water-drop” shapes [4, 17] as depicted in Fig. 2.2(c).

CaP aggressiveness was shown to be inversely correlated with SI. Indeed, CaPs assessed with a GS of 4-5 implied lower SI than the one with a GS of 2-3 [269].

In spite of the availability of these useful and encouraging features, the T_2 -W modality lacks reliability [92, 113]. Sensitivity is affected by the difficulties in detecting cancers in CG [113] while specificity rate is highly affected by outliers [17]. In fact, various conditions emulate patterns of CaP such as BPH, post-biopsy haemorrhage, atrophy, scars and post-treatment [17, 50, 96, 196, 208]. These issues can be partly addressed using more innovative and advanced modalities.

2.2.2 T_2 map

As previously mentioned, T_2 -W MRI modality shows low sensitivity. Moreover, T_2 -W MRI images are a composite of multiple effects [89]. However, T_2 values alone have been shown to be more discriminative [143] and highly correlated with citrate concentration, a biological marker in CaP [135, 136].

2. MRI PRINCIPLES AND IMAGING TECHNIQUES

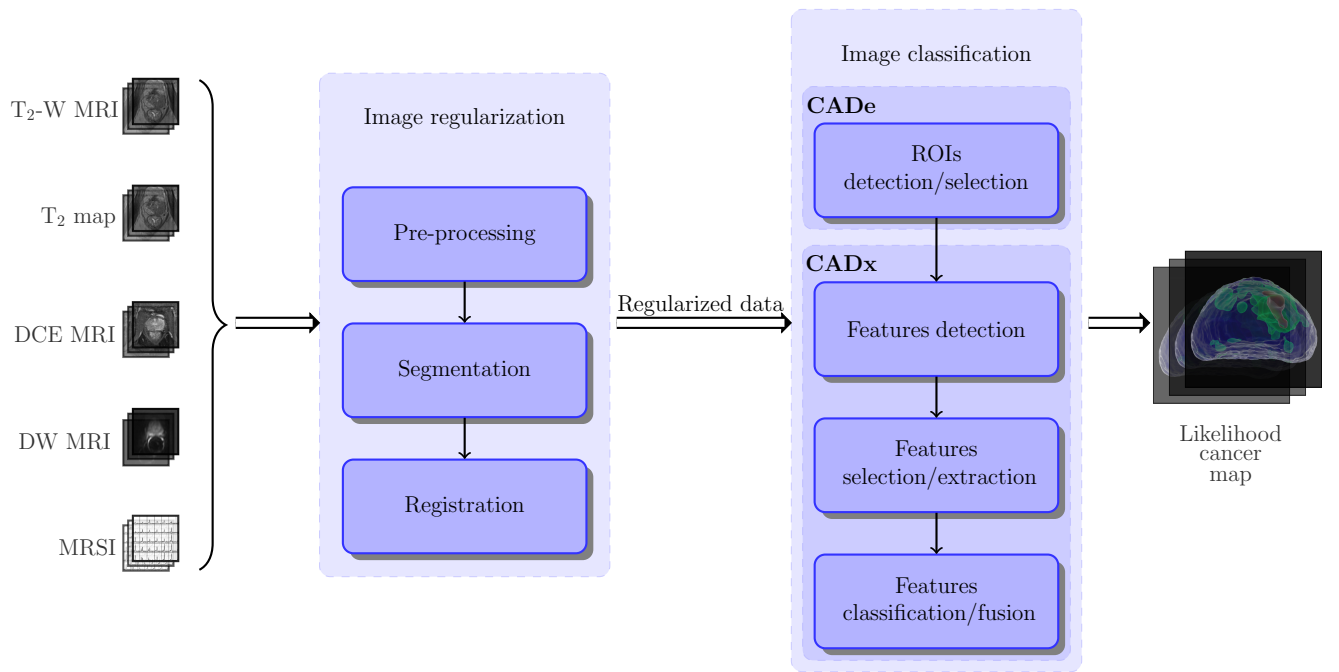


Figure 2.1: CAD framework using MRI images. Multiparametric MRI images are provided as inputs. These data arise from heterogeneous sources and need to be regularized. Some studies do not consider this stage as mandatory and do not implement or only partly those processes (see Tab. 3.1). A pre-processing stage is usually applied to standardize the intensity of images, reduce noise and artefacts. Then, in the image set, the prostate organ has to be segmented to focus the next processing stages only on that particular ROI. Moreover, prostate location can vary depending of the modality chosen. Therefore, the images are registered so that all segmented images will be in the same reference frame. Once the image regularisation performed, image classification can be carried out. First, a strategy defining ROIs to focus on is decided. Then, distinctive features are extracted before to be post-processed to select the most salient features. Finally, these salient features will feed a classifier previously trained which will provide a likelihood cancer map associated with either CaP detection or diagnosis.



(a) T₂-W-MRI slice of an healthy prostate acquire with a 1.5 Tesla MRI. The blue contour represents the CG while the PZ corresponds to the green contour.

(b) T₂-W-MRI slice of a prostate with a CaP highlighted in the PZ using a 3.0 Tesla MRI scanner.

(c) T₂-W-MRI slice of a prostate with a CaP highlighted in the CG using a 3.0 Tesla MRI scanner.

Figure 2.2: Rendering of T₂-W-MRI prostate image with both 1.5 and 3.0 Tesla MRI scanner.

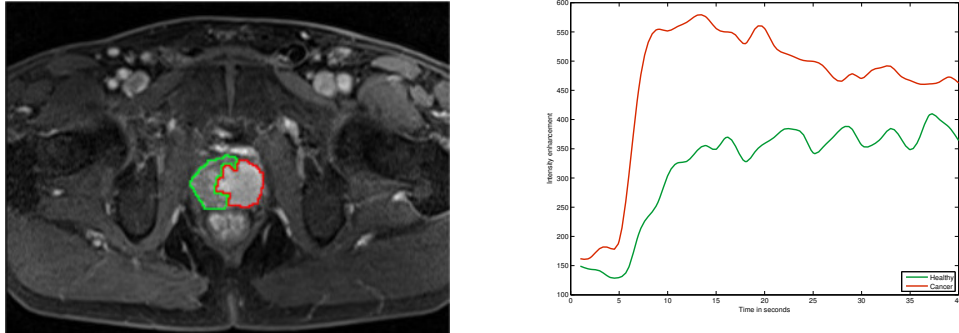
T₂ values are computed using the characteristics of transverse relaxation which is formalized as:

$$M_{x,y}(t) = M_{x,y}(0) \exp \left(-\frac{t}{T_2} \right) , \quad (2.1)$$

where $M_{x,y}(0)$ is the initial value of $M_{x,y}(t)$ and T_2 is the relaxation time. By rearranging Eq. 2.1, T_2 map is computed performing a linear fitting on the model in Eq. 2.2 using several TE, $t = \{TE_1, TE_2, \dots, TE_m\}$.

$$\ln \left[\frac{M_{x,y}(t)}{M_{x,y}(0)} \right] = -\frac{t}{T_2} . \quad (2.2)$$

The Fast Spin-Echo (FSE) sequence has been shown to be particularly well suited in order to build a T_2 map and obtain accurate T_2 values [134]. Similar to T₂-W MRI, T_2 values associated with CaP are significantly lower than those of healthy tissues [75, 135].



(a) T₁-W-MRI image where the cancer is delimited by the red contour. The green area was still not invaded by the CaP

(b) Enhancement curve computed during the DCE-MRI analysis. The red curve is typical from CaP cancer while the green curve is characteristic of healthy tissue.

Figure 2.3: Illustration of typical enhancement signal observed in DCE-MRI analysis collected with a 3.0 Tesla MRI scanner.

2.2.3 DCE MRI

DCE MRI is an imaging technique which exploits the vascularity characteristic of tissues. Contrast media, usually gadolinium-based, is injected intravenously into the patient. The media extravasates from vessels to extravascular-extracellular space (EES) and is released back into the vasculature before being eliminated by the kidneys [82]. Furthermore, the diffusion speed of the contrast agent may vary due to several parameters: (i) the permeability of the micro-vessels, (ii) their surface area and (iii) the blood flow [177].

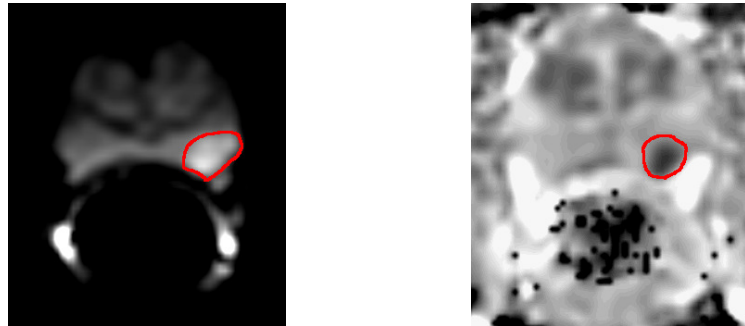
Healthy PZ is mainly made up of glandular tissue, around 70 % [41], which implies a reduced interstitial space restricting exchanges between vessels and EES [31, 249]. Normal CG has a more disorganized structure, composed of mainly fibrous tissue [41, 92], which facilitates the arrival of the contrast agent in EES [250]. To understand the difference between contrast media kinetic in malignant tumours and the two previous behaviours mentioned, one has to focus on the process known as angiogenesis [33]. In order to ensure growth, malignant tumours produce and release angiogenic promoter substances [33]. These molecules stimulate the creation of new vessels towards the tumour [33]. However, the new vessel networks in

tumours differ from those present in healthy tissue [82]. They are more porous due to the fact that their capillary walls have a large number of “openings” [41, 82]. In contrast to healthy cases, this increased vascular permeability results in increased contrast agent exchanges between vessels and EES [254].

By making use of the previous aspects, DCE MRI is based on an acquisition of a set of T₁-W MRI images over time. The Gadolinium-based contrast agent shortens T₁ relaxation time enhancing contrast in T₁-W MRI images. The aim is to post-analyse the pharmacokinetic behaviour of the contrast media concentration in prostate tissues [254]. The image analysis is carried out in two dimensions: (i) in the spatial domain on a pixel-by-pixel basis and (ii) in the time domain corresponding to the consecutive images acquired with the MRI. Thus, for each spatial location, a signal linked to contrast media concentration is measured as shown in Fig. 2.3(b) [240].

By taking the previous remarks regarding medical aspects and signal theory into account, CaPs are characterized by a signal having an earlier and faster enhancement and an earlier wash-out (cf., the rate of the contrast agent flowing out of the tissue) (see Fig. 2.3(b)) [254]. Three different approaches exist to analyse these signals with the aim of tagging them as corresponding to either normal or malignant tissues. Qualitative analysis is based on assessment of the signal shape [92].

Quantitative approaches consist of inferring pharmacokinetic parameter values [240]. Those parameters are part of mathematical-pharmacokinetic models which are directly based on physiological exchanges between vessels and EES. Several pharmacokinetic models were proposed such as the Kety model [111], the Tofts model [241] and mixed models [119, 223]. The last family of methods mixed both approaches and are grouped together under the heading of semi-quantitative methods. They rely on shape characterization using mathematical modelling to extract a set of parameters such as wash-in gradient, wash-out, integral under the curve, maximum signal intensity, time-to-peak enhancement and start of enhancement. These parameters will be discussed in a later section (see Fig. 3.11) [92, 254]. It was shown that semi-quantitative and quantitative methods improve localization of CaP when compared with qualitative methods [201]. Section ?? provides a full description of quantitative and semi-quantitative approaches.



(a) DW-MRI image acquired with a 1.5 Tesla MRI scanner. The cancer corresponds to the high SI region highlighted in red.

(b) ADC map computer after acquisition of DW-MRI images with a 1.5 Tesla MRI scanner. The cancer corresponds to the low SI region highlighted in red.

Figure 2.4: Illustration of DW-MRI and ADC map. The signal intensity corresponding to cancer are inversely correlated on these two types of imaging techniques.

DCE MRI combined with T_2 -W MRI has shown to enhance sensitivity compared to T_2 -W MRI alone [104, 112, 209, 273]. Despite this fact, DCE MRI possesses some drawbacks. Due to its “dynamic” nature, patient motions during the image acquisition lead to spatial misregistration of the image set [254]). Furthermore, it has been suggested that malignant tumours are difficult to distinguish from prostatitis located in PZ and BPH located in CG [92, 254]. These pairs of tissues tend to have similar appearances. Later studies have shown that CaPs in CG do not always manifest in homogeneous fashion. Indeed, tumours in this zone can present both hypo-vascularization and hyper-vascularization which illustrates the challenge of CaP detection in CG [250].

2.2.4 DW MRI

As previously mentioned in the introduction, DW MRI is the most recent MRI imaging technique aiming at CaP detection and diagnosis [208]. This modality exploits the variations in the motion of water molecules in different tissues [115, 122].

2.2 MRI imaging techniques

From a physiological point of view, the following facts can be claimed. On the one hand, PZ, as previously mentioned, is mainly glandular and tubular in structure allowing water molecules to move freely [41, 92]. On the other hand, CG is made up of muscular or fibrous tissue causing the motion of the water molecules to be more constrained and heterogeneous than in PZ [92]. Then, CaP growth leads to the destruction of normal glandular structure and is associated with an increase in cellular density [92, 115, 219]. Furthermore, these factors both have been shown to be inversely correlated with water diffusion [115, 219]: higher cellular density implies a restricted water diffusion. Thus, water diffusion in CaP will be more restricted than both healthy PZ and CG [92, 115].

From the NMR principle side, DW MRI sequence produces contrasted images due to variation of water molecules motion. The method is based on the fact that the signal in DW MRI images is inversely correlated to the degree of random motion of water molecules [101]. In fact, gradients are used in DW MRI modality to encode spatial location of nuclei temporarily. Simplifying the problem in only one direction, a gradient is applied in that direction, dephasing the spins of water nuclei. Hence, the spin phases vary along the gradient direction depending of the gradient intensity at those locations. Then, a second gradient is applied aiming at cancelling the spin dephasing. Thus, the immobile water molecules will be subject to the same gradient intensity as the initial one while moving water molecules will be subject to a different gradient intensity. Thus, spins of moving water molecules will stay dephased whereas spins of immobile water molecules will come back in phase. As a consequence, a higher degree of random motion results in a more significant signal loss whereas a lower degree of random motion is synonymous with lower signal loss [101]. Under these conditions, the MRI signal is measured as:

$$M_{x,y}(t, b) = M_{x,y}(0) \exp \left(-\frac{t}{T_2} \right) S_{\text{ADC}}(b) , \quad (2.3)$$

$$S_{\text{ADC}}(b) = \exp(-b \times \text{ADC}) , \quad (2.4)$$

where S_{ADC} refers to signal drop due to diffusion effect, ADC is the apparent diffusion coefficient and b is the attenuation coefficient depending only on gradient

2. MRI PRINCIPLES AND IMAGING TECHNIQUES

pulses parameters: (i) gradient intensity and (ii) gradient duration [121].

By using this formulation, image acquisition with a parameter $b = 0 \text{ s.mm}^{-2}$ corresponds to a T₂-W MRI acquisition. Then, increasing the attenuation coefficient b (cf., increase gradient intensity and duration) enhances the contrast in DW MRI images.

To summarize, in DW MRI images, CaPs are characterized by high-SI compared to normal tissues in PZ and CG as shown in Fig. 2.4(a) [17]. However, some tissues in CG can look similar to CaP with higher SI [17].

Diagnosis using DW MRI combined with T₂-W MRI has shown a significant improvement compared with T₂-W MRI alone and provides highly contrasted images [41, 178, 215]. As drawbacks, this modality suffers from poor spatial resolution and specificity due to false positive detection [41]. With a view to eliminate these drawbacks, radiologists are extracting quantitative maps from DW MRI. This imaging technique is presented next.

2.2.5 ADC Map

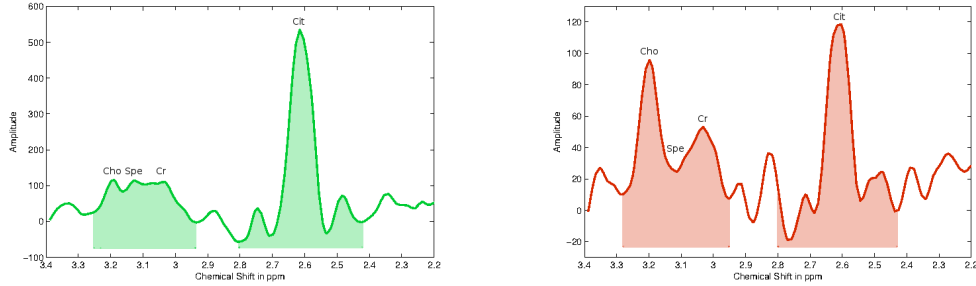
The NMR signal measured for DW MRI images is not only affected by diffusion as shown in Eq. (2.3). However, the signal drop (Eq. (2.4)) is formulated such that the only variable is the acquisition parameter b [121]. The ADC is considered as a “pure” diffusion coefficient and can be extracted to build a quantitative map.

From Eq. (2.3), it is clear that performing multiple acquisitions only varying b will not have any effect on the term $M_{x,y}(0) \exp\left(-\frac{t}{T_2}\right)$. Thus, Eq. (2.3) can be rewritten as:

$$S(b) = S_0 \exp(-b \times \text{ADC}) . \quad (2.5)$$

To compute the ADC map, a minimum of two acquisitions are necessary: (i) for $b_0 = 0 \text{ s.mm}^{-2}$ where the measured signal is equal to S_0 , and (ii) $b_1 > 0 \text{ s.mm}^{-2}$ (typically 1000 s.mm^{-2}). Then, the ADC map can be computed as:

$$\text{ADC} = -\frac{\ln\left(\frac{S(b_1)}{S_0}\right)}{b_1} . \quad (2.6)$$



(a) Illustration of an MRSI spectrum of an healthy voxel acquired with a 3.0 Tesla MRI.

(b) Illustration of an MRSI spectrum of a cancerous voxel acquired with a 3.0 Tesla MRI.

Figure 2.5: Illustration of an MRSI spectrum both healthy and cancerous voxel with a 3.0 Tesla MRI. The highlighted areas corresponds to the related concentration of the metabolites which is computed by integrating the area under each peak. Acronyms: Choline (Cho), Spermine (Spe), Creatine (Cr) and Citrate (Cit).

More accurate computation of the ADC map can be obtained by performing several acquisitions with different values for the parameter b and performing a semi-logarithmic linear fitting using the model presented in Eq. (2.5).

Regarding the appearance of the ADC maps, it was previously stated that by increasing the value of b , the signal of CaP tissue increases significantly. From Eq. (2.6), it can be shown that tissue appearance in the ADC map will be the inverse of DW MRI images. Then, CaP tissue is associated with low-SI whereas healthy tissue appears brighter as depicted in Fig. 2.4(b) [17].

Similar to the gain achieved by DW MRI, diagnosis using ADC map combined with T₂-W MRI significantly outperforms T₂-W MRI alone [41, 58]. Moreover, it has been shown that ADC is correlated with GS [85, 103, 184].

However, some tissues of the CG zone mimic CaP with low-SI [113] and image distortion can arise due to haemorrhage [41]. It has also been noted that a high variability of the ADC occurs between different patients making it difficult to define a static threshold to distinguish CaP from non-malignant tumours [41].

2. MRI PRINCIPLES AND IMAGING TECHNIQUES

2.2.6 MRSI

CaP induces metabolic changes in the prostate compared with healthy tissue. Thus, CaP detection can be carried out by tracking changes of metabolite concentration in prostate tissue. MRSI is an NMR-based technique which generates spectra of relative metabolite concentration in a ROI.

In order to track changes of metabolite concentration, it is important to know which metabolites are associated with CaP. To address this question, clinical studies identified three biological markers: (i) citrate, (ii) choline and (iii) polyamines composed mainly of spermine, and in less abundance of spermidine and putrescine [16, 49, 78].

Citrate is involved in the production and secretion of the prostatic fluid, and the glandular prostate cells are associated with a high production of citrate enabled by zinc accumulation by these same cells [49]. However, the metabolism allowing the accumulation of citrate requires a large amount of energy [49]. In contrast, malignant cells do not have high zinc levels leading to lower citrate levels due to citrate oxydation [49]. Furthermore, this change results in a more energy-efficient metabolism enabling malignant cells to grow and spread [49].

An increased concentration of choline is related to CaP [16]. Malignant cell development requires epigenetic mechanisms resulting in metabolic changes and relies on two mechanisms: DNA methylation and phospholipid metabolism which both result in choline uptake, explaining its increased level in CaP tissue [16]. Spermine is also considered as a biological marker in CaP [78, 248]. In CaP, reduction of the ductal volume due to shifts in polyamine homeostasis might lead to a reduced spermine concentration [248].

To determine the concentration of these biological markers, one has to focus on the MRSI modality. In theory, in presence of a homogeneous magnetic field, identical nuclei precesses at the same operating frequency known as the Larmor frequency [83]. However, MRSI is based on the fact that identical nuclei will slightly precess at different frequencies depending on the chemical environment in which they are immersed [83], a phenomenon known as the chemical shift effect (CSE) [179]. Given this property, metabolites can be identified and their concentrations can be determined. In this regard, the Fourier transform is used to obtain the

2.2 MRI imaging techniques

frequency spectrum of the NMR signal [83, 179]. In this spectrum, each peak is associated with a particular metabolite and the area under each peak corresponds to the relative concentration of this metabolite (see Fig. 2.5) [179].

Two different quantitative approaches are used to decide or whether not the spectra of a ROI is associated with CaP classified either as relative quantification or absolute quantification [124]. In relative quantification, the ratio of choline-polyamines-creatine to citrate is computed. The integral of the signal is computed from choline (cf., 3.21 ppm) to creatine (cf., 3.02 ppm) because the peaks in this region can be merged at clinical magnetic field strengths (see Fig. 2.5) [92, 248]. Considering the previous assumption that choline concentration rises and citrate concentration decreases in the presence of CaP, the ratio computed should be higher in malignant tissue than in healthy tissue.

Two different quantitative approaches are used to decide or not the spectra of a ROI is associated with CaP classified either as relative quantification or absolute quantification [124]. In relative quantification, the ratio of choline-polyamines-creatine to citrate is computed. The integral of the signal is computed from choline (cf., 3.21 ppm) to creatine (cf., 3.02 ppm) because the peaks in this region can be merged at clinical magnetic field strengths (see Fig. 2.5) [92, 248]. Considering the previous assumption that choline concentration rises and citrate concentration decreases in the presence of CaP, the ratio computed should be higher in malignant tissue than in healthy tissue.

In contrast with relative quantification, absolute quantification measures molar concentrations by normalizing relative concentrations using water as reference [124]. In this case, “true” concentrations are directly used to differentiate malignant from healthy tissue. However, this method is not commonly used as it requires an additional step of acquiring water signals, inducing time and cost acquisition constraints.

MRSI allows examination with high specificity and sensitivity compared to other MRI modalities [41]. Furthermore, it has been shown that combining MRSI with MRI improves detection and diagnosis performance [107, 207, 255]. Citrate and spermine concentrations are inversely correlated with the GS allowing us to distinguish low from high grade CaPs [78]. However, choline concentration does not provide the same properties [78].

2. MRI PRINCIPLES AND IMAGING TECHNIQUES

Unfortunately, MRSI also presents several drawbacks. First, MRSI acquisition is time consuming which prevents this modality from being used in daily clinical practise [17]. In addition, MRSI suffers from low spatial resolution due to the fact that signal-to-noise (SNR) is linked to the voxel size. However, this issue is addressed by developing new scanners with higher magnetic field strengths such as 7.5 T [78]. Finally, a high variability of the relative concentrations between patients was observed [41]. The same observation was made depending on the zones studied (cf., PZ, CG, base, mid-gland, apex) [124, 268]. Due to this variability, it is difficult to use a fixed thresholds in order to differentiate CaP from healthy tissue.

Chapter 3

Review of CADe and CADx for CaP

As previously mentioned in the introduction (see Sect. 1.4), CADs are developed to advise and backup radiologists in their tasks of CaP detection and diagnosis, but not to provide fully automatic decisions [76]. CADs can be divided into two different sub-groups either as CADe, with the purpose to highlight probable lesions in MRI images, or CADx, which focuses on differentiating malignant from non-malignant tumours [76]. Moreover, an intuitive approach, motivated by developing a framework combining detection-diagnosis, is to mix both CADe and CADx by using the output of the former mentioned as a input of the latter named. Although the outcomes of these two systems should differ, the framework of both CAD systems is similar. A general CAD work-flow is presented n Fig. 2.1.

MRI modalities mentioned in Sect. ?? are used as inputs of CAD for CaP. These images acquired from the different modalities show a large variability between patients: the prostate organ can be located at different positions in images (e.g., patient motion, variation of acquisition plan), and the SI can be corrupted with noise or artefacts during the acquisition process (eg., magnetic field inhomogeneity, use of endorectal coil). To address these issues, the first stage of CAD is to pre-process multiparametric MRI images to reduce noise, remove artefacts and standardize the SI. At most of the later processes will be only focused on the prostate, it is necessary to segment the prostate in each MRI-modality to define

3. REVIEW OF CADE AND CADx FOR CAP

it as a ROI. However, data may suffer from misalignment due to patient motions or different acquisition parameters. Therefore, a registration step is usually performed so that all the previously segmented MRI images will be in the same reference frame. Registration and segmentation can be swapped depending on the strategy chosen.

Some studies do not fully apply the methodology depicted in Fig.. 2.1. Details about those can be found in Tab. 3.1. Some studies proposed methods in which inputs are the MRI raw data in order to demonstrate the robustness of their approaches to noise or artefacts. In some cases, prostate segmentation is performed manually as well as registration. It is also sometimes assumed that no patient motions occur during the acquisition procedure, removing the need of registering the multiparametric MRI images.

Once the data are regularized, it becomes possible to extract features and classify the data to obtain either the location of possible lesions (CADe) or/and the malignancy nature of these lesions (CADx).

In a CADe framework, *possible lesions will be segmented automatically* and further used as input of CADx. Nevertheless, some works also used a fusion CADe-CADx framework in which a voxel-based features are directly used, allowing to obtain the location of the malignant lesions as results. On the other hand, manual lesions segmentation are not considered to be part of CADe. The output of the CADe is used as input of the CADx.

CADx is composed of the processes allowing to *distinguish malignant from non-malignant tumours*. Here, CaP malignancy is defined using the grade of the GS determined after post biopsy or prostatectomy. As presented in Fig.. 2.1, CADx is usually composed of the three common steps used in classification framework: (i) features detection, (ii) feature extraction/selection and (iii) feature classification.

This chapter is organized using the methodology presented in Fig.. 2.1. Methods embedded in the image regularization framework are presented initially to subsequently focus on the image classification framework, being divided into CADe and CADx. Finally presenting the results and the discussion driven from the state-of-the-art. Table 3.1 summarizes the forty-two different CAD studies reviewed in section. The first set of information reported is linked to the data acquisition such as the number of patients included in the study, the modalities acquired as

well as the strength of the field of the scanner used. Subsequently, information about the prostate zones considered in the CAD analysis (PZ or CG) are reported since that detecting CaP in the CG is a more challenging problem and has received particular attention only in the recent publications.

3.1 Image regularization framework

This section provides a review of the methods used in CADs for CaP in order to regularize input images. We start with pre-processing methods presented in Sect.. 3.1.1, focusing mainly on the reduction of noise level and artefacts as well as standardization of SI. Sections 3.1.2 and ?? will be dedicated to segmentation methods, so that later methods only operate on the segmented prostate, and registration to align segmented images from different MRI-modalities in the same reference frame.

3.1.1 Pre-processing

Three different groups of pre-processing methods are commonly applied to images as initial stage in CAD for CaP. These methods are explained for both MRI and MRSI modalities, while a summary of the applied methods in CAD is presented in Table. 3.2.

Noise filtering: The NMR signal measured and recorded in the k-space during an MRI acquisition is affected by noise. This noise obeys a complex Gaussian white noise mainly due to thermal noises in the patient area [169]. Furthermore, MRI images visualized by radiologists are in fact the magnitude images resulting from the complex Fourier transform of the k-space data. The complex Fourier transform, being a linear and orthogonal transform, does not affect the Gaussian noise characteristics [169]. However, the function involved in the magnitude computation is a non-linear transform (i.e., the square root of the sum of squares of real and the imaginary parts), implying that the noise distribution is no longer Gaussian; it indeed follows a Rician distribution making the denoising task harder. Briefly, a Rician distribution can be characterized as follows: in low-SI region (low

3. REVIEW OF CADE AND CADX FOR CAP

Table 3.1: Overview of the different studies reviewed with their main characteristics. Acronyms: number (#) - image regularization (Img. Reg.).

Index	Study	# Cases	MRI-modality				Strength of field		Studied zones		CAD stages	
			T ₂ - W	DCE	DW	MRSI	1.5 T	3.0 T	PZ	CG	Reg.	CADE
[9]	Ampeliotis et al. (2007)	25	✓	✓	✗	✗	✓	✗	✓	✗	✓!	✗
[10]	Ampeliotis et al. (2008)	25	✓	✓	✗	✗	✓	✗	✓	✗	✓!	✗
[13]	Antic et al. (2013)	53	✓	✗	✓	✗	✓	✗	✓	✓	✗	✗
[14]	Artan et al. (2009)	10	✓	✓	✓	✗	✓	✗	✓	✗	✗	✓
[15]	Artan et al. (2010)	21	✓	✓	✓	✗	✓	✗	✓	✗	✓!	✓
[37]	Chan et al. (2013)	15	✓	✗	✓	✗	✓	✗	✓	✗	✗	✗
[73]	Giannini et al. (2013)	10	✓	✓	✓	✗	✓	✗	✓	✗	✓	✓
[110]	Kelm et al. (2007)	24	✗	✗	✗	✓	✓	✗	✓	✓	✓!	✓
[117]	Langer et al. (2009)	25	✓	✓	✓	✗	✓	✗	✓	✗	✓!	✗
[140]	Litjens et al. (2011)	188	✓	✓	✓	✗	✗	✓	✓	✗	✓!	✓
[141]	Litjens et al. (2012)	288	✓	✓	✓	✗	✗	✓	✓	✓	✓!	✓
[138]	Litjens et al. (2014)	347	✓	✓	✓	✗	✗	✓	✓	✓	✓!	✓
[144]	Liu et al. (2009)	11	✓	✓	✓	✗	✓	✗	✓	✗	✓!	✓
[142]	Liu et al. (2013)	54	✓	✓	✓	✓	✗	✗	✓	✓	✓!	✗
[145]	Lopes et al. (2011)	27	✓	✗	✗	✗	✓	✓	✓	✗	✓!	✓
[147]	Lv et al. (2009)	55	✓	✗	✗	✗	✓	✓	✓	✗	✓!	✗
[154]	Matulewicz et al. (2013)	18	✗	✗	✗	✓	✓	✗	✓	✓	✗	✓
[155]	Mazzetti et al. (2011)	10	✗	✓	✗	✗	✓	✓	✓	✗	✓!	✓
[166]	Niaf et al. (2011)	23	✓	✓	✓	✗	✓	✓	✓	✗	✓!	✗
[167]	Niaf et al. (2012)	30	✓	✓	✓	✓	✗	✓	✓	✗	✓!	✗
[175]	Ozer et al. (2009)	20	✓	✓	✓	✓	✗	✓	✓	✗	✓!	✓
[176]	Ozer et al. (2010)	20	✓	✓	✓	✓	✗	✓	✓	✗	✓!	✓
[180]	Parfait et al. (2012)	22	✗	✗	✗	✓	✓	✗	✓	✓	✓!	✓
[184]	Peng et al. (2013)	48	✓	✓	✓	✗	✗	✓	✓	✓	✓	✗
[192]	Puech et al. (2009)	100	✗	✓	✗	✗	✓	✓	✓	✗	✓	✗
[229]	Sung et al. (2011)	42	✗	✓	✗	✗	✗	✗	✓	✓	✓	✓
[233]	Tiwari et al. (2007)	14	✗	✗	✗	✓	✓	✓	✗	✓	✓!	✓
[234]	Tiwari et al. (2008)	18	✗	✗	✗	✓	✓	✓	✓	✗	✓!	✓
[235]	Tiwari et al. (2009)	18	✗	✗	✗	✓	✓	✓	✓	✗	✓!	✓
[236]	Tiwari et al. (2009)	15	✓	✗	✗	✓	✓	✓	✓	✗	✓!	✓
[237]	Tiwari et al. (2010)	19	✓	✗	✗	✓	✓	✓	✓	✗	✓!	✓
[238]	Tiwari et al. (2012)	36	✓	✗	✗	✓	✓	✓	✓	✗	✓	✓
[239]	Tiwari et al. (2013)	29	✓	✗	✗	✓	✓	✓	✓	✗	✓!	✓
[259]	Viswanath et al. (2008)	16	✓	✗	26	✗	✓	✓	✓	✗	✓	✓
[258]	Viswanath et al. (2008)	6	✓	✓	✗	✗	✗	✗	✓	✓	✓!	✓
[260]	Viswanath et al. (2009)	6	✓	✓	✗	✗	✗	✗	✓	✓	✓	✓
[261]	Viswanath et al. (2011)	12	✓	✓	✓	✗	✗	✓	✓	✓	✓!	✓

3.1 Image regularization framework

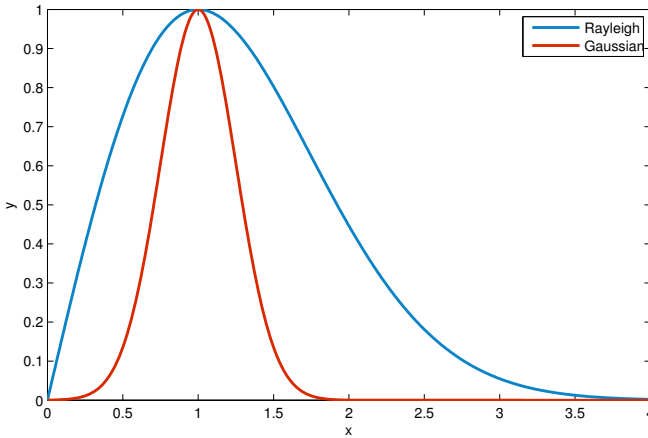


Figure 3.1: Illustration of a Gaussian distribution ($\mu = 1, \sigma = 0.25$) and a Rayleigh distribution ($\sigma = 2$). It can be seen that the Rayleigh distribution is suffering of a bias term when compared with the Gaussian distribution.

SNR), it can be approximated with a Rayleigh distribution while in high-SI region (high SNR), it is similar to a Gaussian distribution (see Fig. 3.1) [153]. Reviews of all denoising methods can be found in [30, 163].

Median filtering is the simplest approach used to address the denoising issue in MRI images [175, 176]. In both studies, Ozer *et al.* used a square kernel of size 5×5 pixels with the image resolutions ranging from 320×256 (cf., T₂-W MRI) to 256×128 (cf., T₂ map, DCE and DW MRI) and a field of view (FOV) ranging from 14 cm (cf, T₂-W and DW MRI) to 20 cm (cf, T₂ map and DCE MRI). However, from a theoretical point of view, this simple filtering method is not well formalized to address the noise distribution in MRI images.

More complex approaches were proposed to overcome this problem. A common method used to denoise MRI images is based on wavelet-based filtering. This filtering exploits the sparsity property of the wavelet decomposition. The projection of a noisy signal from the spatial-domain to the wavelet-domain implies that only few wavelet coefficients contribute to the “signal-free noise” while all wavelet coefficients contribute to the noise [57]. Therefore, denoising is performed by thresholding/attenuating the insignificant wavelet coefficients to enforce the sparsity in the wavelet-domain. Investigations focus on the strategies to perform the

3. REVIEW OF CADE AND CADX FOR CAP

most adequate coefficient shrinkage method (e.g., using thresholding, singularity property or Bayesian framework) [187].

Ampeliotis *et al.* in [9, 10] performed wavelet shrinkage to denoise magnitude MRI images (cf., T₂-W-MRI and DCE-MRI) using thresholding techniques [152]. However, since the wavelet transform is an orthogonal transform, the Rician distribution of the noise is preserved in the wavelet-domain. Hence, for low SNR, the wavelet and scaling coefficients still suffer from a bias due to this specific noise distribution [169].

Lopes *et al.* in [145] used the filtering technique proposed by [188] to denoise T₂-W-MRI which was based on joint detection and estimation theory [188]. In this approach, the wavelet coefficients “free-of-noise” are estimated from the noisy wavelet coefficients using a maximum *a posteriori* (MAP) estimate. Furthermore, the estimator designed takes spatial context into account by including both local and global information in the prior probabilities. The different probabilities needed by the MAP are empirically estimated by using mask images representing the locations of the significant wavelet coefficients. These mask images are computed by thresholding the detail images obtained from the wavelet decomposition. To remove the bias from the wavelet and scaling coefficients, the squared magnitude MRI image used instead of the magnitude MRI image as proposed by [169]. This involves changing the Rician distribution to a scaled non-central Chi-square distribution. It implies that the wavelet coefficients are also unbiased estimators and the scaling coefficients are unbiased estimators but up to a constant C as defined in Eq. (3.1) which needs to be subtracted from each scaling coefficient,

$$C = 2^{(J+1)}\hat{\sigma}^2 , \quad (3.1)$$

where J is the number of levels of the wavelet decomposition and $\hat{\sigma}$ is an estimate of the noise standard deviation.

Bias correction: Besides being corrupted by noise, MRI images are also affected by the inhomogeneity of the MRI field commonly referred to as bias field [228]. This bias field results in a smooth variation of the SI through the image. When an endorectal coil is used, an artefact resulting of an hyper-intense signal can be observed around the coil on the images (see Fig. 3.2).

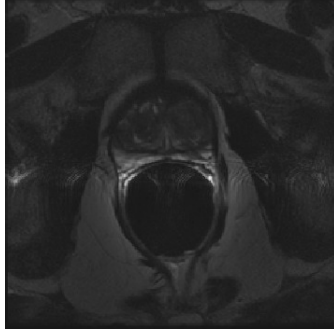


Figure 3.2: Example of artefacts with high SI due to perturbation from the endorectal coil which create inhomogeneity.

As a consequence, the SI of identical tissues varies depending on their spatial location in the image making further processes such as segmentation or registration harder [106, 267]. A review of bias correction methods can be found in [267].

The model of image formation is usually formalized such that:

$$s(\mathbf{x}) = o(\mathbf{x})b(\mathbf{x}) + \eta(\mathbf{x}) , \quad (3.2)$$

where $s(\mathbf{x})$ is the corrupted SI at the pixel for the image coordinates $\mathbf{x} = \{x, y\}$, $o(\mathbf{x})$ is the “noise-free signal” , $b(\mathbf{x})$ is the bias field function and $\eta(\mathbf{x})$ is an additive white Gaussian noise.

Hence, the task of bias correction involves estimating the bias function $b(\mathbf{x})$ in order to infer the “signal-free bias” $o(\mathbf{x})$.

Viswanath *et al.* [260] performed bias correction on T₂-W-MRI using a parametric Legendre polynomial model proposed in [228] and available in the Insight Segmentation and Registration Toolkit (ITK) library¹.

Styner *et al.* [228] chose to model the bias field by using a linear combination of Legendre polynomials as:

$$\hat{b}(\mathbf{x}, \mathbf{p}) = \sum_{i=0}^{m-1} p_i f_i(\mathbf{x}) = \sum_{i=0}^l \sum_{j=0}^{l-i} p_{ij} P_i(x) P_j(y) , \quad (3.3)$$

where \hat{b} is the bias estimation with the image coordinates $\mathbf{x} = \{x, y\}$ and the m coefficients of the linear combination $\mathbf{p} = p_{11}, \dots, p_{ij}$; m can be defined as

¹The ITK library is available at: <http://www.itk.org/>

3. REVIEW OF CADE AND CADX FOR CAP

$m = (l + 1)\frac{(l+2)}{2}$ where l is the degree of Legendre polynomials chosen and $P_i(\cdot)$ denotes a Legendre polynomial of degree i .

This family of functions allows us to model the bias as a smooth inhomogeneity function across the image. To estimate the set of parameters \mathbf{p} , a cost function is defined which relies on the following assumptions: (i) an image is composed of k regions with μ_k being the mean SI and a variance σ_k^2 of each particular class, and (ii) each noisy pixel belongs to one of the k regions with its SI value close to the class mean μ_k . Hence, the cost function is defined as:

$$C(\mathbf{p}) = \sum_{\mathbf{x}} \prod_k \rho_k(s(\mathbf{x}) - \hat{b}(\mathbf{x}, \mathbf{p}) - \mu_k) , \quad (3.4)$$

$$\rho_k(x) = \frac{x^2}{x^2 + 3\sigma_k^2} , \quad (3.5)$$

where $\rho_k(\cdot)$ is a M-estimator allowing estimations to be less sensitive to outliers than usual square distance [132].

Finally, estimation of the parameters \mathbf{p} results in finding the minimum of the cost function $C(\mathbf{p})$. This optimization was performed using the non-linear (1 + 1) Evolution Strategy (ES) optimizer [227].

In a later publication, [262] make use of the well known N3 algorithm¹ to correct T₂-W-MRI developed by [217]. To estimate the bias function, [217] proposed to estimate the PDFs of the signal and bias.

Recalling Eq. (3.2) and taking advantage of logarithm property, it implies that this model becomes additive such that:

$$\begin{aligned} \log s(\mathbf{x}) &= \log b(\mathbf{x}) + \log \left(o(\mathbf{x}) + \frac{\eta(\mathbf{x})}{b(\mathbf{x})} \right) , \\ &\approx \log b(\mathbf{x}) + \log \hat{o}(\mathbf{x}) , \end{aligned} \quad (3.6)$$

where $\hat{o}(\mathbf{x})$ is the signal only degraded by noise. [217] shows that Eq. (3.6) can be related to PDFs such that:

$$S(s) = B(s) * O(s) , \quad (3.7)$$

¹The N3 algorithm implementation is available at: <http://www.bic.mni.mcgill.ca/software/N3/>

3.1 Image regularization framework

where S , B and O are respectively the probability densities of s , b and o .

Restoring the corrupted signal s is carried out by finding the multiplicative field b which maximizes the frequency content of the distribution O . Sled *et al.* [217] argue that a search through all possible fields b and selection of the one which maximizes the high frequency content of O could be carried out but results in an exhaustive search. However, they show that the bias field distribution can be assimilated to a near Gaussian distribution. Using this fact as *a priori*, it is then possible to infer the distribution O using Wiener deconvolution given B and S and later estimate the corresponding smooth field b .

Lv *et al.* [147] corrected the inhomogeneity in T₂-W-MRI images by using the method proposed in [150]. In this method, the MRI images are corrected iteratively by successively detecting the image foreground via generalized scale (g -scale) and estimating a bias field function based on a second-order polynomial model. First the background of the MRI image is eliminated by thresholding. The threshold value is commonly equal to the mean SI of the considered image. Then, in the seeded region growing algorithm is applied considering every thresholded pixel as a potential seed. However, pixels already assigned to a region will not be considered any more as seed. As in seeded region growing algorithm [213], two criteria are taken into account to expand the region. First, the region will grow using a connected-neighbourhood, initially defined by the user. Then, the homogeneity of SI is based on a fuzzy membership function taking into account the absolute difference of the SIs of two pixels. Depending on the membership value (cf., a threshold has to be defined), the pixel considered is merged or not to the region. Once this segmentation is performed, the largest region R is used as a mask to select pixels of the original image and the mean SI, μ_R , is computed. The background variation $b(\mathbf{x})$ is estimated as:

$$b(\mathbf{x}) = \frac{s(\mathbf{x})}{\mu_R}, \quad \forall \mathbf{x} \in R, \quad (3.8)$$

where $s(\mathbf{x})$ is the original MRI image.

Finally, a second order polynomial $\hat{b}_\Theta(\mathbf{x})$ is fitted in a least-squares sense

3. REVIEW OF CADE AND CADX FOR CAP

(Eq. (3.9)),

$$\hat{\Theta} = \arg \min_{\Theta} |b(\mathbf{x}) - \hat{b}_{\Theta}(\mathbf{x})|^2, \quad \forall \mathbf{x} \in R. \quad (3.9)$$

Finally, the whole original MRI image is corrected by dividing it by the estimated bias field function $\hat{b}_{\Theta}(\mathbf{x})$. This process is repeated until the number of pixels in the largest region R does not change significantly between two iterations.

SI normalization/standardization: As discussed in the later section, segmentation or classification tasks are usually performed by first learning from a training set of patients. Hence, one can emphasize the desire to perform MRI examinations with a high repeatability or in other words, one would ensure to obtain similar MRI images (cf., similar SIs) for patients of the same group (cf., healthy patients *vs.* patients with CaP), for a similar sequence.

However, it is a known fact that variability between patients occurs during the MRI examinations even using the same scanner, protocol or sequence parameters [170]. Hence, the aim of normalization or standardization of the MRI data is to remove the variability between patients and enforce the repeatability of the MRI examinations. Approaches used to standardize MRI images can be either categorized as statistical-based standardization or organ SI-based standardization.

Artan *et al.* [14, 15] as well as Ozer *et al.* [175, 176] standardized T₂-W, DCE and DW MRI images by computing the *standard score* (also called *z-score*) of the pixels of the PZ as:

$$I_s(\mathbf{x}) = \frac{I_r(\mathbf{x}) - \mu_{pz}}{\sigma_{pz}}, \quad \forall \mathbf{x} \in \text{PZ}, \quad (3.10)$$

where $I_s(\mathbf{x})$ is the standardized SI with the image coordinates $\mathbf{x} = \{x, y\}$, $I_r(\mathbf{x})$ is the raw SI, μ_{pz} is the mean-SI of the PZ and σ_{pz} is the SI standard deviation in the PZ. This transformation enforces the image PDF to have a zero mean and a unit standard deviation.

In a similar way, Liu *et al.* [142] normalized T₂-W-MRI by making use of the median and interquartile range for all the pixels.

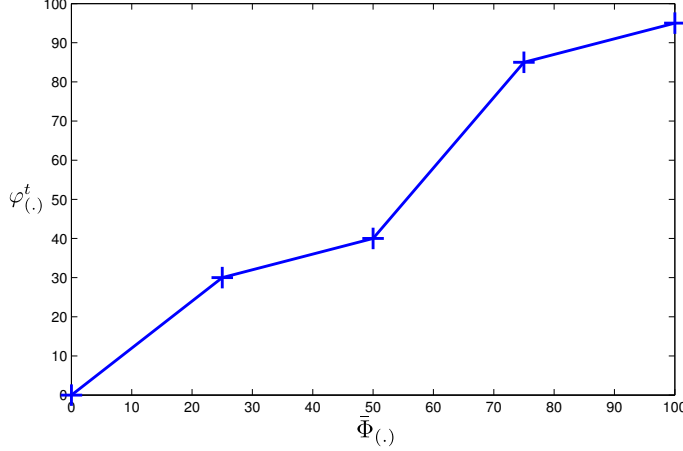


Figure 3.3: Example of linear mapping by parts as proposed by [171].

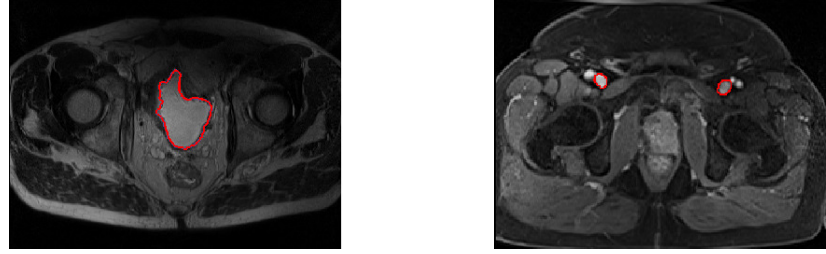
Lv *et al.* [147] scaled the SI of T₂-W-MRI images using the method proposed in [171] based on PDF matching. This approach is based on the assumption that MRI images from the same sequence should share the same PDF appearance. Hence, one can approach this issue by transforming and matching the PDFs using some statistical landmarks such as median and different quantiles. Using a training set, these statistical landmarks are extracted for N training images as for instance for the minimum, the 25th quantile, the median, the 75th quantile and the maximum:

$$\begin{aligned}
 \Phi_0 &= \{\phi_0^1, \phi_0^2, \dots, \phi_0^N\}, \\
 \Phi_{25} &= \{\phi_{25}^1, \phi_{25}^2, \dots, \phi_{25}^N\}, \\
 \Phi_{50} &= \{\phi_{50}^1, \phi_{50}^2, \dots, \phi_{50}^N\}, \\
 \Phi_{75} &= \{\phi_{75}^1, \phi_{75}^2, \dots, \phi_{75}^N\}, \\
 \Phi_{100} &= \{\phi_{100}^1, \phi_{100}^2, \dots, \phi_{100}^N\},
 \end{aligned} \tag{3.11}$$

where $\phi_{n^{\text{th}}}^i$ is the n^{th} quantile of the i^{th} training image.

Then, the mean of each quantile $\{\bar{\Phi}_0, \bar{\Phi}_{25}, \bar{\Phi}_{50}, \bar{\Phi}_{75}, \bar{\Phi}_{100}\}$ is also calculated. Once this training stage is performed, a linear transformation by parts $\mathcal{T}(\cdot)$ can be computed (Eq. (3.12)) for each test image t by mapping each statistical landmark

3. REVIEW OF CADE AND CADX FOR CAP



(a) Illustration and location of the bladder on a T₂-W MRI image acquired with a 3.0 Tesla MRI scanner

(b) Illustration and location of the femoral arteries on a T₁-W-MRI image acquired with a 3.0 Tesla MRI scanner

Figure 3.4: Illustration of the two organs used by [166, 167] to normalize T₂-W and T₁-W MRI images.

$\varphi_{(cdot)}^t$ of this image with the pre-learned statistical landmarks $\bar{\Phi}_{(.)}$. This linear mapping is also depicted in Fig. 3.3.

$$\mathcal{T}(s(\mathbf{x})) = \begin{cases} \lceil \bar{\Phi}_0 + (s(\mathbf{x}) - \varphi_0^t) \left(\frac{\bar{\Phi}_{25} - \bar{\Phi}_0}{\varphi_{25}^t - \varphi_0^t} \right) \rceil, & \text{if } \varphi_0^t \leq s(\mathbf{x}) < \varphi_{25}^t, \\ \lceil \bar{\Phi}_{25} + (s(\mathbf{x}) - \varphi_{25}^t) \left(\frac{\bar{\Phi}_{50} - \bar{\Phi}_{25}}{\varphi_{50}^t - \varphi_{25}^t} \right) \rceil, & \text{if } \varphi_{25}^t \leq s(\mathbf{x}) < \varphi_{50}^t, \\ \lceil \bar{\Phi}_{50} + (s(\mathbf{x}) - \varphi_{50}^t) \left(\frac{\bar{\Phi}_{75} - \bar{\Phi}_{50}}{\varphi_{75}^t - \varphi_{50}^t} \right) \rceil, & \text{if } \varphi_{50}^t \leq s(\mathbf{x}) < \varphi_{75}^t, \\ \lceil \bar{\Phi}_{75} + (s(\mathbf{x}) - \varphi_{75}^t) \left(\frac{\bar{\Phi}_{100} - \bar{\Phi}_{75}}{\varphi_{100}^t - \varphi_{75}^t} \right) \rceil, & \text{if } \varphi_{75}^t \leq s(\mathbf{x}) \leq \varphi_{100}^t, \end{cases} \quad (3.12)$$

Viswanath *et al.* [260, 261, 262] use a variant of this previous approach presented in [149] aiming to standardize the T₂-W-MRI images. Instead of computing the PDF of an entire image, a pre-segmentation of the foreground is carried out via *g*-scale which was discussed in the bias correction section. Once the foreground is detected, the largest region is extracted and the same process than previously mentioned (see Eq. (3.12)) takes place in order to align PDFs of the foreground of the MRI images.

The methods described above were statistical-based methods. However, the standardization problem can be tackled by normalizing the MRI images using the SI of some known organs present in these images. Niaf *et al.* [166, 167] normalized T₂-W-MRI images by dividing the original SI of the images by the mean SI of the bladder (see Fig. 3.4(a)). Likewise, [166] standardized the T₁-W-MRI images

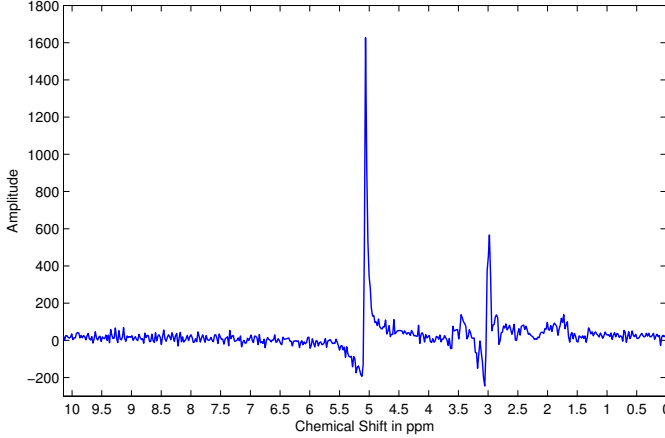


Figure 3.5: Illustration of phase misalignment in an MRSI spectra acquire with a 3.0 Tesla MRSI scanner. Note the distortion of the signal specially visible for the water and citrate peaks.

using the arterial input function (AIF). They computed the AIF by taking the mean of the SI in the most enhanced part of the common femoral arteries (see Fig. 3.4(b)) as proposed in [271].

Presented in Sect. 2.2.6, MRSI is a modality related to a one dimensional signal. Hence, specific pre-processing steps for this type of signals have been applied instead of standard signal processing methods.

Phase correction: MRSI data acquired suffer from zero-order and first-order phase misalignments as shown in Fig. 3.5 [40, 173]. Parfait *et al.* [180] used a method proposed in [40] where the phase of MRSI signal is corrected based on entropy minimization in the frequency domain. The corrected MRSI signal $o(\xi)$ can be expressed as:

$$\begin{aligned}\Re(o(\xi)) &= \Re(s(\xi)) \cos(\Phi(\xi)) - \Im(\xi) \sin(\Phi(\xi)) , \\ \Im(o(\xi)) &= \Im(s(\xi)) \cos(\Phi(\xi)) + \Re(\xi) \sin(\Phi(\xi)) , \\ \Phi(\xi) &= \phi_0 + \phi_1 \frac{\xi}{N} ,\end{aligned}\tag{3.13}$$

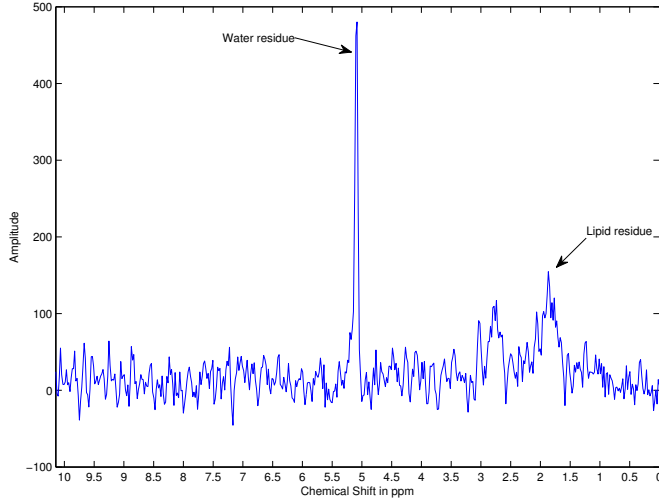


Figure 3.6: Illustration of the residues of water and fat even after their suppression during the acquisition protocol. The acquisition was carried out with a 3.0 Tesla MRI.

where $\Re(\cdot)$ and $\Im(\cdot)$ are the real and imaginary part of the complex signal respectively, $s(\xi)$ is the corrupted MRSI signal, ϕ_0 and ϕ_1 are the zero-order and first-order phase correction terms respectively and N is the total number of samples of the MRSI signal.

Chen *et al.* [40] tackled this problem using an optimization framework where ϕ_0 and ϕ_1 had to be inferred. Hence, the simplex Nelder-Mead optimization method was used to minimize the following cost function based on the *Shannon entropy* formulation:

$$\hat{\Phi} = \arg \min_{\Phi} \left[- \sum \Re(s'(\xi)) \ln \Re(s'(\xi)) + \lambda \|\Re(s(\xi))\|_2 \right], \quad (3.14)$$

where $s'(\xi)$ is the first derivative of the corrupted signal $s(\xi)$ and λ is a regularization parameter. Once the best parameter Φ is obtained, the MRSI signal is corrected using Eq. (3.13).

Water and lipid residuals filtering: The water and lipid metabolites occur in much higher concentrations than the metabolites of interests (cf., choline, creatine

3.1 Image regularization framework

and citrate) [173, 275]. Fortunately, specific MRSI sequences were developed in order to suppress water and lipid metabolites using pre-saturation techniques [275]. However, these techniques do not perfectly remove water and lipids peaks and some residuals are still present in the MRSI spectra as shown in Fig. 3.6. Therefore, different post-processing methods have been proposed to enhance the quality of the MRSI spectra by removing these residuals. For instance, Kelm *et al.* [110] used the well known HSVD algorithm proposed by [186] which models the MRSI signal by a sum of exponentially damped sinusoids in the time domain (see Eq. (3.15)).

$$s(t) = \sum_{k=1}^K a_k \exp(i\phi_k) \exp(-d_k + i2\pi f_k)t + \eta(t) , \quad (3.15)$$

where a_k is the amplitude proportional to the metabolite concentration with a resonance frequency f_k , d_k represents the damping factor of the exponential, ϕ_k is the first-order phase and $\eta(t)$ is a complex white noise.

Pijnappel *et al.* [186] showed that the “noise-free signal” can be found using the singular value decomposition (SVD) decomposition. First the noisy signal is reorganized inside a Hankel matrix H . It can be shown that if the signal considered would be a “noise-free signal”, the rank of H would be equal to rank K . However, due to the presence of noise, H is in fact a full rank matrix. Thus, to recover the “noise-free signal”, the rank of H can be truncated to K using its SVD decomposition. Hence, knowing the cut off frequencies of water (cf., 4.7 ppm) and lipid (cf., 2.2 ppm) metabolites, their corresponding peaks can be reconstructed and subtracted from the original signal [120].

Baseline correction: Sometimes, the problem discussed in the above section regarding the lipid molecules is not addressed simultaneously with water residuals suppression. Lipids and macromolecules are known to affect the baseline of the MRSI spectra. They could cause errors during further fitting processes aiming to quantify the metabolites, especially regarding the citrate metabolite.

Parfait *et al.* [180] made the comparison of two different methods to detect the baseline and correct the MRSI spectra which are based on [56, 133]. Lieber *et al.* [133] addressed the problem of baseline detection in the frequency domain by fitting a low degree polynomial whereas Parfait *et al.* [180] modified this algorithm

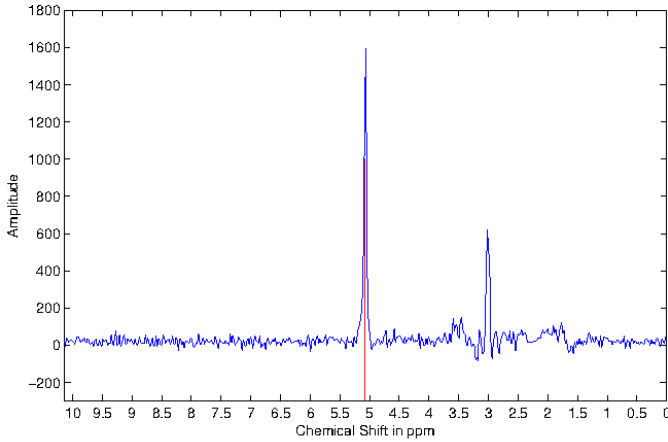


Figure 3.7: Illustration of frequency misalignment in an MRSI spectra acquired with a 3.0 Tesla MRSI scanner. The water peak is known to be aligned at 4.65 ppm. However, it can be seen that the peak on this spectra is aligned at around 5.1 ppm.

by convolving a Gaussian kernel to smooth the MRSI signal instead of fitting a polynomial function. **Check the tex file to see the commented area pre-processing.tex**

Unlike in [133], Devos *et al.* [56] proposed to correct the baseline in the time domain by multiplying the MRSI signal by a decreasing exponential function as:

$$c(t) = \exp(-\beta t) , \quad (3.16)$$

Having a typical value for β of 0.15. However, Parfait *et al.* [180] concluded that the method proposed in [133] outperformed the one in [56].

In the contemporary work of Tiwari *et al.* [238], the authors detected the baseline using a local non-linear fitting method avoiding regions with significant peaks which were detected using a experimentally parametrised signal-to-noise ratio (i.e. a value larger than 5 dB).

Frequency alignment: Due to variations of the experimental conditions, a frequency shift can be observed in the MRSI spectra [40, 173] as shown in Fig. 3.7.

Tiwari *et al.* [238] corrected the frequency shift by first detecting known metabolite peaks such as choline, creatine and citrate. The frequency shift is corrected by

minimizing the frequency error between the experimental and theoretical values of each of these peaks.

Normalization: Due to variations of the experimental conditions, the MRSI signal may also vary between patients. Parfait *et al.* [180] as in [56] compared two methods to normalize MRSI signal. In each method, the original MRSI spectra is divided by a normalization factor, similar to the intensity normalization described earlier. The first approach to obtain the normalization factor is based on an estimation of the water concentration. It is required to have an additional MRSI sequence where the water metabolites are unsuppressed. Using this sequence, an estimation of the water concentration can be performed using the previously reported HSVD algorithm. The second approach to normalization is based on using the L_2 norm of the MRSI spectra $\|s(\xi)\|_2$. It should be noted that both [180] and [56] concluded that the L_2 normalization was more efficient in their framework.

3.1.2 Segmentation

The segmentation task consists of delineating the prostate boundaries in the MRI and is of particular importance for focusing the posterior processing on the organ of interest [72]. In this section, only the segmentation methods used in CAD for CaP are presented and summarized in Table. 3.3. These methods are mostly intensity based. An exhaustive review of prostate segmentation methods in MRI can be found in [72].

Manual segmentation: To highlight the importance of prostate segmentation task in CAD systems, it is interesting to note the large number of studies which manually segment the prostate organs [14, 15, 154, 166, 167, 175, 176, 192, 263, 264]. In all the cases, the boundaries of the prostate gland are manually defined in order to limit further processing to only this area. This approach ensures the right delineation of the organ nevertheless this procedure is highly time consuming and should be performed by a radiologist.

3. REVIEW OF CADE AND CADX FOR CAP

Table 3.2: Overview of the pre-processing methods used in CAD systems.

Pre-processing operations	References
<hr/>	
<i>MRI pre-processing:</i>	
Noise filtering:	
Median filtering	[175, 176]
Wavelet-based filtering	[9, 10, 145]
Bias correction:	
Parametric methods	[147, 260]
Non-parametric methods	[261]
Standardization:	
Statistical-based normalization:	[14, 15, 147, 175, 176, 260, 261, 262]
Organ SI-based normalization	[166, 167]
<i>MRSI pre-processing:</i>	
Phase correction	[180]
Water and lipid residuals filtering	[110]
Baseline correction	[180, 238]
Frequency alignment	[238]
Normalization	[180]

Table 3.3: Overview of the segmentation methods used in CAD systems.

Segmentation methods	References
<i>MRI-based segmentation:</i>	
Manual segmentation	[14, 15, 154, 166, 167, 175, 176, 192, 263, 264, 265, 266]
Region-based segmentation	[138, 141]
Model-based segmentation	[140, 258, 260, 261, 266]
<i>MRSI-based segmentation:</i>	
Clustering	[235]

Region-based segmentation: Litjens *et al.* in [141] used a multi-atlas-based segmentation using multi-modal images (e.g., T₂-W-MRI and ADC map) to segment the prostate with an additional pattern recognition method to differentiate CG and PZ as proposed in [137]. This method consists in three different steps: (i) the registration between each atlas and the multi-modal images, (ii) the atlas selection and finally (iii) the classification of the prostate segmented voxels in either CG or PZ. The registration between each atlas and the MRI images is performed using two successive registrations; the first registration is a rigid registration to roughly aligned the atlases and the MRI images and the second is an elastic registration using B-spline transformation. The objective function to perform the registration is defined as the weighted sum of the metric of both T₂-W-MRI and ADC map. The metric is based on mutual information (MI) (please refer to the next section for more details in regard to registration). Two strategies of atlas selection were performed by using either a majority voting approach or the simultaneous truth and performance level estimation (STAPLE) approach [270].

Subsequently, CG and PZ segmentation within the prostate region is achieved by classifying each voxel using a linear discriminant analysis (LDA) classifier. Three types of features were considered: (i) anatomy, (ii) intensity and (iii) texture. Regarding the anatomy, relative position and relative distance from the pixel to the border of the prostate were used. The intensity features consist in the inten-

3. REVIEW OF CADE AND CADX FOR CAP

sity of the voxel in the ADC coefficient and the T_2 map. The texture features were composed of five different features: homogeneity, correlation [6], entropy, texture strength [130] and local binary pattern (LBP) [172]. Finally, some morphological operations were applied to remove artefact and the contour between the zones were smooth using the thin plate spline (TPS) [23].

Litjens *et al.* in [138] used an almost identical algorithm proposed by PROMISE12 challenge [139]. Their segmentation method is also based on multi-atlas multi-modal images, but the SIMPLE method [118] is used instead to combine labels after the registration of the different atlas to obtain the final segmentation.

Model-based segmentation: Viswanath *et al.* in [258, 260] used a multi-attribute non-initializing texture reconstruction based active shape model (MANTRA) method as proposed in [243]. MANTRA is closely related to the active shape model (ASM) from [47]. This algorithm consists of two stages: (i) a training stage where a shape and appearance model is generated and (ii) the actual segmentation performed based on the learned model. For the training stage, a set of landmarks is defined and the shape model is generated as in the original ASM method [47]. Then, to model the appearance, a set of K texture images $\{I_1, I_2, \dots, I_k\}$ based on first and second order statistical texture features are computed. For a given landmark l with its given neighbourhood $\mathcal{N}(l)$, its feature matrix extracted can be expressed as:

$$f_l = \{I_1(\mathcal{N}(l)), I_2(\mathcal{N}(l)), \dots, I_k(\mathcal{N}(l))\}, \quad (3.17)$$

where $I_k(\mathcal{N}(l))$ represents a feature vector obtained by sampling the k^{th} texture map using the neighbourhood $\mathcal{N}(l)$. By generating multiple landmarks in the same fashion as ASM, PCA [182] is applied to learn the appearance variations.

For the segmentation stage, the mean shape learned previously is initialised in the test image. The same associated texture images as in the training stage are computed. For each landmark l , a neighbourhood of patches are used to sample the texture images and a reconstruction is obtained using the appearance model previously trained. The new landmark location will be defined as the position where the MI is maximal between the reconstructed and original values. This scheme is performed in a multi-resolution manner as in [47].

3.1 Image regularization framework

Subsequently, Viswanath *et al.* in [262], used the weighted ensemble of regional image textures for active shape model segmentation (WERITAS) method also proposed by [244]. WERITAS and MANTRA methods, both are based on the ASM formulation. However, they differ in the last stage, where in WERITAS instead of using MI to adapt the positions of new landmarks, a Mahalanobis distance metric is used. In the training stage, the Mahalanobis distance is computed between landmarks and neighbour patches for each of the features. Subsequently, a new metric is proposed as a linear weighted combination of those Mahalanobis distances which maximises the correlation with the Euclidean distance between the patches and the true landmarks. In the segmentation step, this metric is then computed between the initialised landmarks and neighbouring patches in order to update landmark positions, in a similar fashion to other active contour model (ACM) models. [Check the commented senetcence in the tex file.](#)

Litjens *et al.* [140] and Vos *et al.* [266] used an approach proposed in [99] in which the bladder, prostate and rectum are segmented. The segmentation task is performed as an optimization problem taking three parameters into account linked to organs such as: (i) the shape (an ellipse), (ii) the location and (iii) the respective angles between them. Furthermore, Litjens *et al.* [140] used only ADC map to encode the appearance whereas Vos *et al.* [266] used both ADC and T₂ maps. Then, during the optimization using a quasi-Newton optimizer, an objective function is minimized. This function is defined as the sum of the deviations from the above model learnt. This rough segmentation is then used inside a Bayesian framework to refine the segmentation.

Only the work of Tiwari *et al.* in [235] propose a segmentation based on MRSI. Authors localized the voxels corresponding to the prostate organ using a hierarchical spectral clustering. First, each MRSI spectrum is projected into a lower dimension space using graph embedding [214]. To proceed, a similarity matrix W is computed using a Gaussian similarity measure from Euclidean distance [18]) such that:

$$W(\mathbf{x}, \mathbf{y}) = \begin{cases} \exp\left(\frac{\|s(\mathbf{x})-s(\mathbf{y})\|_2^2}{\sigma^2}\right) & , \text{ if } \|\mathbf{x} - \mathbf{y}\|_2 < \epsilon , \\ 0 & , \text{ if } \|\mathbf{x} - \mathbf{y}\|_2 > \epsilon . \end{cases} \quad (3.18)$$

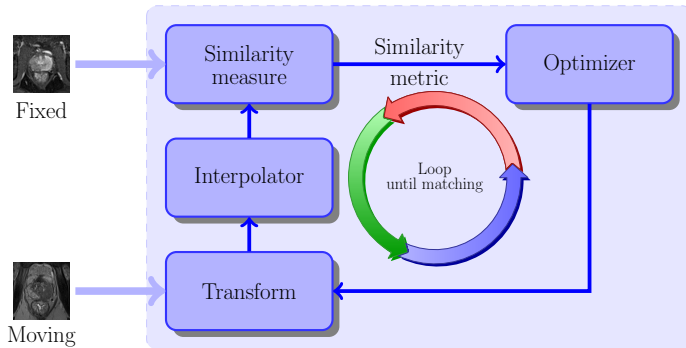


Figure 3.8: Typical framework involved to solve the registration problem.

where $s(\mathbf{x})$ and $s(\mathbf{y})$ are the MRSI spectra for the voxels \mathbf{x} and \mathbf{y} respectively, σ is the standard deviation of the Gaussian similarity measure and ϵ is the parameter to define an ϵ -neighbourhood.

The MRSI spectra projection into the lower dimension space is approached as a generalized eigenvector problem. Subsequently, a replicate k-means clustering method is run defining two clusters. The data corresponding to larger cluster is assumed to belong to the non-prostate voxels and these voxels will be eliminated from the processing. The full procedure is repeated until the total number of voxels left is inferior to a given threshold set experimentally.

3.1.3 Registration

The role of image registration is vital in CAD systems using multi-parametric MRI images. As it will be discussed in Sect. 3.2, for the sake of an optimal classification, the features detected in each modality will be grouped depending of their spatial locations. Hence, one has to ensure the perfect alignment of the multi-modal MRI images ahead of performing any classification.

Image registration is the procedure consisting of aligning an unregistered image (also called moving image) into a template image (also called fixed image) via a geometric transformation. This problem is usually addressed as presented in Fig. 3.8. An iterative procedure takes place to infer the geometric transformation (parametric or non-parametric) via an optimizer, which maximizes the similarity between the two images. In the following, a review of the different components of a

typical registration framework: transformation model, similarity metric, optimizer and interpolation are presented, followed by a summary of registration approaches applied in CAD for CaP systems. Exhaustive reviews covering all registration methods in computer science and medical fields can be found in [151] and [277].

Geometric transformation models: As previously mentioned, the registration problem is to align two images or volumes by finding the geometric transformation. Regarding the transformation, from all CAD systems reviewed, only parametric methods have been implemented. Three different groups of parametric transformation models have been used, rigid, affine, and elastic, each of them are characterized by the degree of freedom that they offer.

The first type of transformation is usually referred to as rigid transformation. These transformations are only composed of rotation and translation transforms. Hence, for a 2D space where $\mathbf{x} = (x, y) \in \mathbb{R}^2$, a rigid transformation \mathcal{T}_R is formalized as:

$$\begin{aligned} \mathcal{T}_R(\mathbf{x}) &= \begin{bmatrix} R & \mathbf{t} \\ \mathbf{0}^T & 1 \end{bmatrix} \mathbf{x}, \\ &= \begin{bmatrix} \cos \theta & -\sin \theta & t_x \\ \sin \theta & \cos \theta & t_y \\ 0 & 0 & 1 \end{bmatrix} \begin{bmatrix} x \\ y \\ 1 \end{bmatrix}, \end{aligned} \quad (3.19)$$

where θ is the rotation angle and $\{t_x, t_y\}$ represents the translation along $\{x, y\}$ respectively.

In the case of 3D registration using volume, an additional component z has to be taken into account such that $\mathbf{x} = (x, y, z)$. Thus, the rotation matrix \mathbf{R} becomes of size 3×3 whereas the translation vector \mathbf{t} consists of a vector of three elements. Hence, the geometric transformation $\mathcal{T}_R(\cdot)$ is embedded into a matrix of size 4×4 .

Affine transformations provide additional degrees of freedom managing rotations and translation as with the rigid transformations but also shearing and scaling. Hence, for a 2D space where $\mathbf{x} = (x, y) \in \mathbb{R}^2$, an affine transformation \mathcal{T}_A is formalized as:

3. REVIEW OF CADE AND CADX FOR CAP

$$\begin{aligned}
 \mathcal{T}_A(\mathbf{x}) &= \begin{bmatrix} A & \mathbf{t} \\ \mathbf{0}^T & 1 \end{bmatrix} \mathbf{x}, \\
 &= \begin{bmatrix} a_{11} & a_{12} & t_x \\ a_{21} & a_{22} & t_y \\ 0 & 0 & 1 \end{bmatrix} \begin{bmatrix} x \\ y \\ 1 \end{bmatrix}.
 \end{aligned} \tag{3.20}$$

Hence the four parameters $\{a_{11}, a_{12}, a_{21}, a_{22}\}$ of the affine matrix and $\{t_x, t_y\}$ of the translation encode an affine transformation.

Regarding volume registration, the previously mentioned remark can be applied as well. Thus the geometric transformation $\mathcal{T}_A(\cdot)$ is of size 4×4 with nine parameters involved.

Finally, the last group of transformations is known as elastic transformations and offer the advantage to handle local distortions. In the reviewed CAD systems, the radial basis functions are used to formalize the local distortions such as:

$$\mathcal{T}_E(\mathbf{x}) = \frac{a_{11}x - a_{12}y + t_x + \sum_i c_i g(\|\mathbf{x} - p_i\|)}{a_{21}x + a_{22}y + t_y + \sum_i c_i g(\|\mathbf{x} - p_i\|)}, \tag{3.21}$$

where \mathbf{x} are the control points in both images and $g(\dots)$ is the actual radial basis function.

Two radial basis functions are used: (i) the TPS and (ii) the B-splines. Apart from the formalism, these two approaches have a main difference: with B-splines, the control points are usually uniformly and densely placed on a grid where as with TPS, the control points correspond to detected or selected key points. By using TPS, Mitra *et al.* [161] obtained more accurate and time efficient results than with the B-splines strategy [162].

It is reasonable to point out that usually only rigid or affine registrations are used to register multi-parametric images from a same protocol. Elastic registration methods are more commonly used to register multi-protocol images (e.g., histopathology with MRI images) [243, 244].

Similarity measure: The most naive similarity measure used in reviewed registration framework is the mean squared error (MSE) of the SI of MRI images.



(a) Illustration of a joint histogram between two aligned images.

(b) Illustration of a joint histogram between two misaligned images.

Figure 3.9: Difference observed in joint histogram between aligned and misaligned images. The joint measure will be more concentrated of the histogram in the case that the images are aligned and more randomly distributed in the case that both images are more misaligned.

For a pair of images I and J , the MSE is formalized as:

$$\text{MSE} = \frac{1}{N} \sum_x \sum_y (I(x, y) - J(x, y))^2 , \quad (3.22)$$

where N is the total number of pixels. This metric is not well suited when multi-parametric images are involved due to the tissue appearance variations between the different modalities.

In that regard, MI was introduced as a registration measure in the late 1990's by [189]. The MI measure finds its foundation in the assumption that a homogeneous region in the first modality image should also appear as a homogeneous region in the second modality even if their SIs are not identical. Thus, those regions share information and the registration task can be achieved by maximizing this common information. Hence, MI of two images A and B is defined as:

$$MI(A; B) = S(A) + S(B) - S(A, B) , \quad (3.23)$$

where $S(A)$ and $S(B)$ are the marginal entropies and $S(A, B)$ is the joint entropy. Then, maximizing the MI is equivalent to minimizing the joint entropy. The joint entropy measure is related with the degree of uncertainty or dispersion of the data in the joint histogram of the images A and B . As shown in Fig. ??, the data in

3. REVIEW OF CADE AND CADX FOR CAP

the joint histogram will be concentrated in the case of aligned images while will be more randomly distributed in the case of misaligned images. Regarding the computation of the entropies, an estimation of the PDFs have to be carried out. Histogram or Parzen window methods are a common way to estimate these PDFs.

A generalized form of MI, combined mutual information (CMI), was proposed by [38]. CMI encompasses interdependent information such as texture and gradient into the metric. Hence, for both of images A and B , the image ensembles ϵ_n^A and ϵ_m^B are generated and composed of n and m images based on the texture and gradient. Then, the CMI can be formulated such as:

$$CMI(\epsilon_n^A; \epsilon_m^B) = S(\epsilon_n^A) + S(\epsilon_m^B) - S(\epsilon_n^A, \epsilon_m^B). \quad (3.24)$$

Check the commented text, It is not well written and I did not include them

Optimization methods: Registration is usually regarded as an optimization problem where the parameters of the geometric transformation model have to be inferred by minimizing the similarity measure. Iterative estimation methods are commonly used being the L-BFGS-B quasi-Newton method [32] and gradient descent [257] the most common ones. During our review, we noticed that authors do not usually linger over optimizer choice.

Interpolation: The registration procedure involves transforming an image, and pixels mapped to non-integer points must be approximated using interpolation methods. As for the optimization methods, we notice that little attention has been paid on the choice of those interpolations methods. However, commonly used methods are bilinear, nearest-neighbour, bi-cubic, spline and inverse-distance weighting method [160].

Registration methods used in CAD systems: Studies presenting CAD pipeline incorporating an automatic registration procedure are summarized in Tab. 3.4.

Ampeliotis *et al.* in [9, 10] did not use the framework as presented in Fig. 3.8 to register 2D T₂-W and DCE images. By using image symmetries and the MSE metric, they find the parameters of an affine transformation but without using a

3.1 Image regularization framework

Table 3.4: Classification of the different registration methods used in the CAD systems reviewed. Acronyms: gradient descent (GD), Nelder-Mead (NM).

Study index	Modality registered	Type	Geometric model		Similarity measure			Optimizer	
			Affine	Elastic	MSE	MI	CMI	GD	L-BFGS-B
[9, 10]	T ₂ -W - DCE	2D	✓	—	✓	—	—	—	—
[73]	T ₂ -W - DW	2D	✓	✓	—	—	—	—	—
[73]	T ₂ -W - DCE	2D	✓	✓	—	✓	—	✓	—
[258, 260]	T ₂ -W - DCE	2D	✓	—	—	✓	—	—	—
[261]	T ₂ -W - DCE - DW	3D	✓	—	—	—	✓	✓	—
[263]	T ₂ -W - DCE	3D	✓	—	—	✓	—	—	—
[265]	T ₂ -W - DCE	3D	✓	✓	—	✓	—	—	✓

Notes:

—: not used or not mentioned.

✓: used or implemented.

common objective function. They were finding independently and sequentially the scale factor, the rotation and finally the translation.

Giannini *et al.* [73] used also a in-house registration method for 2D T₂-W and DW images using an affine model. The bladder is first segmented in both modalities in order to obtain its contours and to focus the registration.

Giannini *et al.* [73] and also Vos *et al.* [265] used the same framework which is based on finding an affine transformation to register the T₂-W and DCE images using MI [203]. Then, an elastic registration using B-spline takes place using the affine parameters to initialize the geometric model with the same similarity measure. However, the approaches differ regarding the choice of the optimizer since a gradient descent is used in [73] and the same optimization problem is tackled via quasi-Newton method in [265]. Moreover, Giannini *et al.* [73] performed a 2D registration whereas Vos *et al.* [265] registered 3D volumes.

Viswanath *et al.* in [258, 260] as well as Vos *et al.* [263] performed an affine registration using the MI as similarity measure to correct the misalignment between T₂-W and DCE images. The choice of the optimizer was not specified. Viswanath *et al.* [258, 260] focused on 2D registration while Vos *et al.* [263] performed 3D registration.

3. REVIEW OF CADE AND CADX FOR CAP

Table 3.5: Overview of the CADe strategies employed in CAD systems.

CADe: ROIs selection strategy	References
All voxels-based approach	[14, 15, 73, 110, 144, 145, 154, 155, 175, 176, 180, 229, 233, 234, 235, 236, 237, 238, 239, 258, 259, 260, 261, 262]
Lesions candidate detection	[138, 140, 141, 266]

Finally, Viswanath *et al.* in [261] performed a 3D registration with the three modalities, T₂-W and DCE and DW MRI, by using an affine transformation model combined with the CMI similarity measure as presented in [38]. Moreover, in this latter work, the authors employed gradient descent [38] employed gradient descent approach to solve this problem but suggested Nelder-Mead simplex and quasi-Newton method as other solutions.

3.2 Image classification framework

3.2.1 CADe: ROIs detection/selection

As discussed in the introduction and shown in Fig. 2.1, the image classification framework is often composed of a CADe and a CADx. In this section, we will focus on studies embedding a CADe in their framework. Two approaches are considered to define a CADe (see Tab. 3.5): (i) voxel-based delineation and (ii) lesion segmentation. The first strategy, which concerns the majority of the studies reviewed (see Tab. 3.5), is in fact linked to the nature of the classification framework [14, 15, 73, 110, 144, 145, 154, 155, 175, 176, 180, 229, 233, 234, 235, 236, 237, 238, 239, 258, 259, 260, 261, 262]. All voxels are considered as a possible lesion and the output of the framework will be pixels classified as lesion and non lesion. The second group of methods is composed of method implementing a lesion segmentation algorithm to delineate potential candidates to further obtain a diagnosis through the CADx. This approach was borrowed from other application areas such as breast cancer. These methods are in fact very similar to the

classification framework used in CADx later.

Vos *et al.* [266] highlighted lesion candidates by detecting blobs in the ADC map. These candidates were filtered using some *a priori* criteria such as SI or diameter. As mentioned in Sect. 2.2.6 (see also Tab. 2.1), CaP can be interpreted as region of lower SI in ADC map. Hence, blob detectors are suitable to highlight these regions. Blobs are detected in a multi-resolution scheme, by computing the three main eigenvalues $\{\lambda_{\sigma,1}, \lambda_{\sigma,2}, \lambda_{\sigma,3}\}$ of the Hessian matrix, for each voxel location of the ADC map at a specific scale σ [131]. The probability p of a voxel \mathbf{x} being a part of a blob at the scale σ is given by:

$$P(\mathbf{x}, \sigma) = \begin{cases} \frac{\|\lambda_{\sigma,3}(\mathbf{x})\|^2}{\|\lambda_{\sigma,1}(\mathbf{x})\|} , & \text{if } \lambda_{\sigma,k}(\mathbf{x}) > 0 \text{ with } k = \{1, 2, 3\} , \\ 0 , & \text{otherwise .} \end{cases} \quad (3.25)$$

The fusion of the different scales is computed as:

$$L(\mathbf{x}) = \max P(\mathbf{x}, \sigma), \forall \sigma . \quad (3.26)$$

The candidate blobs detected are then filtered depending on its appearance (cf. maximum of the likelihood of the region, diameter of the lesion) and their SI in ADC and T₂-W images. The detected regions are then used as inputs for the CADx.

Litjens *et al.* in [140] used a pattern recognition approach in order to delineate the ROIs. A blobness map was calculated in the same manner as in [265] using the multi-resolution Hessian blob detector on the ADC map, T₂-W and pharmacokinetic parameters maps (see Sect. 3.2.2 for details about those parameters). Additionally, the position of the voxel $\mathbf{x} = \{x, y, z\}$ was used as a feature as well as the Euclidean distance of the voxel to the prostate center. Hence, the feature vectors were composed of eight features and a support vector machines (SVM) classifier was trained using a radial basis function (RBF) kernel (see Sect. 3.2.4 for more details).

Subsequently, Litjens *et al.* in [141] modified this approach by including only features related to the blob detection on the different maps as well as the original SIs of the parametric images. Two new maps were introduced based on texture. Instead of a SVM classifier, a k -nearest neighbour (k -NN) classifier was used.

3. REVIEW OF CADE AND CADx FOR CAP

The candidate regions were then extracted by performing a local maxima detection followed by post-processing region-growing and morphological operations.

3.2.2 CADx: Feature detection

Discriminative features which can be used to recognize CaP from healthy tissue have to be first detected. This processing is known in computer vision as feature extraction. However, feature extraction is also the name given in pattern recognition to some types of dimension reduction methods which will be presented next. In order to avoid confusion between these two aspects, in this survey, the procedure “detecting” or “extracting” features from images and signals will be defined as feature detection. This section will summarize the different strategies employed for this task. The features used in the studies are summarized in Table. ??.

3.2.2.1 Image-based features

This section will focus on image-based features detection. Two main strategies to detect features have been identified and used for the purpose of our classification: (i) voxel-wise detection and (ii) region-wise detection.

Voxel-wise detection: This strategy refers to the fact that a feature is extracted at each voxel location. CaP as previously discussed (see Tab. 2.1) can be discerned due to SI changes. Hence, intensity-based features are one of the most common features used to build the feature vector which has to be classified [9, 10, 14, 15, 37, 117, 144, 166, 167, 258, 261]. This type of feature consists simply of the SI of each voxel of the different MRI modalities.

Edge based features have also been used to detect SI changes. Each feature is computed by convolving the original image with an edge operator. Three of these operators are used: (i) Prewitt operator [190], (ii) Sobel operator [218] and (iii) Kirsch operator [114]. Results obtained with these operators vary, due to their different kernels. These features are commonly incorporated in the feature vector for further classification in the CAD systems reviewed [166, 167, 236, 237, 239, 259, 261].

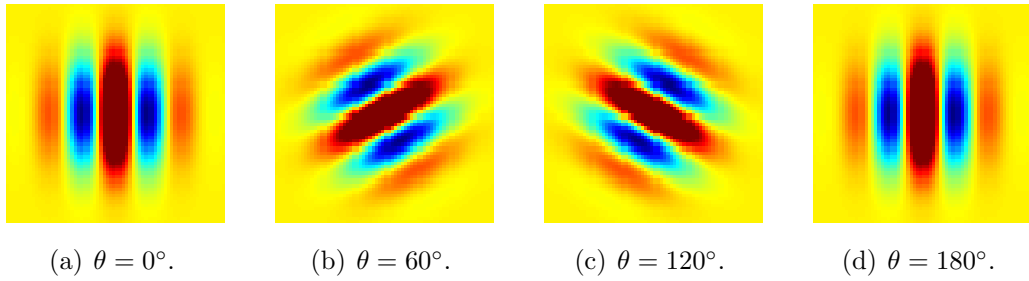


Figure 3.10: Illustration of four different Gabor filters varying their orientations θ .

Gabor filters [52, 71] offer another approach to extract information related to edges and texture and were integrated in three different CAD for CaP [238, 258, 262]. A Gabor filter is defined by the modulation of a Gaussian function with a sinusoid which can be further rotated. Hence, a Gabor filter g can be formalized as:

$$g(x, y; \theta, \psi, \sigma, \gamma) = \exp\left(-\frac{x'^2 + \gamma^2 y'^2}{2\sigma^2}\right) \cos\left(2\pi \frac{x'}{\lambda} + \phi\right), \quad (3.27)$$

with

$$\begin{aligned} x' &= s(x \cos \theta + y \sin \theta) , \\ y' &= s(-x \sin \theta + y \cos \theta) , \end{aligned}$$

where λ is the wavelength of the sinusoidal factor, θ represents the orientation of the Gabor filter, ψ is the phase offset, σ is the standard deviation of the Gaussian envelope, γ is the spatial aspect ratio and s is the scale factor. To perform Gabor analysis to extract features for a classification scheme, a bank of Gabor filters is usually created with different angles, scale and dilatations (see Fig. 3.10) and then convolved with the image.

Texture-based features provide other characteristics discerning CaP from healthy tissue. The most common texture analysis for image classification are co-occurrence matrices with their related statistics which were proposed in [88] and are commonly used in CAD systems [13, 166, 167, 236, 237, 239, 258, 259, 261, 262]. At each voxel, a neighbourhood is defined around this center and a gray-level

3. REVIEW OF CADE AND CADX FOR CAP

co-occurrence matrix is built by selecting a pair of voxels based on a defined distance and angle. Then, using this co-occurrence matrix, a set of features can be computed based on the statistics describing the texture around each voxel. Computation of these features is presented in Tab. 3.6.

Fractal analysis and more precisely a local estimation of the fractal dimension [20] describing the texture roughness at a specific location was used in [145]. A wavelet-based method in a multi-resolution framework was used to estimate the fractal dimension. Cancerous tissue were characterized to have a higher fractal dimension than healthy tissue.

Chan *et al.* [37] described the texture using the frequency signature via the discrete cosine transform (DCT) [2]) defining a neighbourhood of 7×7 pixels for each of the modalities that they used. The DCT allows to decompose a portion of image into a coefficients space where few of these coefficients encoded the visually significant information. The DCT coefficients are computed such as:

$$C_{k_1, k_2} = \sum_{m=0}^{M-1} \sum_{n=0}^{N-1} p_{m,n} \cos \left[\frac{\pi}{M} \left(m + \frac{1}{2} \right) k_1 \right] \cos \left[\frac{\pi}{N} \left(n + \frac{1}{2} \right) k_2 \right], \quad (3.28)$$

where C_{k_1, k_2} is the DCT coefficient at the position k_1, k_2 , M and N are the dimension of the neighbourhood and $p_{m,n}$ is the pixel SI at the position $p_{m,n}$.

Viswanath *et al.* [262] projected T₂-W images into the wavelet space, using Haar wavelet, and used the coefficients obtained from the decomposition as features.

Finally Litjens *et al.* in [140] computed the texture map based on T₂-W images using a Gaussian filer bank.

Region-wise detection: Unlike the previous section, another strategy is to study an entire region and extract characteristic features corresponding to this region. The most common approach reviewed can be classified as statical methods. First a feature map is computed for the whole image instaed of using single voxels. Then, ROIs are defined and statistics are extracted from each of these regions. The most widely used statistics is based on percentiles and is widely used [13, 140, 141, 184, 236, 237, 239, 258, 259, 261, 262, 263, 264, 265, 266?]. The percentile used

3.2 Image classification framework

Table 3.6: The fourteen statistical features for texture analysis commonly computed from the gray level co-occurrence matrix p as presented by [88].

Statistical features	Formula
Angular second moment	$\sum_i \sum_j p(i, j)^2$.
Contrast	$\sum_{n=0}^{N_g-1} n^2 \{ \sum_{i=1}^{N_g-1} \sum_{j=1}^{N_g-1} p(i, j) \} , i - j = n$.
Correlation	$\frac{\sum_i \sum_j (ij)p(i, j) - \mu_x \mu_y}{\sigma_x \sigma_y}$.
Variance	$\sum_i \sum_j (i - \mu)^2 p(i, j)$.
Inverse difference moment	$\sum_i \sum_j \frac{1}{1 + (i - \mu)^2} p(i, j)$.
Sum average	$\sum_{i=2}^{2N_g} i p_{x+y}(i)$.
Sum variance	$\sum_{i=2}^{2N_g} (i - f_s)^2 p_{x+y}(i)$.
Sum entropy	$-\sum_{i=2}^{2N_g} p_{x+y}(i) \log p_{x+y}(i)$.
Entropy	$-\sum_i \sum_j p(i, j) \log p(i, j)$.
Difference variance	$\sum_{i=0}^{N_g-1} i^2 p_{x-y}(i)$.
Difference entropy	$-\sum_{i=0}^{N_g-1} p_{x-y}(i) \log p_{x-y}(i)$.
Info. measure of corr. 1	$\frac{S(X; Y) - S_1(X; Y)}{\max(S(X), S(Y))}$.
Info. measure of corr. 2	$\sqrt{(1 - \exp[-2(H_2(X; Y) - H(X; Y))])}$.
Max. corr. coeff.	$\sqrt{\lambda_2}$, of $Q(i, j) = \sum_k \frac{p(i, k)p(j, k)}{p_x(i)p_y(k)}$.

3. REVIEW OF CADE AND CADX FOR CAP

is usually manually determined observing the distribution and corresponds to the best discriminant value differentiating malignant and healthy tissue. In addition, statistic-moments such as mean, standard deviation, kurtosis and skewness are also used [9, 10, 13, 166, 167, 184]. Litjense *et al.* in [?] also introduced a feature based on symmetry. They compute the mean of a candidate lesion as well as its mirrored counter-part and compute the quotient as feature.

Another subset of features are anatomic which were also used in [141, 154?]. Litjense *et al.* in [? ?] computed the volume, compactness and sphericity related to the region to integrate it in their feature vector. Matulewicz *et al.* [154] introduced four features corresponding to the percentage of tissue belonging to the regions PZ, CG, periurethral region or outside prostate region for the considered ROI.

In contrast to anatomical are histogram-based features. For instance, Liu *et al.* [142] introduced four different types of histogram-based features. The first type corresponds to the histogram of the SI of the image. The second type is the histogram of oriented gradient (HOG) [51]. HOG descriptor describes the local shape of the object of interest by using distribution of gradient directions. This descriptor is extracted mainly in three steps. First the gradient image and its corresponding magnitude and direction are computed. Then, the ROI is divided into cells and an oriented-based histogram is generated for each cell. At each pixel location, the orientation of the gradient will vote for a bin of the histogram and this vote is weighted by the magnitude of the same gradient. Finally, The cells are grouped into block and each block is normalized. The third histogram-based type used in [142] was shape context [19]. The shape context is also a way to describe the shape of an object of interest. First, a set of points defining edges have to be detected and for each point of each edge, a log-polar-based histogram is computed using the relative points distribution. The last set of histogram-based feature extracted is based on the framework described in [274] which is using the Fourier transform of the histogram created via local binary pattern (LBP) [172]. LBP is generated by comparing the value of the central pixel with its 8-connected neighbours. Then, in the ROI, the histogram of the LBP distribution is computed. The discrete fourier transform (DFT) of the LBP histogram is used to make the feature invariant to rotation.

The last group of region-based feature is based on fractal analysis. The features proposed are based on estimating the fractal dimension which is a statistical index representing the complexity of what is analysed. Lv *et al.* [147] proposed two features based on fractal dimension: (i) texture fractal dimension and (ii) histogram fractal dimension. The first feature is based on estimating the fractal dimension on the SI of each image. Hence, this feature is a statistical characteristic of the image roughness. The second fractal dimension is estimated in the PDF of each image and characterises the complexity of the PDF. Lopes *et al.* [145] proposed a 3D version to estimate the fractal dimension of a volume using wavelet decomposition.

3.2.2.2 DCE-based features

DCE-MRI is more commonly based on a SI analysis over time as presented in Sect. 2.2.3. In this section the features extracted for DCE-MRI analysis are presented.

Whole-spectra approach: Some studies are using the whole DCE time series as feature vector [9, 10, 238, 258, 259]. In some cases, the high-dimensional feature space is reduced using dimension reduction methods as it will be presented in the next section (see Sect. 3.2.3).

Semi-quantitative approach: Semi-quantitative approaches are based on mathematically modelling the DCE time series. The parameters modelling the signal are commonly used, mainly due to the simplicity of their computation. Parameters included in semi-quantitative analysis are summarized in Tab. 3.7 and also graphically depicted in Fig. 3.11. A set of time features corresponding to specific amplitude level (start, maximum and end) are extracted. Then, derivative and integral features are also considered as discriminative and are commonly computed.

Quantitative approach: As presented in Sect. 2.2, quantitative approaches correspond to mathematical-pharmacokinetic models based on physiological exchanges. Four different models have been used in CAD for CaP systems. The

3. REVIEW OF CADE AND CADX FOR CAP

Table 3.7: Parameters used as features for a DCE semi-quantitative analysis in CAD systems.

Semi-quantitative features	Explanations
<i>Amplitude features:</i>	
S_0	Amplitude at the onset of the enhancement
S_{\max}	Amplitude corresponding to 95% of the maximum amplitude
S_p	Amplitude corresponding to the maximum amplitude
S_f	Amplitude at the final time point
<i>Time features:</i>	
t_0	Time at the onset of the enhancement
t_{\max}	Time corresponding to 95% of the maximum amplitude
t_p	Time corresponding to the maximum amplitude
t_f	Final time
t_{tp}	Time to peak which is the time from t_0 to t_p
<i>Derivatives and integral features:</i>	
WI	Wash-in rate corresponding to the signal slope from t_0 to t_m or t_p
WO	Wash-out rate corresponding to the signal slope from t_m or t_p to t_f
$IAUC$	Initial area under the curve which is the area between t_0 to t_f

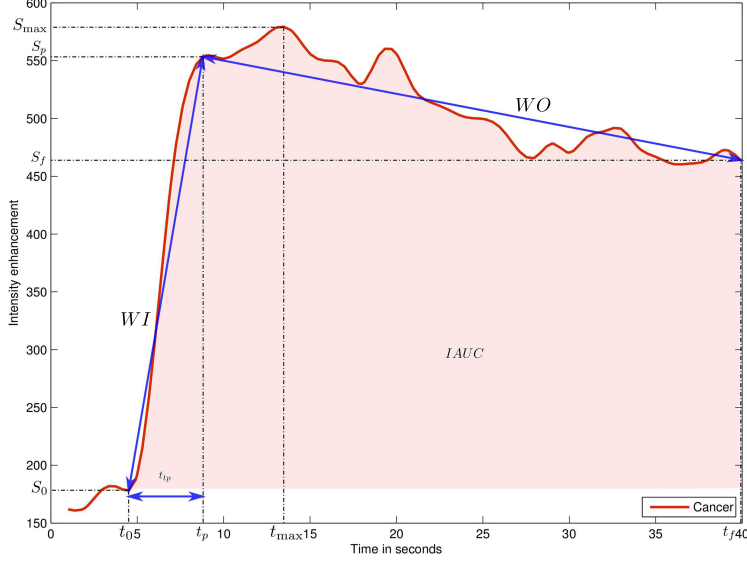


Figure 3.11: Graphical representation of the different semi-quantitative features used for DCE-MRI analysis.

most common model reviewed was the *Brix model* [14, 15, 144, 175, 176, 229]. This model is formalized such as:

$$\frac{S(t)}{S(0)} = 1 + Ak_{ep} \left(\frac{\exp(-k_{ep}t) - \exp(-k_{el}t)}{k_{el} - k_{ep}} \right), \quad (3.29)$$

where $S(\cdot)$ is the DCE signal, A is the parameter simulating the tissue properties, k_{el} is the parameter related to the first-order elimination from the plasma compartment and k_{ep} is the parameter of the transvascular permeability. These parameters (k_{ep} , k_{el} , A) are computed from the MRI data and used as features.

Another model is Tofts model [241] which was used in [73, 117, 155, 166, 167]. In this model, the DCE signal relative to the concentration is presented as:

$$C_t(t) = v_p C_p(t) + K_{trans} \int_0^t C_p(\tau) \exp(-k_{ep}(t - \tau)) d\tau, \quad (3.30)$$

where $C_t(\cdot)$ is the concentration of the medium, $C_p(\cdot)$ is the AIF which have to be estimated independently, K_{trans} is the parameter related to the diffuse transport of media across the capillary endothelium, k_{ep} is the parameter related to the

3. REVIEW OF CADE AND CADX FOR CAP

exchanges back into the vascular space and v_e is the extravascular-extracellular space fraction defined such that $v_e = 1 - v_p$. In this model, parameters K_{trans} , k_{ep} and v_e are computed and used as features.

Mazzetti *et al.* [155] and Giannini *et al.* [73] used the Weibull function in different empirical model based on West-like function and referred to as the phenomenological universalities model [35] defined by three parameters β , a_0 , and r (see Eq. 3.31).

$$S(t) = \exp \left[rt + \frac{1}{\beta} a_0 - r (\exp(\beta t) - 1) \right], \quad (3.31)$$

For all these models, the parameters are inferred using an optimization curve fitting approach.

3.2.2.3 MRSI-based features

Whole spectra approach: As in the case of DCE analysis, one common approach is to incorporate the whole MRSI spectra in the feature vector for classification [110, 154, 180, 233, 235, 236, 237, 239, 258]. Sometimes post-processing involving dimension reduction methods is performed to reduce the complexity during the classification as it will be presented in Sect. 3.2.3.

Quantification approach: We can reiterate that in MRSI only few biological markers (cf., choline, creatine and citrate metabolites mainly) are known to be useful to discriminate CaP and healthy tissue. Then, concentrations of these metabolites can be considered as a feature used for classification. In order to perform this quantification, four different approaches have been used. The QUEST [198], AMARES [251] and VARPRO [46] models were used in [110]. They are all time-domain quantification methods varying by the type of pre-knowledge embedded and the optimization approaches used to solve the quantification problem. Unlike the time-domain quantification approaches, Parfait *et al.* [180] used the LcModel approach [191] which solves the optimization problem in the frequency domain.

Although Parfait *et al.* [180] used each metabolite concentration individually, other authors such as Kelm *et al.* [110] proposed to compute relative concentrations

as the ratio of the choline plus creatine to citrate (see Eq. (3.32)) or the ratio of citrate to choline plus creatine plus citrate (see Eq. (3.33)).

$$R_1 = \frac{[\text{Cho}] + [\text{Cr}]}{[\text{Cit}]} . \quad (3.32)$$

$$R_2 = \frac{[\text{Cit}]}{[\text{Cho}] + [\text{Cr}] + [\text{Cit}]} , \quad (3.33)$$

where Cit, Cho and Cr are the concentration of citrate, choline and creatine respectively.

Wavelet decomposition approach: Tiwari *et al.* [238] performed a wavelet packet decomposition [45] of the spectra with the Haar wavelet basis function and used its coefficients as features.

3.2.3 CADx: Feature selection and feature extraction

As presented in the previous section, a wide variety of features can be computed (see Tab. ??). This often leads from multi-parametric MRI data to a high complexity feature space which might mislead or corrupt the classifier which used for training. Thus, it is of interest to reduce the number of dimensions before proceeding to the classification task. The strategies used can be grouped as: (i) feature selection and (ii) feature extraction. In this section only the methods used in CAD system are presented and summarized in Table. 3.8.

3.2.3.1 Feature selection

The feature selection strategy is based on selecting the most discriminative feature dimensions of the high-dimensional space. Thus, the low-dimensional space is then composed of a subset of the original features detected. In this section, methods employed in the studies reviewed will be briefly presented. More extensive reviews specific to feature selection can be found in [205].

Naif *et al.* [166, 167] make use of the p-value by using the independent two-sample t-test with equal mean for each feature dimension. In this statistical test, there are two classes: CaP and healthy tissue. Hence, for each particular feature,

3. REVIEW OF CADE AND CADX FOR CAP

Table 3.8: Overview of the feature selection and extraction methods used in CAD systems.

Dimension reduction methods	References
<i>Feature selection:</i>	
Statistical test	[166, 167, 266]
MI-based methods	[166, 167, 263]
<i>Feature extraction:</i>	
Linear mapping	
PCA	[234, 235]
Non-linear mapping	
Laplacian eigenmaps	[233, 235, 236, 237, 259, 261]
LLE and LLE-based	[234, 235, 258, 259]

the distribution of each class can be characterized by their means \bar{X}_1 and \bar{X}_2 and standard deviation s_{X_1} and s_{X_2} , respectively. Therefore, the null hypothesis test is based on the fact that these both distribution means are equal. The t-statistic used to verify the null hypothesis is formalized such that:

$$t = \frac{\bar{X}_1 - \bar{X}_2}{s_{X_1 X_2} \cdot \sqrt{\frac{1}{n_1} + \frac{1}{n_2}}}, \quad (3.34)$$

$$s_{X_1 X_2} = \sqrt{\frac{(n_1 - 1)s_{X_1}^2 + (n_2 - 1)s_{X_2}^2}{n_1 + n_2 - 2}},$$

where n_1 and n_2 are the number of samples in each class. From Eq. (3.34), it can be seen that more the means of the class distribution diverge, the larger the t-statistic t will be, implying that this particular feature is more relevant and able to make the distinction between the two classes.

The p -value statistic can be deduced from the t -test and corresponds to the probability of obtaining such an extreme test assuming that the null hypothesis is true ([81]). Hence, smaller the p -value, the more likely we are to reject the null hypothesis and keep more relevant features. Finally, the features can be ranked and the most significant features can be selected. However, this technique suffers

from a main drawback since it assumes that each feature is independent, which is unlikely to happen and introduces a high degree of redundancy in the features selected.

Vos *et al.* in [266] employed a similar feature ranking approach but make use of the Fisher discriminant ratio to compute the relevance of each feature dimension. Taking the aforementioned formulation, the Fisher discriminant ratio is formalized as the ratio of the interclass variance to the intraclass variance as:

$$F_r = \frac{\bar{X}_1 - \bar{X}_2}{s_{X_1}^2 + s_{X_2}^2} . \quad (3.35)$$

Hence, a relevant feature dimension can be selected when the interclass variance is maximum and the intraclass variance in minimum. Once the features are ordered, the authors select the feature dimensions with the larger Fisher discriminant ratio.

MI can also be used to select a subset of feature dimensions. This method was previously presented in Sect. 3.1.3 (see Eq. (3.23)). Peng *et al.* [183] introduced two main criteria to select the feature dimensions: (i) maximal relevance and (ii) minimum redundancy. Maximal relevance criterion is based on the paradigm that the classes and the feature dimension which has to be selected have to share a maximal MI and can be formalized:

$$\arg \max Rel(\mathbf{x}, c) = \frac{1}{|\mathbf{x}|} \sum_{x_i \in \mathbf{x}} MI(x_i, c) , \quad (3.36)$$

where $\mathbf{x} = \{x_i, i = 1, \dots, d\}$ is a feature vector of d dimensions and c is the class considered. As in the previous method, using maximal relevance criterion alone will imply independence between each feature dimension which is usually not true. Minimal redundancy criterion will force selection of a new feature dimension which shares as little as possible MI with previously selected feature dimension and is formalized as:

$$\arg \min Red(\mathbf{x}) = \frac{1}{|\mathbf{x}|^2} \sum_{x_i, x_j \in \mathbf{x}} MI(x_i, x_j) . \quad (3.37)$$

Combination of these two criteria is known as minimum redundancy maximum relevance (mRMR)¹ ([183]) and are computed as a difference or quotient of Eqs.

¹mRMR implementation can be found at: <http://penglab.janelia.org/proj/mRMR/>

(3.36) and (3.37). Authors in [166, 167] make use of maximal relevance criterion alone and also of both mRMR difference and quotient criterion. Viswanath *et al.* [262] also reduced their feature vector via mRMR difference and quotient.

3.2.3.2 Feature extraction

The feature extraction strategy is related to dimension reduction methods but not selecting discriminative features. Instead, these methods aim at mapping the data from the high-dimensional space into a low-dimensional space created to maximize the separability between the classes. The mapping can be performed in a linear or a non-linear manner. Again, only methods employed in CAD system will be reviewed in this section. We refer the reader to [65] for a full review of feature extraction techniques.

PCA is the most commonly used linear mapping method in CAD systems. PCA is based on finding the orthogonal linear transform mapping the original data into a low-dimensional space. The space is defined such that the linear combinations of the original data with the k^{th} greatest variances will lie on the k^{th} principal components [105]. The principal components can then be computed by using the eigenvectors-eigenvalues decomposition of the covariance matrix. Let \mathbf{x} denote the data matrix. Then the covariance matrix and eigenvectors-eigenvalues decomposition are defined as in Eq. (3.38), and Eq. (3.39), respectively. The eigenvectors-eigenvalues decomposition can be formalized as:

$$\Sigma = \mathbf{x}^T \mathbf{x} . \quad (3.38)$$

$$\mathbf{v}^{-1} \Sigma \mathbf{v} = \Lambda , \quad (3.39)$$

where \mathbf{v} are the eigenvectors matrix and Λ is a diagonal matrix containing the eigenvalues.

It is then possible to find the new low-dimensional space by sorting the eigenvectors using the eigenvalues and finally selecting the largest eigenvalues. The total variation that is the sum of the principal eigenvalues of the covariance matrix ([65]), usually corresponds to the 95% to 98% of the cumulative sum of the eigenvalues. Tiwari *et al.* in [234, 235, 238] used PCA in order to reduce the dimensionality of

their feature vector. Non-linear mapping was also used for dimension reduction. It is mainly based on Laplacian eigenmaps and locally linear embedding (LLE) methods. Laplacian eigenmaps¹, also referred as spectral clustering in computer vision, aim to find a low-dimensional space in which the proximity of the data should be preserved from the high-dimensional space [18, 214]. Thus, two adjacent data points in the high-dimensional space should also be close in the low-dimensional space. Similarly, two distant data points in the high-dimensional space also should be distant in the low-dimensional space. To compute this projection, an adjacency matrix is defined as:

$$W(i, j) = \exp \|\mathbf{x}_i - \mathbf{x}_j\|_2 , \quad (3.40)$$

where \mathbf{x}_i and \mathbf{x}_j are the two samples considered. Then, the low-dimensional space will be found by solving the generalized eigenvectors-eigenvalues problem:

$$(D - W)\mathbf{y} = \lambda D\mathbf{y} , \quad (3.41)$$

where D is a diagonal matrix such that $D(i, i) = \sum_j W(j, i)$. Finally the low-dimensional space is defined by the k eigenvectors of the k smallest eigenvalues [18]. Tiwari *et al.* in [233, 235, 236] and Viswanath *et al.* in [259] used this spectral clustering to project their feature vector into a low-dimensional space. The feature space in these studies is usually composed of features extracted from a single or multiple modalities and then concatenated before applying the Laplacian eigenmaps dimension reduction technique.

Tiwari *et al.* in [235, 239] used a slightly different approach by combining the Laplacian eigenmaps techniques with a prior multi-kernel learning strategy. First, multiple features were extracted for multiple modalities. The features of a single modality were then mapped to a higher dimensional space via the Kernel trick ([3]) and more precisely using a Gaussian kernel. Then, each kernel associated with each modality was linearly combined to obtain a combined kernel K , which leads to computation of the adjacency matrix W . Finally the same scheme as in

¹Laplacian eigenmap implementation is available at: <http://www.cse.ohio-state.edu/~mbelkin/algorithms/algorithms.html>

3. REVIEW OF CADE AND CADX FOR CAP

Laplacian eigenmaps is applied. However, in order to use the combined kernel, Eq. (3.41) is rewritten as:

$$K(D - W)K^T \mathbf{y} = \lambda KDK^T \mathbf{y} . \quad (3.42)$$

Which can be solved as a generalized eigenvectors-eigenvalues problem as previously. Viswanath *et al.* in [261] used Laplacian eigenmaps inside a bagging framework in which multiple embeddings are generated by successively selecting feature dimensions.

READ THIS SECTION and CHECK THE DEFINITIONS

LLE¹ is another common non-linear dimension reduction technique widely used, first proposed in [202]. LLE is based on the fact that a data point in the feature space can be characterized by its neighbours. Thus, it was proposed to represent each data point in the high-dimensional space as the linear combination of its k -nearest neighbours. This can be expressed as:

$$\hat{\mathbf{x}}_i = \sum_j W(i, j) \mathbf{x}_j , \quad (3.43)$$

where $\hat{\mathbf{x}}_i$ are the data point estimated using its neighbouring data points \mathbf{x}_j , and W is the weight matrix. The weight matrix W is estimated using a least square optimization scheme (see Eq. (3.44)).

$$\begin{aligned} \hat{W} &= \arg \min_W \sum_i |\mathbf{x}_i - \sum_j W(i, j) \mathbf{x}_j|^2 , \\ &\text{subject to } \sum_j W(i, j) = 1 , \end{aligned} \quad (3.44)$$

Then, the essence of LLE is to project the data into a low dimension space, while retaining the data organization. Thus, the projection into the low dimension space can be seen as an optimization problem as:

$$\hat{\mathbf{y}} = \arg \min_{\mathbf{y}} \sum_i |\mathbf{y}_i - \sum_j W(i, j) \mathbf{y}_j|^2 . \quad (3.45)$$

¹LLE implementation is available at: <http://www.cs.nyu.edu/~roweis/lle/code.html>

This optimization can be performed as an eigenvectors-eigenvalues problem by finding the k^{th} eigenvectors corresponding to the k^{th} smallest eigenvalues of the sparse matrix $(I - W)^T(I - W)$.

Tiwari *et al.* in [234] used a modified version of the LLE algorithm in which they applied LLE in a bagging approach with multiple neighbourhood sizes. The different embeddings obtained are then fused using the maximum likelihood (ML) estimation.

3.2.4 CADx: Classification

3.2.4.1 Classifier

Once the feature vector has been extracted and eventually the complexity reduced, it is possible to make a decision and classify this feature vector to belong to CaP or healthy tissue. Classification methods used in CAD system to distinguish these two classes are summarized in Table. 3.9. A full review of classification methods used in pattern recognition can be found in [22].

Rule-based method: Lv *et al.* [147] make use of a decision stump classifier to distinguish CaP and healthy classes. Puech *et al.* [192] detect CaP by implementing a given set of rules using a score medical decision making approach. The feature values are compared with a pre-defined threshold. Then, at each comparison, the final score is incremented or not, depending on the threshold and the final decision is taken depending of the final score.

Clustering methods: k -nearest neighbour (k -NN) is one of the simplest supervised machine learning classification methods. In this method, a new unlabelled vector is assigned to the most represented class from its k nearest-neighbours in the feature space. The parameter k is usually an odd number in order to avoid any tie case. k -NN was one of the method used by [166, 167] mainly to make a comparison with different machine learning techniques. Litjens *et al.* [141] used this method to roughly detect potential CaP voxels before performing a region-based classification.

3. REVIEW OF CADE AND CADX FOR CAP

Table 3.9: Overview of the classifiers used in CAD systems.

Classifier	References
<i>Rule-based method:</i>	[147, 192]
<i>Clustering methods:</i>	
<i>k</i> -means clustering	[233, 234, 235]
<i>k</i> -NN	[141, 166, 167]
<i>Linear model classifiers:</i>	
LDA	[13, 37, 138, 166, 167, 266]
Logistic regression	[110, 117]
<i>Non-linear classifier:</i>	
QDA	[262]
<i>Probabilistic classifier:</i>	
Naive Bayes	[73, 155, 166, 167]
<i>Ensemble learning classifiers:</i>	
AdaBoost	[138, 145]
Random forest	[110, 138, 238, 239, 260]
Probabilistic boosting tree	[235, 237, 238]
<i>Kernel method:</i>	
Gaussian processes	[110]
<i>Sparse kernel methods:</i>	
SVM	[14, 15, 37, 140, 141, 142, 145, 166, 167, 175, 176, 180, 184, 229, 238, 263, 264, 265, 266]
RVM	[175, 176]
<i>Neural network:</i>	
Multiple layer perceptron	[154, 180]
Probabilistic neural network	[9, 10, 261]
<i>Graphical model classifiers:</i>	
Markov random field	[144, 176]
Conditional random field	[14, 15]

The k -means algorithm is an unsupervised clustering method in which the data is iteratively partitioned into k clusters. The discovery of the clusters is an iterative procedure. First k random centroids are defined in the feature space and each data point is assigned to the nearest centroid. Then, the centroid position for each cluster is updated by computing the mean of all the data points belonging to this particular cluster. Both assignment and updating are repeated until the centroids are stable. The number of clusters k is usually defined as the number of classes. This algorithm can also be used for “on-line” learning. In case that new data has to be incorporated, the initial centroid positions correspond to the results of a previous k -means training and is followed by the assignment-updating stage previously explained. Tiwari *et al.* [233, 235] used k -means in an iterative procedure. Three clusters were defined corresponding to CaP, healthy and non-prostate, respectively. k -means was applied iteratively and the voxels corresponding to the largest cluster were excluded under the assumption that it is assigned to “non-prostate” cluster. The algorithm stopped when the number of voxels in all remaining clusters were smaller than a given threshold.

Tiwari *et al.* in [234] and Viswanath *et al.* in [258, 259] used k -means in a repetitive manner in order to be less sensitive to the centroids initialisation. Thus, k clusters were generated T times. The final assignment was performed by majority voting using a co-association matrix as proposed in [66].

Linear model classifiers: Linear discriminant analysis (LDA) can be used as a classification method in which the optimal linear separation between two classes is found by maximizing the interclass variance and minimizing the intra-class variance[69]. The linear discriminant function is defined as:

$$\delta_k(\mathbf{x}_i) = \mathbf{x}_i^T \Sigma^{-1} \mu_k - \frac{1}{2} \mu_k^T \Sigma^{-1} \mu_k + \log(\pi_k) , \quad (3.46)$$

where \mathbf{x}_i is an unlabelled feature vector, Σ is the covariance matrix of the training data, μ_k is the mean vector of the class k and π_k is the prior probability of class k . To perform the classification, a sample \mathbf{x}_i will be assigned to the class which maximizes the discriminant function (see Eq. (3.47)). LDA has been used in

3. REVIEW OF CADE AND CADX FOR CAP

[13, 37, 166, 167, 266].

$$C(\mathbf{x}_i) = \arg \max_k \delta_k(\mathbf{x}_i) . \quad (3.47)$$

Logistic regression can be used to perform binary classification and can provide the probability of an observation to belong to a class. The posterior probability of one of the classes, c_1 , can be written as:

$$p(c_1|\mathbf{x}_i) = \frac{1}{1 + \exp(-\mathbf{w}^T \mathbf{x}_i)} , \quad (3.48)$$

with $p(c_2|\mathbf{x}_i) = 1 - p(c_1|\mathbf{x}_i)$ and where \mathbf{w} is the vector of the regression parameters allowing to obtain a linear combination of the input feature vector \mathbf{x}_i . Thus, an unlabelled observation \mathbf{x}_i will be assigned to the class which maximizes the posterior probability (see Eq.(3.49)).

$$C(\mathbf{x}_i) = \arg \max_k p(C = k|\mathbf{x}_i) . \quad (3.49)$$

From Eq. (3.48), one can see that the key to classification using logistic regression model is to infer the set of parameters \mathbf{w} through a learning stage in the training set. This vector of parameters \mathbf{w} can be inferred by finding the maximum likelihood estimates. This step can be performed through an optimization scheme, using a quasi-Newton method [32], which iteratively seeks for the local minimum in the derivative of Eq. (3.48). This method has been used to create a linear probabilistic model in [110, 192].

Non-linear model classifier: Viswanath *et al.* in [262] used quadratic discriminant analysis (QDA) instead of LDA. Unlike in LDA in which one assumes that the class covariance matrix Σ is identical for all the classes, in QDA, a covariance matrix Σ_k specific to each class is computed. Thus, Eq. (3.46) becomes:

$$\delta_k(\mathbf{x}_i) = \mathbf{x}_i^T \Sigma_k^{-1} \mu_k - \frac{1}{2} \mu_k^T \Sigma_k^{-1} \mu_k + \log(\pi_k) . \quad (3.50)$$

The classification scheme in the case of the QDA is identical to Eq. (3.47).

Probabilistic classifiers: The most commonly used classifier is the naive Bayes classifier which is a probabilistic classifier assuming independence between each feature dimension [199]. This classifier is based on Bayes' theorem:

$$p(C = k|\mathbf{x}) = \frac{p(C)p(\mathbf{x}|C)}{p(\mathbf{x})} , \quad (3.51)$$

where $p(C = k|\mathbf{x})$ is the posterior probability, $p(C)$ is the prior probability, $p(\mathbf{x}|C)$ is the likelihood and $p(\mathbf{x})$ is the evidence. However, the evidence term is usually discarded since it is not class dependent and plays the role of a normalization term. Hence, in a classification scheme, an unlabelled observation will be classified to the class which maximizes the posterior probability as:

$$C(\mathbf{x}_i) = \arg \max_k p(C = k|\mathbf{x}_i) , \quad (3.52)$$

$$p(C = k|\mathbf{x}_i) = p(C = k) \prod_{j=1}^n p(x_{ij}, |C = k) , \quad (3.53)$$

where d is the number of dimensions of the feature vector $\mathbf{x}_i = \{x_{i1}, \dots, x_{id}\}$. Usually, a model includes both the prior and likelihood probabilities and it is common to use an equal prior probability for each class or eventually a value based on the relative frequency derived from the training set. Regarding the likelihood probability, it is common to choose a Normal distribution to characterize each class. Thus, each class will be characterized by two parameters: (i) the mean and (ii) the standard deviation. These parameters can be inferred from the training set by using the ML approach.

The naive Bayes classifier has been used in [73, 155, 166, 167]. The Normal distribution was used as the likelihood probability for that model.

Ensemble learning classifiers: AdaBoost is an adaptive method based on an ensemble learning method and was initially proposed by [68]. AdaBoost linearly combines several weak learners resulting into a final strong classifier. A weak learner is defined as a classification method performing slightly better than random classification. Popular choices regarding the weak learner classifiers are: decision

3. REVIEW OF CADE AND CADX FOR CAP

stump, decision tree learners (cf., iterative dichotomiser 3 (ID3) [193], C4.5 [194], classification and regression tree (CART) [27]).

AdaBoost is considered as an adaptive method in the way that the weak learners are selected. The selection is performed in an iterative manner. At each iteration t , the weak learner selected h_t corresponds to the one minimizing the classification error on a distribution of weights D_t , that is associated with the training samples. Each weak learner is assigned a weight α_t as:

$$\alpha_t = \frac{1}{2} \ln \frac{1 - \epsilon_t}{\epsilon_t} , \quad (3.54)$$

where ϵ_t corresponds to the classification error rate of the weak learner on the distribution of weight D_t .

Before performing a new iteration, the distribution of weights D_t is updated such that the weights associated with the samples misclassified by h_t will be increased and the weights of well classified samples will decrease as shown in Eq. (3.55).

$$D_{t+1}(i) = \frac{D_t(i) \exp(-\alpha_t y_i h_t(\mathbf{x}_i))}{Z_t} , \quad (3.55)$$

where \mathbf{x}_i is the i^{th} sample corresponding to class y_i and Z_t is a normalization factor forcing D_{t+1} to be a probability distribution. This procedure allows us to select a weak learner at the next iteration $t + 1$ which will classify in priority previous misclassified samples. Thus, after T iterations, the final strong classifier corresponds to the linear combination of the weak learners selected and the classification is performed such that:

$$C(\mathbf{x}_i) = \text{sign} \left(\sum_{t=1}^T \alpha_t h_t(\mathbf{x}_i) \right) . \quad (3.56)$$

Lopes *et al.* [145] make use of the AdaBoost classifier to perform their classification while Litjens *et al.* in [138] used the GentleBoost variant [70] which provides a modification of the function affecting the weight at each weak classifier.

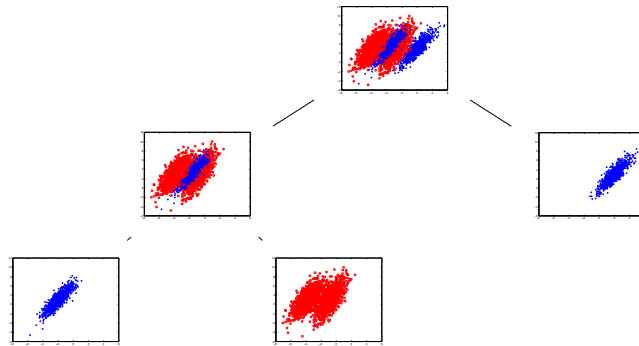


Figure 3.12: Representation of the capabilities of the probabilistic boosting tree algorithm to split at each node of the tree the positive and negative samples.

Random forest¹ is a classification method which is based on creating an ensemble of decision trees and was introduced by [26]. In the learning stage, multiple decision tree learners [27] will be trained. However, each decision tree will be trained with a different dataset. Each of these datasets corresponds to a bootstrap sample generated by randomly choosing n samples with replacement from the initially N samples available [59]. Then, randomization is also part of the decision tree growth. At each node of the decision tree, from the bootstrap sample of D dimensions, a number of $d \ll D$ dimensions will be randomly selected. Finally, the d^{th} dimension in which the classification error is minimum is used. This best “split” classifier is often evaluated using MI. Finally, each tree is grown as much as possible without using any pruning procedure. In the prediction stage, the unlabelled sample is introduced in each tree and each of them will assign a class to this sample. Finally, it is common to use a majority voting approach to choose the final class label. The random forest classifier has been used in [110, 138, 238, 239, 260].

Probabilistic boosting-tree is another ensemble learning classifier which shares principles with AdaBoost but using them inside a decision tree [245]. In the training stage, the probabilistic boosting-tree method grows a decision tree and at each node, a strong classifier is learnt in an almost comparable scheme to AdaBoost (see Eq. 3.56). Once the strong learner is trained, the training set will be split

¹Random forest implementation can be found at: http://www.stat.berkeley.edu/~breiman/RandomForests/cc_software.htm

3. REVIEW OF CADE AND CADX FOR CAP

into two subsets which will be used to train the next strong classifiers in the next descending nodes. Thus, three cases are conceivable to decide which branch to propagate each sample training \mathbf{x}_i :

- if $q(+1, \mathbf{x}_i) - \frac{1}{2} > \epsilon$ then \mathbf{x}_i is propagated to the right branch set and a weight $w_i = 1$ is assigned.
- if $q(-1, \mathbf{x}_i) - \frac{1}{2} > \epsilon$ then \mathbf{x}_i is propagated to the left branch set and a weight $w_i = 1$ is assigned.
- else \mathbf{x}_i will be propagated in both branches with $w_i = q(+1, \mathbf{x}_i)$ in the right branch and $w_i = q(-1, \mathbf{x}_i)$ in the left branch.

with $\mathbf{w} = w_i, i = \{1, \dots, N\}$ corresponding to distribution of weights, N the number of samples as in AdaBoost and $q(\cdot)$ is defined as:

$$q(+1, \mathbf{x}_i) = \frac{\exp(2H(\mathbf{x}_i))}{1 + \exp(2H(\mathbf{x}_i))}, \quad (3.57)$$

$$q(-1, \mathbf{x}_i) = \frac{\exp(-2H(\mathbf{x}_i))}{1 + \exp(-2H(\mathbf{x}_i))}. \quad (3.58)$$

Employing such a scheme tends to divide the data in such a way that positive and negative samples are naturally split as shown in Fig. 3.12. In the classification stage, the unlabelled sample \mathbf{x} is propagated through the tree, where at each node, it will be classified by each strong classifier previously learned and where an estimation of the posterior distribution will be computed. The posterior distribution will correspond to the sum of the posterior distribution at each node of the decision tree. The probabilistic boosting-tree classifier has been used in [236, 237, 238, 261].

Kernel method: A Gaussian process¹ for classification is a kernel method in which it is assumed that the data can be represented by a single sample from a

¹Gaussian process implementation can be found at: <http://www.gaussianprocess.org/gpml/code/matlab/doc/index.html>

multivariate Gaussian distribution [197]. In the case of linear logistic regression for classification, the posterior probability can be expressed as:

$$\begin{aligned} p(y_i|\mathbf{x}_i, \mathbf{w}) &= \sigma(y_i f(\mathbf{x}_i)) , \\ f(\mathbf{x}_i) &= \mathbf{x}_i^T \mathbf{w} , \end{aligned} \quad (3.59)$$

where $\sigma(\cdot)$ is the logistic function and \mathbf{w} are the parameters vector of the model. Thus, the classification using Gaussian processes is based on assigning a Gaussian process prior over the function $f(\mathbf{x})$ which will be characterized by a mean function \bar{f} and covariance function K . Therefore, in the training stage, the best mean and covariance functions have to be inferred in regard to our training data using a Newton optimization and a Laplacian approximation. The prediction stage can be performed in two stages. First, for a new observation \mathbf{x}_* , the corresponding probability $p(f(\mathbf{x}_*)|f(\mathbf{x}))$ can be computed such that:

$$\begin{aligned} p(f(\mathbf{x}_*)|f(\mathbf{x})) &= \mathcal{N}(K_* K^{-1} \bar{f}, K_{**} - K_* (K')^{-1} K_*^T) , \\ K' &= K + W^{-1} , \\ W &= \nabla \nabla \log p(\mathbf{y}|f(\mathbf{x})) , \end{aligned} \quad (3.60)$$

where K_{**} is the variance of the testing sample \mathbf{x}_* , K_* is the covariance of training-testing samples \mathbf{x} and \mathbf{x}_* . Then, the function $f(\mathbf{x}_*)$ is squashed using the sigmoid function and the probability of the class membership can be defined such that:

$$C(\mathbf{x}_*) = \sigma \left(\frac{\bar{f}(\mathbf{x}_*)}{\sqrt{1 + \text{var}(f(\mathbf{x}_*))}} \right) . \quad (3.61)$$

Only the work of [110] used Gaussian process for classification in MRSI data.

Sparse kernel methods: In a classification scheme using Gaussian processes, when a prediction has to be performed, the whole training data will be used to assign a label to the new observations. That is why this method is also called kernel method. Sparse kernel category is composed of methods which rely only on a few labelled observations of the training set to assign the label of new observations [22].

3. REVIEW OF CADE AND CADX FOR CAP

Support vector machines (SVM)¹ is a sparse kernel method aims at finding the best linear hyperplane (non-linear separation is discussed further) which separates two classes such that the margin between the two classes is maximized [252]. The margin is in fact the region defined by two hyperplanes splitting the two classes, such that there are no points lying in between. The distance between these two hyperplanes is equal to $\frac{2}{\|\mathbf{w}\|}$ where \mathbf{w} is the normal vector of the hyperplane splitting the classes. Thus, maximizing the margin is equivalent to minimizing the norm $\|\mathbf{w}\|$. Hence, this problem is solved by an optimization approach and formalized:

$$\begin{aligned} \arg \min_{\mathbf{w}} \quad & \frac{1}{2} \|\mathbf{w}^2\|, \\ \text{subject to} \quad & y_i(\mathbf{w} \cdot \mathbf{x}_i - b) \geq 1, \quad i = \{1, \dots, N\}, \end{aligned} \quad (3.62)$$

where \mathbf{x}_i is a training sample with is corresponding class label y_i . From Eq. (3.62), it is important to notice that only few points from the set of N points have to be selected which will later define the hyperplane. This can be introduced in the optimization problem using Lagrange multipliers α . All points which are not lying on the margin will be assigned a corresponding $\alpha_i = 0$, which is formalized as Eq. (3.63).

$$\arg \min_{\mathbf{w}, b} \max_{\alpha \geq 0} \left\{ \frac{1}{2} \|\mathbf{w}\|^2 - \sum_{i=1}^n \alpha_i [y_i(\mathbf{w} \cdot \mathbf{x}_i - b) - 1] \right\}. \quad (3.63)$$

The different parameters can be inferred using quadratic programming. This version of SVM is known as hard-margin since no points can lie in the margin area. However, it is highly probable to not find any hyperplane splitting the classes such as specified previously. Thus, a soft-margin optimization approach was proposed [48], where points can lie on the margin but at the cost of a penalty ξ_i which will be minimized in the optimization process suchthat:

$$\arg \min_{\mathbf{w}, \xi, b} \max_{\alpha, \beta} \left\{ \frac{1}{2} \|\mathbf{w}\|^2 + C \sum_{i=1}^n \xi_i - \sum_{i=1}^n \alpha_i [y_i(\mathbf{w} \cdot \mathbf{x}_i - b) - 1 + \xi_i] - \sum_{i=1}^n \beta_i \xi_i \right\}. \quad (3.64)$$

¹SVM implementation can be found at: <http://www.csie.ntu.edu.tw/~cjlin/libsvm/>

3.2 Image classification framework

The decision to assign the label to a new observation \mathbf{x}_i is taken such that:

$$C(\mathbf{x}_i) = \text{sign} \left(\sum_{n=1}^N \alpha_n (\mathbf{x}_n \cdot \mathbf{x}_i) + b_0 \right) , \quad (3.65)$$

where $\mathbf{x}_n | n = \{1, \dots, S\}$, S being the support vectors.

SVM can also be used as a non-linear classifier by performing a kernel trick [24]. The original data \mathbf{x} can be projected to a high-dimension space in which it is assumed that a linear hyperplane will split the classes. Different kernels are popular such as the RBF kernel, polynomial kernels or Gaussian kernel. In CAD for CaP systems, SVM is the most popular classification method and was used in a multitude of research works [14, 15, 37, 110, 140, 141, 142, 145, 166, 167, 175, 176, 180, 184, 229, 238, 263, 264, 265, 266].

Relevant vector machine (RVM) is a sparse version of Gaussian process previously presented and was proposed by [232]. RVM is identical to a Gaussian process with the following covariance function [195]:

$$K_{RVM}(\mathbf{x}_p, \mathbf{x}_q) = \sum_{j=1}^M \frac{1}{\alpha_j} \Phi_j(\mathbf{x}_p) \Phi_j(\mathbf{x}_q) , \quad (3.66)$$

where $\phi(\cdot)$ is a Gaussian basis function, $\mathbf{x}_i | i = \{1, \dots, N\}$ are the N training points and $\boldsymbol{\alpha}$ are the weights vector. As mentioned in [195], the sparsity regarding the relevance vector arises if $j\alpha_j^{-1} = 0$. The set of weights $\boldsymbol{\alpha}$ is inferred using the expectation maximization algorithm. Ozer *et al.* [175, 176] make use of RVM and make a comparison with SVM for the task of CaP detection.

Neural network: Multilayer perceptron is a feed-forward neural networks considered as the most successful model of this kind in pattern recognition [22]. The most well known model used is based on two layers where a prediction of an observation is computed as:

$$C(\mathbf{x}_n, w_{ij}^{(1)}, w_{kj}^{(2)}) = \sigma \left[\sum_{j=0}^M w_{kj}^{(2)} h \left(\sum_{i=0}^D w_{ij}^{(1)} x_{in} \right) \right] , \quad (3.67)$$

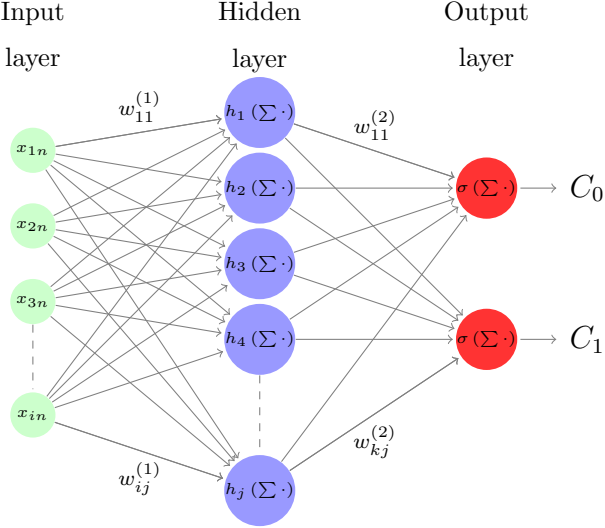


Figure 3.13: Representation of a neural network of the multilayer perceptron family.

where $h(\cdot)$ and $\sigma(\cdot)$ are two activation functions usually non-linear, $w_{ij}^{(1)}$ and $w_{kj}^{(2)}$ are the weights associated with the linear combination with the input feature \mathbf{x}_n and the hidden unit, respectively.

A graphical representation of this network is presented in Fig. 3.13. Relating Fig. 3.13 with Eq. (3.67), it can be noted that this network is composed of some successive non-linear mapping of the input data. First, a linear combination of the input vector \mathbf{x}_n is mapped into some hidden units through a set of weights $w_{ij}^{(1)}$. This combination becomes non-linear by the use of the activation function $h(\cdot)$ which is usually chosen to be a sigmoid function. Then, the output of the networks consists of a linear combination of the hidden units and the set of weights $w_{kj}^{(2)}$. This combination is also mapped non-linearly using an activation function $\sigma(\cdot)$ which is usually a logistic function. Thus, the training of such a network resides in finding the best weights $w_{ij}^{(1)}$ and $w_{kj}^{(2)}$ which will model the best our data. The error of this model can be computed as:

$$E(w_{ij}^{(1)}, w_{kj}^{(2)}) = \frac{1}{2} \sum_{n=1}^N \left(C(\mathbf{x}_n, w_{ij}^{(1)}, w_{kj}^{(2)}) - y(\mathbf{x}_n) \right)^2, \quad (3.68)$$

where $\mathbf{x}_n | n = \{1, \dots, N\}$ are the N training vectors with their corresponding class

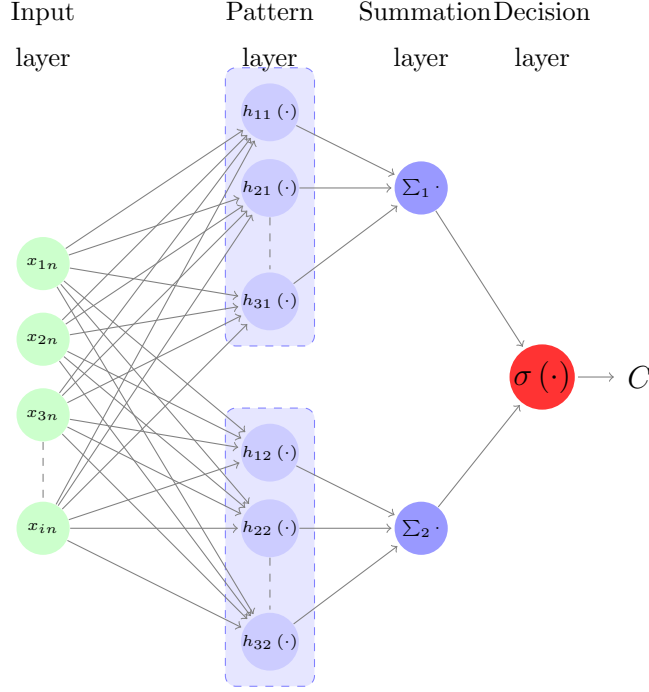


Figure 3.14: Representation of a neural network of the probabilistic neural network family.

label $y(\mathbf{x}_n)$.

Thus the best set of weights can be inferred in an optimization framework where the error $E(\cdot)$ has to be minimized. This optimization can be performed using a gradient descent method where the derivative of Eq. (3.68) can be computed using the backpropagation algorithm proposed by [204]. Matulewicz et al. [154] as well as Parfait et al. [180] used this classifier to classify MRSI spectra.

Probabilistic neural networks are another type of feed-forward networks which can be derived from the multilayer perceptron case and was proposed by [221]. This classifier can be modelled by changing the activation function $h(\cdot)$ in Eq. (3.67) to an exponential function such that:

$$h(\mathbf{x}_n) = \exp \left(-\frac{(\mathbf{w}_j - \mathbf{x})^T(\mathbf{w}_j - \mathbf{x})}{2\sigma^2} \right), \quad (3.69)$$

where σ is a free parameter set by the user.

The other difference of the probabilistic neural networks when compared with

3. REVIEW OF CADE AND CADX FOR CAP

the multilayer perceptron networks resides in the architecture as shown in Fig. 3.14. This network is formed by two hidden layers. The first hidden layer consists of the pattern layer, in which the mapping is done using Eq. (3.69). This pattern layer is sub-divided into a number of groups corresponding to the number of classes. The second hidden layer corresponds to the summation layer which simply sums the output of each sub-group of the pattern layer. This method was used in [9, 10, 261].

Graphical model classifiers: Markov random field (MRF) can also be used as a lesion segmentation method to detect CaP. First, we define s as a pixel which will belong to a certain class denoted by ω_s . The labelling process can be noted as $\omega = \{\omega_s, s \in I\}$ where I is the set of all the pixels inside the image. The observations corresponding to SI in the image are noted $\mathcal{F} = \{f_s | s \in I\}$. Thus, the image process \mathcal{F} represents the deviation from the labelling process ω [108]. Hence, lesion segmentation is equivalent to estimating the best $\hat{\omega}$ which maximizes the posterior probability $p(\omega|\mathcal{F})$. Thus, using a Bayesian approach, this can be formulated such that:

$$p(\omega|\mathcal{F}) = \arg \max_{\omega} \prod_{s \in I} p(f_s|\omega_s)p(\omega) . \quad (3.70)$$

It is generally assumed that $p(f_s|\omega_s)$ follows a Gaussian distribution and that the pixels classes $\lambda = \{1, 2\}$ for a binary classification will be characterized by their respective mean μ_λ and standard deviation σ_λ . Then, ω is a Markov random field, thus:

$$p(\omega) = \frac{1}{Z} \exp(-U(\omega)) , \quad (3.71)$$

where Z is a normalization factor to obtain a probability value, $U(\cdot)$ is the energy function.

Thus the segmentation problem can be solved as an optimization problem where the energy function $U(\cdot)$ has to be minimized. There are different possibilities to define the energy function $U(\cdot)$. However, it is common to define the energy function such that it combines two types of potential function: (i) a local term relative to the pixel itself and (ii) a smoothing prior which embeds neighbourhood information which will penalizes the energy function affecting the region

Table 3.10: Overview of the model validation techniques used in CAD systems.

Model validation techniques	References
LOOCV	[9, 10, 13, 14, 15, 37, 73, 110, 138, 141, 155, 166, 167, 175, 176, 184, 192, 239, 261, 263, 263, 265]
k -CV	[140, 180, 235, 236, 237, 238, 260, 262, 266]

homogeneity. This optimization of such a function can be performed using an algorithm such as iterated conditional modes [108]. Liu *et al.* [144] and Ozer *et al.* [176] used Markov random fields as an unsupervised method to segment lesions in multi-parametric MRI images. Artan *et al.* [14, 15] used conditional random fields instead of MRF for MRI segmentation. The difference between these two methods resides in the fact that conditional probabilities are defined such as:

$$p(\omega|\mathcal{F}) = \frac{1}{Z} \exp \left[- \sum_{s \in I} V_{C1}(\omega_s|\mathcal{F}) - \sum_{\{s,r\} \in C} V_{C2}(\omega_s, \omega_r|\mathcal{F}) \right]. \quad (3.72)$$

$V_{C1}(\cdot)$ is the state (or partition) feature function and $V_{C2}(\cdot)$ is the transition (or edge) feature function [109].

3.2.5 Model validation

In pattern recognition, the use of model validation techniques to assessing the performance of a classifier plays an important role in the final results. Two techniques are broadly used in the development of CAD system and are summarized in Table. 3.10. The most popular technique used in CAD systems (see Table. 3.10) is the leave-one-out cross-validation (LOOCV) technique. From the whole data, one patient is kept for validation and the other cases are used for training. This manipulation is repeated until each patient has been used for validation. This technique

3. REVIEW OF CADE AND CADX FOR CAP

Table 3.11: Overview of the evaluation metrics used in CAD systems.

Evaluation metrics	References
Accuracy	[14, 15, 144, 229, 238]
Sensitivity - Specificity	[14, 15, 73, 144, 145, 155, 175, 176, 180, 184, 234, 235, 258, 259]
ROC - AUC	[10, 13, 37, 73, 110, 117, 142, 145, 147, 154, 155, 166, 167, 184, 236, 237, 238, 239, 260, 261, 262, 263, 264, 265]
FROC	[140, 141, 266]
Dice's coefficient	[14, 15, 144, 175]

is popular when working with a limited number of patients, allowing to train on representative number of cases even with a small dataset. However LOOCV can suffer from large variance and can be considered as an unreliable estimate [60].

The other technique is the k -fold cross-validation (k -CV) technique which is based on splitting the dataset into k subsets where the samples are randomly selected. Then, one fold is kept for the validation and the remaining subsets are used for training. The classification is then repeated as in the LOOCV technique. In fact leave-one-out cross-validation (LOOCV) is a particular case of k -fold cross-validation (k -CV) when k equals the number of patients. In the reviewed papers, the typical values used for k were set to three and five. k -fold cross-validation (k -CV) is regarded as more appropriate than leave-one-out cross-validation (LOOCV), but the number of patients in the dataset needs to be large enough for the results to be meaningful.

3.2.6 Evaluation measure

Several metrics can be used in order to assess the performance of a classifier and are summarized in Tab. 3.11. Voxels in the MRI image are classified into healthy or malign tissue and compared with a ground-truth. This allows to compute a

confusion matrix by counting true positive, true negative, false positive and false negative samples. From this analysis, different statistics can be extracted.

The first statistic used is the accuracy which is computed as the ratio of true detection to the number of samples. However, depending on the strategy employed in the CAD work-flow, this statistic can be highly biased by a high number of true negative samples which will boost the accuracy score overestimating the actual performance of the classifier. That is why, the most common statistic computed are sensitivity and specificity which give a full overview of the performance of the classifier. Sensitivity is also called the true positive rate and is equal to the ratio of the true positive samples over the true positive added with the false negative samples as shown in Eq. (3.73). Specificity is also named the true negative rate and is equal to the ratio of the true negative samples over the true negative added with the false positive samples as shown in Eq. (3.74).

$$SEN = \frac{TP}{TP + FN} , \quad (3.73)$$

$$SPE = \frac{TN}{TN + FP} . \quad (3.74)$$

Check the definitions, there was a mistake here in the definitions previously

These statistics can be used to compute the receiver operating characteristic (ROC) curves [159]. This analysis represents graphically the sensitivity as a function of (1 - specificity), which is in fact the false positive rate, by varying the discriminative threshold of the classifier. By varying this threshold, more true negative samples will be found but often at the cost of detecting more false negatives. However, this fact is interesting in CAD since it is possible to obtain a high sensitivity and to ensure that no cancers are missed even if more false alarms have to be investigated. A statistic derived from ROC analysis is the area under the curve (AUC) which corresponds to the area under the ROC and is a measure used to make comparisons between models.

The ROC analysis can be classified as a pixel-based evaluation method. However, a cancer can be also considered as a region. The free-response receiver operating characteristic (FROC) extends the ROC analysis but to a region-based

level. The same confusion matrix can be computed were the sample are not pixels but lesions. However, it is important to define what is a true positive sample in that case. Usually, a lesion is considered as a true positive sample if the region detected by the classifier overlaps “sufficiently” the one delineated in the ground-truth. However, “Sufficiently” is a subjective measure defined by each researcher and can correspond to one pixel only. However, an overlap of 30 to 50 % is usually adopted. Finally, in addition to the overlap measure, the Dice’s coefficient is often computed to evaluate the accuracy of the lesion localization. This coefficient consists of the ratio between twice the number of pixels in common and the sum of the pixels of the lesions in the ground-truth GT and the output of the classifier S , defined as shown in Eq. (3.75).

$$Q_D = \frac{2|GT \cap S|}{|GT| + |S|} . \quad (3.75)$$

3.3 Discussion

3.3.1 Results reported

As discussed previously in Sect. 3.2.6, different metrics have been used to report results. A comparison of the different methods reviewed is given depending on the metric used in field of research and also the type of MRI scanner used (cf., 1.5 *versus* 3.0 Tesla). For each field, the *best performances* obtained in each study were reported in these figures. The results given in terms of AUC-ROC are depicted in Fig. ???. The results vary between 71% and 97% for some experiments with a 1.5 Tesla MRI scanner and 77% and 95% with a 3.0 Tesla MRI scanner.

The results in regard of sensitivity and specificity are reported in Fig. ???. In the case that the data were collected with a 1.5 Tesla MRI scanner, the sensitivity ranges from 74% to 100% and the specificity from 43% to 93%. For the experiments carried out with a 3.0 Tesla MRI scanner, the sensitivity varies from 60% to 90% and the specificity from 66% to 99%. Four studies also use FROC analysis to report their results and are reported in Fig. ???.

3.3.2 Comparison

We would like to stress the following findings drawn during the review of the different studies:

1. Quantitatively, it is difficult to make a fair comparison between the different studies reviewed. Different factors come into play to elucidate this fact. Mainly a lack of standardization can be pointed out in regard to experimental evaluation: (i) different datasets are used during the evaluation of the frameworks developed hindering a inter-study comparison. The same conclusion has been recently drawn by [138] supporting this argument; (ii) the experimental results are not reported with a common metric which leads to the inability to compare the different studies.
2. However, multiple studies reported some performance improvements using multi-parametric imaging techniques instead of mono-parametric imaging techniques. Considering only the most recent studies proposing CADe-CADx frameworks, the following results can be highlighted. Viswanath et al. [261] obtained an AUC of 77% using an ensemble learning approach combining the features from the three modalities T₂-W-DCE-DW MRI, while the results obtained as standalone modality were ranging from 62% to 65%. Tiwari et al. [239] drawn similar conclusions by using T₂-W and MRSI modalities as both in standalone and multi-parametric frameworks with an improved AUC ranging from 57%-76% to 85%. The most recent work of Litjens et al. [138] obtained an improved AUC metric from 71%-76% considering each modality separately (e.g., T₂-W-DCE-DW MRI) to 89% in their multi-parametric framework.
3. The studies comparing particular combination of more than one modality give rise to the same fact [138, 140, 142, 176]: using three modalities lead to better performances than using any combination of two modalities.
4. Unlike the previous remark 2, no straightforward conclusions can be given regarding the performances of each modality in a standalone framework. The modality being processed by different methods, it does not allow us to

3. REVIEW OF CADE AND CADx FOR CAP

conclude if a modality by itself is more suited than another. However, we were able to distinguish some interesting trends which deserves the attention of the community. Tiwari et al. in [236, 238, 239] observed that MRSI is a more suitable modality than T₂-W to highlight cancers. Moreover, ADC maps have shown a better discriminative power than T₂-W as well [117, 184, 261]. Lately, Litjens et al. in [138] observed that DW modality was more suitable than both DCE and T₂-W to distinguish CaP in their CADx system.

5. Furthermore, multi-parametric has attracted the attention of both radiologists and computer vision researchers. Indeed, pioneer research groups included new modalities over years when at the same time, new research groups directly introduced multi-parametric CAD systems. These facts lead us to think that CaP researches will benefit from multi-parametric imaging techniques.
6. When focusing on the different modalities used, it can be pointed out that no research reported the use of all modalities in a single framework: MRSI is usually used as a standalone modality and never combined with the three remaining. Nevertheless, this modality has shown some overall good performances at the price of a lower resolution as well as an increased acquisition time. Moreover, MRSI analysis is more complex in comparison with the other modalities. To our mind, MRSI could contribute in a multi-parametric framework and should be fused with the other modalities.
7. Lately, three studies focused on developing a region-based classification in which PZ and CG will be analysed separately [138, 141, 262]. The promising results were obtained which indicates that this strategy should be further investigated.
8. Recent studies are using quantitative features in addition to SI. It seems that these quantitative features provide uncorrelated information with respect to SI features and should lead to better performances when combined all together.

9. Regarding the methods used in the “image regularisation” (cf., pre-processing, segmentation and registration), it is particularly difficult to distinguish the benefit of a method over another since none of the studies focus on making comparison of these processing stages. The focus is usually entirely based on the “image classification” framework where different methods are directly compared. Note that the performance of a classifier is highly linked with the features vector extracted from particular data. Hence, one can not conclude that a machine learning method is more appropriate than another, but we can identify a trend in which SVM as well as ensemble learning classifiers (e.g., AdaBoost, GentleBoost and random forest) seem to perform better than neural network, LDA or Naive Bayes.
10. We would like to draw the attention of the reader on the feature extraction/selection stage. This processing could reduce the complexity and also find a better feature space for classification. However, few studies are performing such approaches. Niaf et al. [166, 167] are successfully applying a scheme to reduce the number of dimensions by selecting the most discriminative features. It allows them to obtain improved performances compared with a classification performed with their initial feature vector. Another group of studies also applied different feature extraction methods [233, 234, 235, 237, 238, 239, 258, 259, 262]. In these specific cases, no comparison is performed against the original data.

3.3.3 General discussion

CHECK THIS SECTION- this is where you want to mention all the points ? The last part about the dataset is commented

This review leads to some general discussions which could direct to future avenues for research. As previously mentioned, no open multi-parametric dataset is currently available. This fact leads to an impossibility to fairly compare the different algorithms designed over years. Also, the availability of a full multi-parametric MRI dataset, could lead to the development of algorithms which use all the different modalities currently available. Recalling Tab. 3.1, it can be noted that none of the current works provides a solution using at the same time the four

3. REVIEW OF CADE AND CADX FOR CAP

different modalities. Also, all the algorithms are focused on one type of scanner only, either 1.5 Tesla and 3.0 Tesla. A dataset including both these types of imaging could allow development of more generic algorithms.

Analysing the different stages of the CAD work-flow, it is seen that the current CAD systems do not include all the pre-processing steps. It could be interesting to evaluate the improvement using these pre-processing steps on the final results. Regarding segmentation and registration of the prostate, CAD systems could greatly benefit from specific research in these areas which could lead to a better automation of those systems. Moreover, other segmentation and registration methods not currently used in CAD systems could also obtain better results.

Regarding the classification framework, it seems that the current well-known pattern recognition methods have been widely studied. However, more investigations should be carried out regarding the feature detection stage. Lately, histogram-based features have shown good capabilities in the field of computer vision and could be further investigated. Only one study by [142] used some of these features.

An important point allowing a fair comparison between methods resides in the fact that no common dataset, nor universal evaluation model, nor metric has been defined by the research community allowing such comparison.

Chapter 4

Materials

4. MATERIALS

Chapter 5

Normalization/Standardization of T2W-MRI and DCE-MRI Images

CAD systems are usually designed as a sequential process consisting of four stages: pre-processing, segmentation, registration and classification. As a pre-processing image and data normalization is a crucial and important step of the chain in order to design a robust classifier and overcome the inter-patients intensity variations. However little attention has been dedicated to the normalization. In this section, we first propose two methods for normalization of T₂-W-MRI prostate images based on: (i) Rician *a priori* and (ii) Square-Root Slope Function (SRSF) representation. Then we proposed a fully automated framework for normalization of DCE-MRI images. In both cases, a comparison with the state-of-the-art methods are provided.

5.1 Normalization of T₂-W-MRI images

This section presents the state-of-the-art method proposed for normalization of T₂-W-MRI prostate images. Our proposed methods (Sect. 5.1.1), the designed experiments and finally the conclusions drawn from the results obtained.

Artan *et al.* [14, 15] and Ozer *et al.* [175, 176] proposed to normalize the T2W-MRI images by computing the standard score (i.e., *z-score*) of the PZ pixels such

5. NORMALIZATION/STANDARDIZATION OF T2W-MRI AND DCE-MRI IMAGES

as:

$$I_s(x) = \frac{I_r(x) - \mu_{PZ}}{\sigma_{PZ}}, \forall x \in PZ, \quad (5.1)$$

where, $I_s(x)$ and $I_r(x)$ are the standardized and the raw signal intensity, respectively, and μ_{PZ} and σ_{PZ} are the mean and standard deviation of the PZ signal intensity. This transformation enforces the image PDF to have a zero mean and a unit standard deviation. However, this normalization is not appropriate if the PDF do not follow a Gaussian distribution as illustrated in Fig. 5.1

Lv *et al.* [147] used the method proposed by Nyul *et al.* [171]. For a given patient, a warping function is inferred by matching some specific landmarks (i.e., median and different percentiles) of the current PDF to the same landmarks learned during a training phase from several patients. The mapping between each landmark is performed using a linear mapping. Viswanath *et al.* [262] used a variant of the previous method by segmenting first the image using region growing with a pre-defined homogeneity criterion and keeping only the largest region to build the PDF. Nevertheless, the warping functions inferred by these methods can suffer from abrupt changes around the landmarks position, leading to a disrupt PDF in the normalized image.

In this section, we evaluate and compare different normalization approaches in the context of T2W-MRI prostate images normalization. Our contribution is threefold: (i) a normalization approach based on a Rician *a priori*; (ii) a normalization approach based on a method used in registration of functional data, without any assumption regarding the PDF of the data; (iii) a novel evaluation metric to asses quantitatively the alignment of the PDFs independently of the assumed distribution. These methods will be compared qualitatively and quantitatively, with both *z-score* normalization and piecewise-linear normalization.

5.1.1 Methodology

5.1.1.1 Normalization using Rician *a priori*

As previosuly stated, proper normalization of the MRI data during pre-processing is a key problem that has been addressed using parametric and non-parametric strategies. We believe that normalizing MRI data using a parametric model based

5.1 Normalization of T₂-W-MRI images

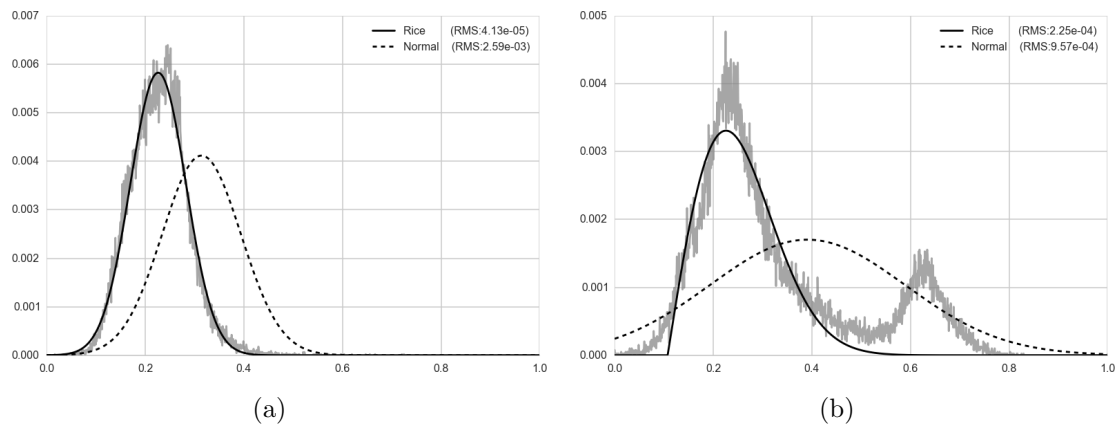


Figure 5.1: Visual evaluation of the goodness of fitting using Rician and Gaussian distribution.

on a Rician distribution would improve the results for the parametric case. Expecting this improvement by changing the data model from the widely used Gaussian distribution to Rician distribution is reasonable. Indeed, Bernstein *et al.* [21] state that MRI data theoretically follows a Rayleigh distribution for a low SNR scenarios while it appears closer to a Gaussian distribution when the SNR increases. Figure 5.1 shows the intensity spectrum for some MRI prostate data as well as the fitted Gaussian and Rician distributions. A qualitative assessment of the underlying distribution is performed by overlying the fitted distribution, while quantitative results of the fitting are given in terms of Root Mean Square (RMS). It can be highlighted that the Rician model better fits the data than the Gaussian model.

The normalization is carried out as: (i) fit a Rician model to each prostate PDF using non-linear least squares minimization; (ii) compute the mean (see Eq. (5.2)) and variance (see Eq. (5.3)) of the Rician model; (iii) normalize the entire data using the *z-score* similarly as in Eq. (5.1).

$$\mu_r = \sigma \sqrt{\frac{\pi}{2}} L_{1/2} \left(-\frac{\nu^2}{2\sigma^2} \right), \quad (5.2)$$

$$\sigma_r = 2\sigma^2 + \nu^2 - \frac{\pi\sigma^2}{2} L_{1/2}^2 \left(\frac{-\nu^2}{2\sigma^2} \right) , \quad (5.3)$$

where ν and σ are the distance between the reference point and the center of the bivariate distribution and the scale, respectively; $L_{1/2}$ denotes a Laguerre polynomial.

5.1.1.2 Normalization using generative models in functional data analysis

Srivastava *et al.* [222] have proposed a generic method to register functional data, without any assumption regarding the models of different functions. This framework (see Sect. ??) relies on the SRSF representation (see Sect. ??) which transforms the Fisher-Rao metric into the conventional \mathbb{L}^2 metric, and thus allows to define a cost function corresponding to an Euclidean distance between two functions in this new representation.

Square-Root Slope Function representation In the proposed registration framework of functional data, two function f_1 and f_2 are registered by composing f_2 with a warping function γ such that:

$$\arg \min_{\gamma \in \Gamma} D_{FR}(f_1, (f_2 \circ \gamma)) , \quad (5.4)$$

where D_{FR} is the Fisher-Rao distance and Γ is the set of all the functions γ .

The SRSF representation is used to transform the functions and register them into this space. The SRSF of a function f is defined as:

$$q(t) = \text{sign}(\dot{f}(t)) \sqrt{|\dot{f}(t)|} , \quad (5.5)$$

where $\dot{f}(t)$ corresponds to the derivative of f .

The major property of the SRSF representation used in the registration framework is the following: the composition of a function f with a warping function γ (i.e., $f \circ \gamma$) is equivalent to Eq. (5.6), using the SRSF representation.

$$\tilde{q}(t) = (q(t) \circ \gamma) \sqrt{\dot{\gamma}} , \quad (5.6)$$

where $\dot{\gamma}$ is the derivative of γ .

Using this property, a cost function (named amplitude or y -distance) is defined to measure the similarity between two functions f_1 and f_2 , expressed as in Eq. (5.7)

$$D_y(f_1, f_2) = \inf_{\gamma \in \Gamma} \|q_1 - (q_2 \circ \gamma)\sqrt{\dot{\gamma}}\| . \quad (5.7)$$

Registration framework The registration framework consists into two steps. First, an initialization in which the Karcher mean μ_f is computed as in Eq. (5.8)

$$\mu_f = \arg \min_{f \in \mathcal{F}} \sum_{i=1}^n D_y(f, f_i)^2 . \quad (5.8)$$

Then, for each function f_i : (i) compute γ_i^* as in Eq. (5.9); (ii) compute \tilde{q}_i as in Eq. (5.6); (iii) update μ_f as in Eq. (5.8) by replacing f_i by \tilde{f}_i , using \tilde{q}_i .

$$\gamma_i^* = \arg \min_{\gamma \in \Gamma} \sum_{i=1}^n D_y(\mu_f, f_i)^2 , \quad (5.9)$$

where n is the total number of functions to be aligned.

This step is iteratively performed based on the gradient of the cost function given in Eq. (5.8). We refer the reader to the work of Srivastava *et al.* [222] for more detailed discussion.

5.1.2 Experiments and results

5.1.2.1 Experiments

This section has repetitive information according to data, it should be checked.

The experiments are conducted on a subset of public multi-parametric MRI prostate publicly available dataset¹ [?]. This dataset was acquired from a cohort of patients with higher-than-normal level of PSA. The acquisition was performed using a 3T whole body MRI scanner (Siemens Magnetom Trio TIM, Erlangen, Germany) using sequences to obtain T₂-W-MRI. Aside of the MRI examinations, these patients also underwent a guided-biopsy. Finally, the dataset was composed of a total of 20 patients of which 18 patients had biopsy proven CaP and 2 patients

¹<http://visor.udg.edu/i2cvb/>

were “healthy” with negative biopsies. In this study, our subset consists of 17 patients with CaP. The prostate organ as well as the prostate zones (i.e., PZ, CG) and CaP were manually segmented by an experienced radiologist.

The different normalization methods are implemented in Python and publicly available in GitHub¹. The normalization based on SRSF uses the implementation² of Tucker *et al.* [246].

The model fitting for the Gaussian and Rician normalization is performed as a non-linear least squares problem, using Levenberg-Marquardt optimization. The piecewise-linear normalization is performed using the following set of percentiles $s \in \{0, 5, 25, 50, 75, 95, 100\}$ as landmarks. In the SRSF-based normalization, the PDFs are smoothed using spline-based denoising method.

5.1.2.2 Results

Qualitative Figure 5.2 depicts the alignment of the different PDFs using the different methods implemented. All the methods seem to address the problem of the PDF alignment of the full prostate data. However, the Rician normalization seems to outperform the other methods when focusing solely on the CaP data. The PDF computed in this specific area is more skewed from its original shape in the case of the piecewise-linear normalization than with the three other normalization strategies. The SRSF normalization gets unstable due to the warping function γ found which is in practise non-smooth.

Quantitative A spectral evaluation is performed by decomposing the set of normalized PDFs using PCA under the assumption that they are linearly dependent. Intuitively, the eigenvalues of the PCA decomposition are correlated with the alignment of the different PDFs. Thus, in the case of a perfect alignment of the PDFs, the first eigenvalue is much greater than the remaining since that the first eigenvector encodes all the information. In the contrary, in the case of a misalignment of the PDFs, more eigenvectors are needed to encode the information synonymous with larger eigenvalues. Thus, we propose to use the cumulative sum of the normalized eigenvalues as well as the AUC, as depicted in Fig. 5.3. Rician

¹<https://github.com/glemaitre/protoclass>

²<https://bitbucket.org/tetonedge/fdasrsf>

5.1 Normalization of T₂-W-MRI images

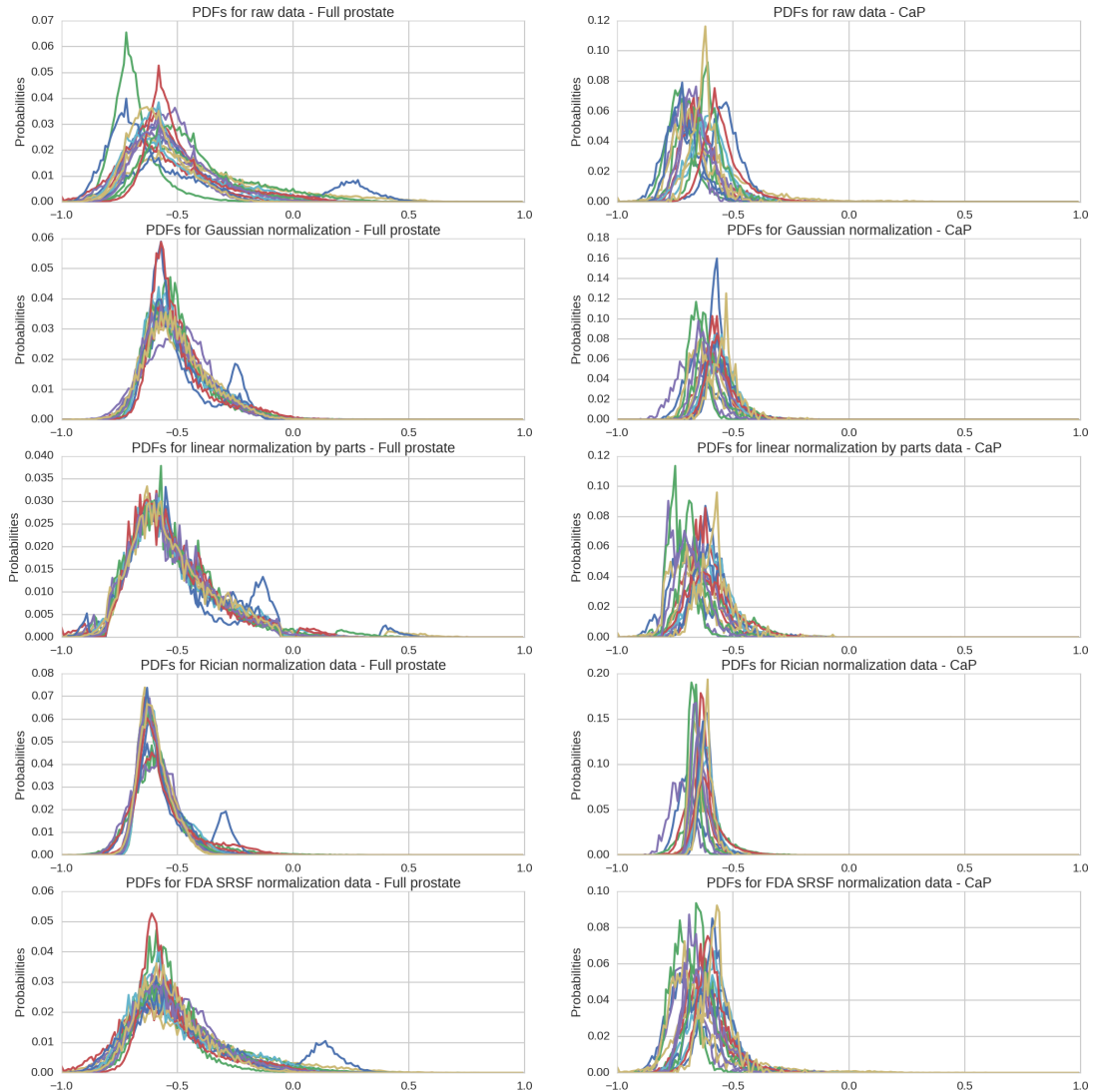
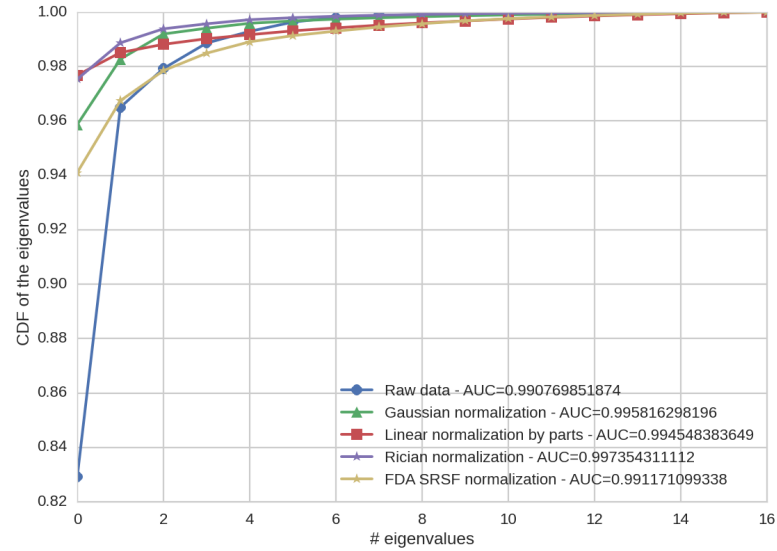
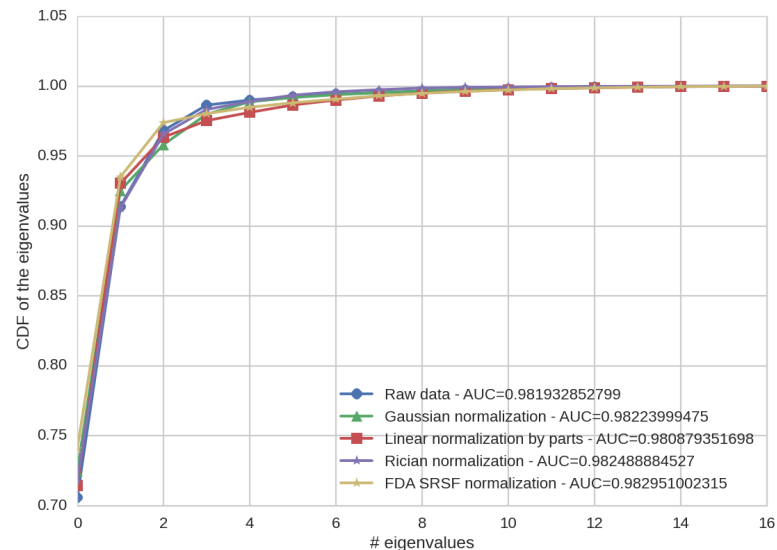


Figure 5.2: Qualitative evaluation by visual inspection of the alignment of the PDFs for the full prostate and the CaP.

5. NORMALIZATION/STANDARDIZATION OF T2W-MRI AND DCE-MRI IMAGES



(a)



(b)

Figure 5.3: Spectral evaluation using PCA decomposition: (a) evaluation considering the full prostate, (b) evaluation considering only the CaP.

normalization outperforms the other methods with an AUC of 0.9974 and 0.9824 considering the full prostate and CaP, respectively.

5.1.3 Discussion and conclusion

In this section, we propose to normalize the T₂-W-MRI prostate images using two new strategies: (i) based on a Rician *a priori* and (ii) based on a SRSF representation which do not make any assumption regarding the PDF of the data. An extensive comparison was conducted showing that the Rician normalization outperforms the Gaussian, SRSF-based, and piecewise-linear normalization for T₂-W-MRI prostate images normalization.

As avenues for future research, the contribution of the Rician normalization must be evaluated in a classification framework. Furthermore, normalized T₂-W-MRI can be included with other modalities in order to perform classification using multi-parametric MRI data.

5.2 Normalization of DCE-MRI images

In DCE-MRI, a contrast media is injected intravenously and a set of images is acquired over time. Consequently, each voxel in an image corresponds to a dynamic signal which is related to both contrast agent concentration and the vascular properties of the tissue. Therefore, changes of the enhanced signal allows to discriminate healthy from CaP tissues. In fact, these properties are automatically extracted using quantitative or semi-quantitative approaches [126].

Quantitative approaches uses pharmacokinetic modelling based on a bicompartiment model, namely Brix [29] and Tofts [242] models. The parameters of the Brix model are inferred assuming a linear relationship between the media concentration and the MRI signal intensity. This assumption has shown, however, to lead to inaccurately estimate the pharmacokinetic parameters [91]. In the contrary, Tofts model requires a conversion from MRI signal intensity to concentration, which becomes a non-linear relationship using specific equation of MRI sequences (e.g., FLASH sequence). Tofts modelling suffers, however, from a higher complexity [80]. Indeed, the conversion using the non-linear approach requires to acquire

5. NORMALIZATION/STANDARDIZATION OF T2W-MRI AND DCE-MRI IMAGES

a T_1 map which is not always possible during clinical examination. Additionally, the parameter calculation requires the AIF which is challenging to measure and can also lead to an inaccurate estimation.

Semi-quantitative approaches are rather mathematical than pharmacokinetic modelling since no pharmacokinetic assumption regarding the relation between the MRI signal and the contrast agent are made [80, 100]. These methods offer the advantages to not require any knowledge about the MRI sequence nor any conversion from signal intensity to concentration. However, they present some limitations: the heuristic approach proposed by Huisman *et al.* [100] requires an initial estimate of the noise standard deviation of the signal as well as some manual tuning.

Nevertheless, all presented methods suffer from two major drawbacks: (i) inter-patient variability and (ii) loss of information. The inter-patient variability is mainly due to the acquisition process and consequently leads to generalization issue while applying a machine learning algorithm. All previous methods extract few discriminative parameters to describe the DCE-MRI signal which might lead to a loss of information.

In this section, we propose a fully automatic normalization method for DCE-MRI that reduces the inter-patient variability of the data. The benefit and simplicity of our approach will be shown by classifying the whole normalized DCE-MRI signal and comparing with the state-of-the-art quantitative and semi-quantitative methods. Additionally, we will show that using this normalization approach in conjunction with the quantitative methods improves the classification performance of most of the models. We also propose a new clustering-based method to segment enhanced signals from the arteries, later used to estimate an AIF as well as an alternative approach to estimate the parameters of the semi-quantitative model proposed by [100].

This section is organized as follows: First Sect. 5.2.1.1 details our normalization strategy for DCE-MRI data. Quantitative and semi-quantitative methods are summarized in Sect. 5.2.1.2 with insights about their implementations. Finally experiments and results to answer the previous stated challenges are reported in Sect. 5.2.2 while discussed in Sect. 5.2.3, followed by a concluding section.

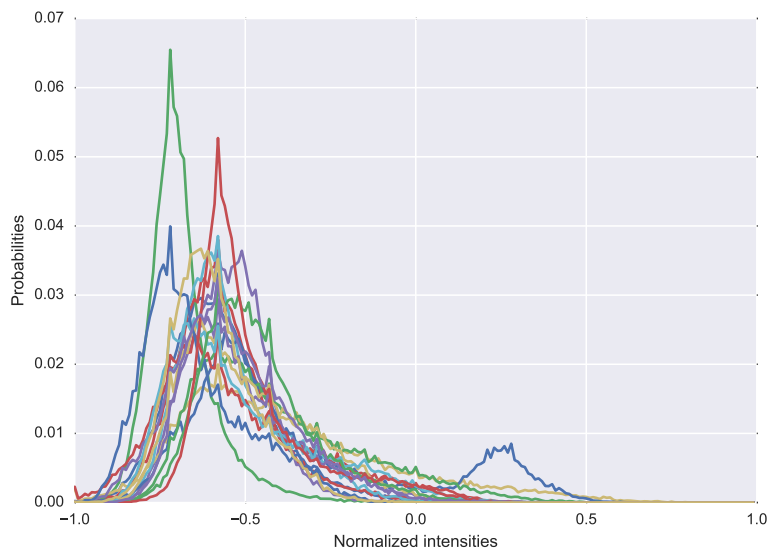


Figure 5.4: Illustration of the inter-patient variations in 17 different patients, using the PDF representation.

5.2.1 Methodology

5.2.1.1 Normalization of DCE-MRI images

In this section, we propose a method to normalize DCE-MRI prostate data to reduce inter-patient variations, although it can be applied to any DCE-MRI sequences. In T_2 -W-MRI, these variations are characterized by a shift and a scaling of the intensities as illustrated by the intensity PDF in Fig. 5.4. Therefore, these variations can be corrected using a z -score approach—i.e., normalizing the data by subtracting the mean and dividing by the standard deviation—assuming that the data follow a specific distribution [127].

In DCE-MRI, the intensity PDF of prostate gland does not follow a unique type of distribution such as Rician or Gaussian distribution, as shown in Fig. 5.5(a). Indeed, the inter-patient variations are more complex due to the temporal acquisition. A better representation to observe these variations is to represent the intensity PDF of the prostate gland over time—requiring to segment the prostate—using a heatmap representation as shown in Fig. 5.5(a). Analyzing this heatmap representation across patients (see Fig. 5.5(c)), the following variations are highlighted: (i) intensity offsets Δ_i of the PDF peak, (ii) a time offset Δ_t depending

5. NORMALIZATION/STANDARDIZATION OF T2W-MRI AND DCE-MRI IMAGES

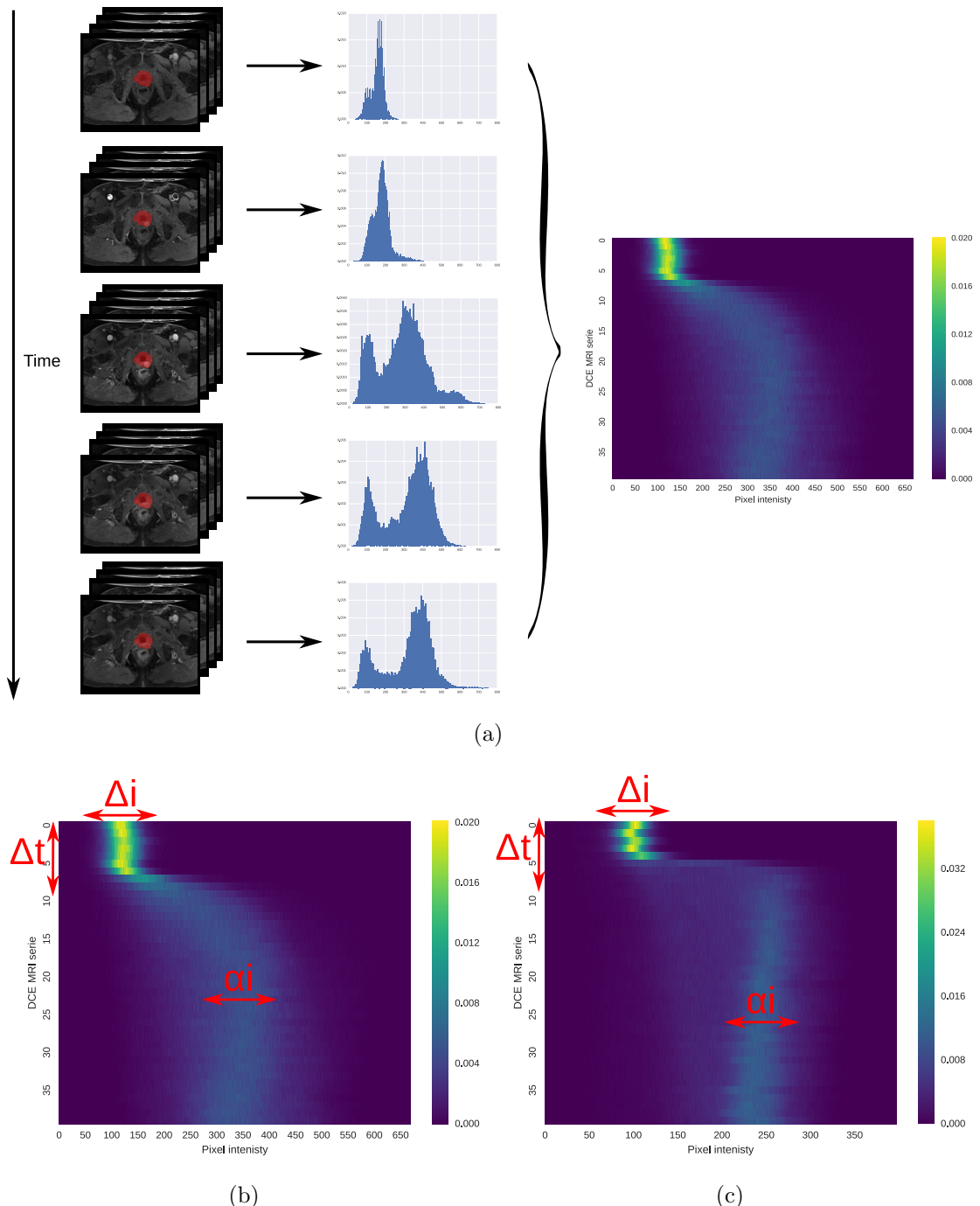


Figure 5.5: (a) Illustration of the heatmap representation: all PDFs of the prostate gland are concatenated together to build an heatmap; (b)-(c) Illustration of inter-patient variations (i.e., Δ_i , Δ_t , and α_i) PDF over time of two patients in a DCE-MRI.

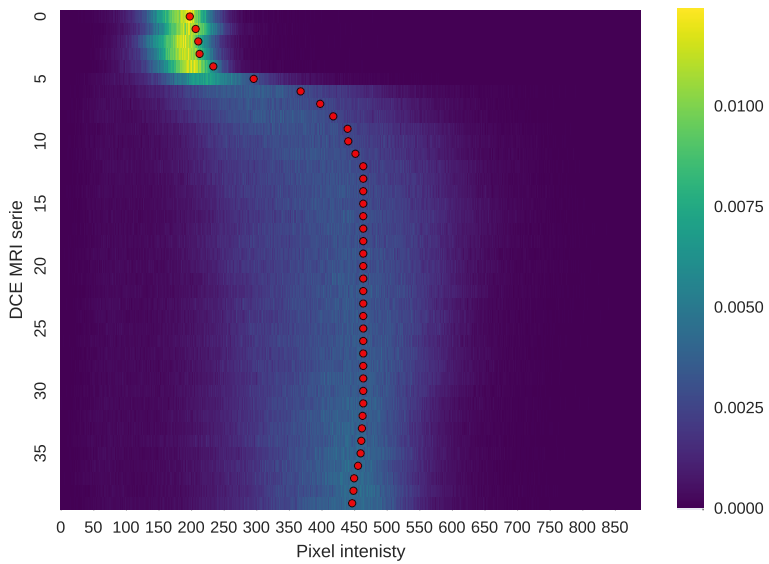


Figure 5.6: Illustration of the estimator found using the shortest-path through the graph.

of the contrast agent arrival, and (iii) a change of scale α_i related to the signal enhancement. Therefore, our normalization method should attenuate all these variations and be performed globally across the different time sequences rather than for each independent sequence.

Graph-based intensity offsets correction Before to standardize each sequence, the first step of the normalization is to cancel the intensity specific at each patient, occurring due to the media injection. As previously mentioned, the intensity PDF does not always follow either a Rician or a Gaussian distribution over time, in DCE-MRI. Therefore, the mean of these distributions cannot be used as a potential estimate for these offsets. Additionally, these offsets should be characterized by a smooth transition between series over time. Thus, this problem is solved using the graph-theory: considering the intensity PDF over time as shown in Fig. 5.5(a), the offsets correspond to the boundary splitting the heatmap in two partitions such that they are as close as possible to the peak of the intensity PDF (see Fig. 5.6 for an illustration). Given the heatmap, a directed weighted graph $\mathcal{G} = (\mathcal{V}, \mathcal{E})$ is built by taking each bar— i.e., the probability for a given time and

5. NORMALIZATION/STANDARDIZATION OF T2W-MRI AND DCE-MRI IMAGES

pixel intensity—of the heatmap as a node and connecting each pair of bars by an edge. The edge weight w_{ij} between two nodes i and j corresponding to two pixels at position (x_i, y_i) and (x_j, y_j) , respectively, is defined as in Eq. (5.10):

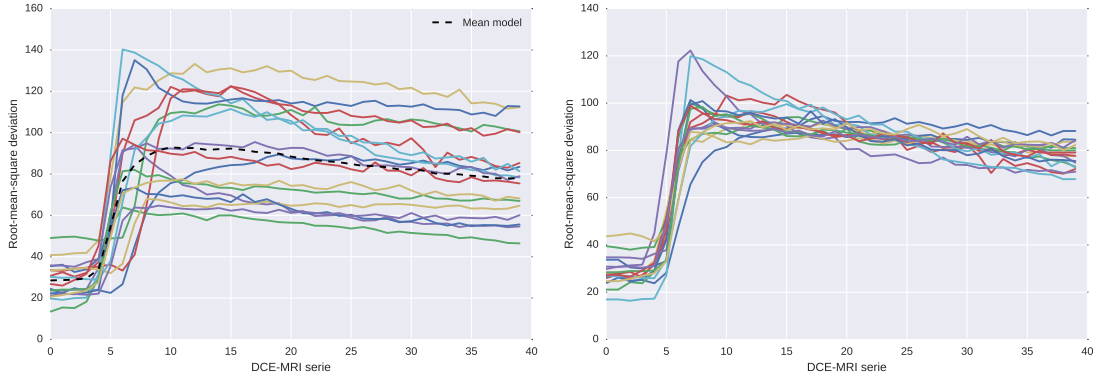
$$w_{ij} = \begin{cases} \alpha \exp\left(1 - \frac{H(i)}{\max(H)}\right) & \text{if } x_j = x_i + 1 \text{ and } y_j = y_i, \\ (1 - \alpha) \exp\left(1 - \frac{H(i)}{\max(H)}\right) & \text{if } x_j = x_i \text{ and } y_j = y_i + 1, \\ 0 & \text{otherwise,} \end{cases} \quad (5.10)$$

where H is the heatmap, α is a smoothing parameter controlling the partitioning.

Therefore, these offsets related to Δ_i are estimated by finding the shortest-path to cross the graph using Dijkstra's algorithm. The entry and exiting nodes are set to be the bin with the maximum probability for the first DCE-MRI serie and the bin corresponding to the median value for the last DCE-MRI serie, respectively. To ensure a robust estimation of these offsets, the process of finding the shortest-path is iteratively repeated by shifting the data and updating the heatmap as well as the graph \mathcal{G} . The procedure is stopped once the offset found does not change. In general, this process is not repeated more than 3 iterations. The parameter α is set to 0.9, empirically. Figure 5.6 illustrates the final estimation of the offsets Δ_i (i.e., red landmark) found for each DCE-MRI serie. Therefore, each intensity offset is subtracted for each DCE-MRI.

Time offset and data dispersion correction The next variations to correct are the time offset Δ_t and the data dispersion σ_i . By computing the Root-Mean-Square Deviation (RMSD) of the intensities for each DCE-MRI serie, one can observe these two variations as shown in Fig. 5.7(a). Therefore, to correct these variations, we propose to register each patient RMSD to a mean model which corresponds to the mean of all patients RMSD. The parametric model to perform the registration is formulated as in Eq. (5.11):

$$T(\alpha, \tau, f(t)) = \alpha f(t - \tau), \quad (5.11)$$



(a) RMSD computed for each patient of our dataset.
(b) RMSD after alignment using the curve parametric model.

Figure 5.7: Illustration of the correction of the time offset and the data dispersion.

where α and τ are the two parameters handling the time offset Δ_i and global scale σ_i , respectively, $f(\cdot)$ is the RMSD function define as:

$$f(t) = \sqrt{\left(\frac{\sum_{n=1}^N x(t)_n^2}{N} \right)}, \quad (5.12)$$

where $x(t)_n$ is the shifted intensity of a sample from a specific DCE-MRI serie at time t from a total number of N samples.

Therefore the registration problem is equivalent to:

$$\arg \min_{\alpha, \tau} = \sum_{t=1}^N [T(\alpha, \tau, f(t)) - \mu(t)]^2, \quad (5.13)$$

where $\mu(\cdot)$ is the mean model, N is the number of DCE-MRI serie.

Illustration of the correction applied to each RMSD patient is shown in Fig. 5.7(b). Once all these parameters have been inferred, the data are shifted as well as scaled.

The resulting normalized data can be used into two fashions: (i) each normalized signal can be used as a whole to determine whether the corresponding voxel is healthy or cancerous or (ii) the normalized data can be fitted using a quantitative method, as presented in the next section.

5. NORMALIZATION/STANDARDIZATION OF T2W-MRI AND DCE-MRI IMAGES

5.2.1.2 Quantification of DCE-MRI

The quantitative approaches for detection of DCE-based features was briefly discussed in Sect. 3.2.2.2. In this section, we present in details the different methods which have been used for the quantification of DCE-MRI for CaP detection [126] and which will be used for comparison in this work. Furthermore, we would like to emphasize the following additional contributions for this section: (i) a novel automatic AIF estimation algorithm based on clustering and (ii) a simplified semi-quantitative method using constrained optimization.

Brix and Hoffmann models In the Brix model [29], the MRI signal intensity is assumed to be proportional to the media concentration. Therefore, the model is expressed as in Eq. (5.14) (see also Eq. (3.29)):

$$s_n(t) = 1 + A \left[\frac{\exp(k_{el}t') - 1}{k_{ep}(k_{ep} - k_{el})} \exp(-k_{el}t) - \frac{\exp(k_{ep}t') - 1}{k_{el}(k_{ep} - k_{el})} \exp(-k_{ep}t) \right], \quad (5.14)$$

with

$$s_n(t) = \frac{s(t)}{S_0}, \quad (5.15)$$

where $s(t)$ and S_0 are the MRI signal intensity at time t and the average pre-contrast MRI signal intensity, respectively; A , k_{el} , and k_{ep} are the constant proportional to the transfer constant, the diffusion rate constant, and the rate constant, respectively. Additionally, t' is set such that $0 \leq t \leq \tau$, $t' = t$ and afterwards while $t > \tau$, $t' = \tau$.

Hoffmann *et al.* [94] proposed a similar model as expressed in Eq. (5.16), which derive from the Brix model:

$$s_n(t) = 1 + \frac{A}{\tau} \left[\frac{k_{ep}(\exp(k_{el}t') - 1)}{k_{el}(k_{ep} - k_{el})} \exp(-k_{el}t) - \frac{\exp(k_{ep}t') - 1}{(k_{ep} - k_{el})} \exp(-k_{ep}t) \right], \quad (5.16)$$

in which the constant A is redefined by isolating the parameter τ .

The parameters A , k_{el} , and k_{ep} are estimated by fitting the model using non-linear least-squares optimization solved with Levenberg-Marcquardt.

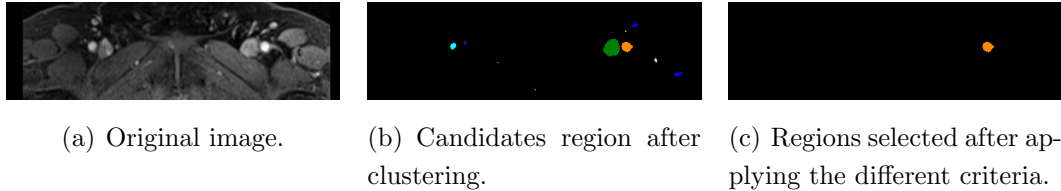


Figure 5.8: Illustration of the segmentation of the area used to determine the AIF.

Tofts model The extended Tofts model is formulated as in Eq. (5.17)(see also Eq. (3.30)):

$$C_t(t) = K_{trans} C_p(t) * \exp(-k_{ep}t) + v_p C_p(t), \quad (5.17)$$

where $*$ is the convolution operator; $C_t(t)$ and $C_p(t)$ are the concentrations of contrast agent in the tissue and in the plasma, respectively; K_{trans} , k_{ep} , and v_p are the volume transfer constant, the diffusion rate constant, and the plasma volume fraction, respectively.

Therefore, Tofts model requires to: (i) detect candidate voxels from the femoral or iliac arteries and estimate a patient-based AIF signal, (ii) convert the MRI signal intensity (i.e., AIF and dynamic signal) to a concentration, and (iii) in the case of a population-based AIF, estimate an AIF signal.

Segmentation of artery voxels and patient-based AIF estimation The AIF signal from DCE-MRI can be manually estimated by selecting the most-enhanced voxels from the femoral or iliac arteries [158]. Few methods have been proposed to address the automated extraction of AIF signal. [39] filtered successively the possible candidates to be considered as AIF such that [39]: (i) dynamic signals with small peak and voxels with a small wash-in are rejected by thresholding, (ii) a blob detector is used and large enough regions are kept, and (iii) circular and cylindricality criteria are used to reject the false positives. Zhu *et al.* [276] proposed an iterative method selecting voxels which best fit a gamma variate function [276]. However, it requires to compute first and second derivatives as well as maximum curvature points. Shanbhag *et al.* [212] proposed a 4-steps algorithm [63, 212]: (i) remove

5. NORMALIZATION/STANDARDIZATION OF T2W-MRI AND DCE-MRI IMAGES

slices with artefacts and find the best slices based on intrinsic anatomic landmarks and enhancement characteristics, (ii) find the voxel candidates using the maximum enhanced voxels and a multi-label maximum entropy based thresholding algorithm, (iii) exclude region next to the endorectal coil, and (iv) select the best 5 candidates which meet enhancement characteristics and that are correlated.

All the above methods are rather complex and thus we propose a simpler method which is based on the following reasonable assumptions: (i) all possible AIF signal candidates should have a similar shape, (ii) a high enhancement, and (iii) the arteries should be almost round and within a size range. Therefore, each slice is clustered into regions using K-means clustering with $k = 6$. The cluster made of the most enhanced signals is selected since it contains the artery signals. In this regards, the selection criteria corresponds to the 90th percentile of the maximum DCE-MRI signal. Finally, regions with an eccentricity smaller than 0.5 and an area in the range of [100, 400] voxels are kept. Additionally, to remove voxels contaminated by partial volume effect, only the 10% most enhanced voxels of the possible candidates are kept as proposed by [206] and the average signal is computed. A summary of the different segmentation steps is presented in Fig. 5.8.

Conversion of MRI signal intensity to concentration To estimate the free parameters of the Tofts model (see Eq. (5.17)), the concentration $C_t(t)$ and $C_p(t)$ need to be computed from the MRI signal intensity and the AIF signal, respectively. This conversion is based on the equation of the FLASH sequence—see ?? for details—and is formulated as in Eq. (5.18):

$$c(t) = \frac{1}{TR \cdot r_1} \ln \left(\frac{1 - \cos \alpha \cdot S^* \frac{s(t)}{S_0}}{1 - S^* \frac{s(t)}{S_0}} \right) - \frac{R_{10}}{r_1}, \quad (5.18)$$

with,

$$S^* = \frac{1 - \exp(-TR \cdot R_{10})}{1 - \cos \alpha \cdot \exp(-TR \cdot R_{10})}, \quad (5.19)$$

where $s(t)$ is the MRI signal, S_0 is the MRI signal prior to the injection of the contrast media, α is the flip angle, TR is the repetition time (TR),

R_{10} is the pre-contrast tissue relaxation time also equal to $\frac{1}{T_{10}}$, and r_1 is the relaxitativity coefficient of the contrast agent.

T_{10} can be estimated from the acquisition of a T_1 map. However, this modality is not part of the clinical trial in this research and the value of T_{10} is fixed to 1600 ms for both blood and prostate, in accordance with the values found in the literature [63? ?].

Estimation of population-based AIF While estimating the pharmacokinetic parameters from Tofts model, the AIF concentration $C_p(t)$ can be computed either from the patient or a population. We presented in the two previous sections the algorithms which allows to estimate the patient-based AIF concentration. To compare with the previous approach, we also computed a population-based AIF which will be also used later to compare the performance of both approaches. In that regard, the population-based AIF was estimated as in [158] by fitting the average patient-based AIFs to the model of [181] which is formulated as in Eq. (5.20):

$$C_p(t) = \sum_{n=1}^2 \frac{A_n}{\sigma_n \sqrt{2\pi}} \exp\left(\frac{-(t - T_n)^2}{2\sigma_n^2}\right) + \frac{\alpha \exp(-\beta t)}{1 + \exp -s(t - \tau)}, \quad (5.20)$$

where A_n , T_n , and σ_n are the scaling constants, centers, and widths of the n^{th} Gaussian, α and β are the amplitude and decay constant of the exponential; and s and τ are the width and center of the sigmoid function, respectively.

The parameters are estimated by fitting the model using a constrained non-linear least-squares optimization, solved with the Trust Region Reflective algorithm [220] and bounding the parameters to be positive.

PUN model Gliozzi *et al.* [80] showed that Phenomenological Universalities (PUN) approach can be used for DCE-MRI analysis [80]. The model has been successfully used in a CAD system proposed by [74]. This model can be expressed as in Eq. (5.21) (see also Eq. (3.31)):

$$s_n(t) = \exp \left[rt + \frac{1}{\beta} (a_0 - r) (\exp(\beta t) - 1) \right], \quad (5.21)$$

5. NORMALIZATION/STANDARDIZATION OF T2W-MRI AND DCE-MRI IMAGES

with

$$s_n(t) = \frac{s(t) - S_0}{S_0}, \quad (5.22)$$

where $s(t)$ and S_0 are the MRI signal intensity at time t and the average pre-contrast MRI signal intensity, respectively; r , a_0 , and β are the free parameters of the model.

The parameters are estimated by fitting the model using non-linear least-squares optimization solved with Levenberg-Marcquardt.

Semi-quantitative analysis The semi-quantitative analysis of the DCE-MRI is equivalent to extracting curve characteristics directly from the signal without a strict theoretical pharmacokinetic meaning (see Table. 3.7). In this work, we use the model presented by [100] which formulated the MRI signal as in Eq. (5.23):

$$s(t) = \begin{cases} S_0 & 0 \leq t \leq t_0 \\ S_M - (S_M - S_0) \exp\left(\frac{-(t-t_0)}{\tau}\right) & t_0 < t \leq t_0 + 2\tau \\ S_M - (S_M - S_0) \exp\left(\frac{-(t-t_0)}{\tau}\right) + w(t - t_0 + 2\tau) & t > t_0 + 2\tau \end{cases} \quad (5.23)$$

where $s(t)$ is the MRI signal intensity, S_0 is the pre-contrast signal intensity, t_0 is the time corresponding to the start of enhancement, S_M and τ is the maximum of the signal and the exponential time constant, and w is the slope of the linear part.

Huisman *et al.* [100] argue that curve fitting via least-squares minimization using Nelder-Mead algorithm leads to inaccurate estimation of the free parameters: mainly the issue come from an incorrect estimation of the start of enhancement t_0 leading to incorrect estimation of the other parameters. Therefore, they propose to: (i) estimate robustly t_0 , (ii) estimate S_0 by averaging the samples between 0 and t_0 (ii) estimate w depending if the slope is significant or not, (iii) estimate S_M which should be the point at the intersection of the most probable slope line and the plateau.

Instead of these successive estimations, we propose a unified optimization in which t_0 is fixed since that this is a key parameter. Therefore, t_0 is robustly estimated from the AIF signal since that this is the most enhanced signal in which

the start of enhancement is easily identifiable. The AIF signal is computed as in Section ???. t_0 is estimated by finding the maximum of the first derivative of the AIF signal, always occurring at the beginning of the signal. Then, the function in Eq. (5.23) is fitted using non-linear least squares with the Trust Region Reflective algorithm [220]. Furthermore, the parameters τ and S_M are bounded during the optimization to ensure robust estimations. τ is bounded between t_0 and t_f which is the time of the last sample while S_M is bounded between S_0 and $\max(s(t))$.

From Eq. (5.23), the following features are extracted: (i) the wash-in corresponding to the slope between t_0 and $t_0 + 2\tau$, (ii) the wash-out corresponding to the parameter w , (iii) the area under the curve between t_0 and the end of the signal, (iv) the exponential time constant τ , and (v) the relative enhancement $S_M - S_0$.

5.2.2 Experiment and results

Data, check with the material chapter

The multi-parametric MRI data are acquired from a cohort of patients with higher-than-normal level of PSA. The acquisition is performed using a 3T whole body MRI scanner (Siemens Magnetom Trio TIM, Erlangen, Germany) using sequences to obtain T₂-W-MRI, DCE-MRI and DW-MRI. Aside of the MRI examination, these patients also have undergone a guided-biopsy. The dataset is composed of a total of 20 patients of which 18 patients have biopsy proven CaP and 2 patients are “healthy” with negative biopsies. Therefore, 13 patients have a CaP in the PZ, 3 patients have CaP in the CG, 2 patients have invasive CaP in both PZ and CG and finally 2 patients are considered as “healthy”. An experienced radiologist has segmented the prostate organ — on T₂-W-MRI and DCE-MRI — as well as the prostate zones (i.e., PZ and CG) and CaP on the T₂-W-MRI.

A 3 mm slice fat-suppressed T₂-W fast spin-echo sequence (TR/TE/Echo Train Length (ETL): 3400 ms/85 ms/13) is used to acquire images in sagittal and oblique coronal planes, the latter planes being orientated perpendicular or parallel to the prostate PZ rectal wall axis. Three-dimensional T₂-W fast spin-echo (TR/TE/ETL: 3600 ms/143 ms/109, slice thickness: 1.25 mm) images are then acquired in an

5. NORMALIZATION/STANDARDIZATION OF T2W-MRI AND DCE-MRI IMAGES

Table 5.1: Coefficient of determination R^2 (i.e., μ ($\pm\sigma$)), while fitting data with the different quantification models.

Data type	Brix	Hoffmann	Tofts population AIF	Tofts patient AIF	PUN	Semi-quantitative
Un-normalized	0.85 (± 0.11)	0.81 (± 0.17)	0.84 (± 0.14)	0.88 (± 0.12)	0.27 (± 0.18)	0.64 (± 0.24)
Normalized	0.92 (± 0.05)	0.72 (± 0.32)	0.92 (± 0.06)	0.90 (± 0.10)	0.28 (± 0.20)	0.75 (± 0.20)

oblique axial plane. The nominal matrix and FOV of the 3D T₂-W fast spin-echo images are 320 × 256 and 280 × 240 mm², respectively, thereby affording sub-millimetric pixel resolution within the imaging plane.

DCE-MRI is performed using a fat suppressed 3D T₁ VIBE sequence (TR/TE/Flip angle: 3.25 ms/1.12 ms/10°; Matrix: 256 × 192; FOV: 280 × 210 (with 75% rectangular FOV); slab of 16 partitions of 3.5 mm thickness; temporal resolution: 6 s/slab over approximately 5 min). A power injector (Medrad, Indianola, USA) is used to provide a bolus injection of Gd-DTPA (Dotarem, Guerbet, Roissy, France) at a dose of 0.2 ml Gd-DTPA/kg of body weight.

These DCE-MRI sequences are resampled using the spatial information of the T₂-W-MRI and missing data are interpolated using a linear interpolation. The volumes of the DCE-MRI dynamic are rigidly registered, to remove any patient motion during the acquisition. Furthermore, a non-rigid registration is performed between the T₂-W-MRI and DCE-MRI in order to propagate the prostate zones and CaP ground-truths. The resampling is implemented in C++ using the Insight Segmentation and Registration Toolkit [102].

The implementation of the registration (C++), normalization (Python), and classification pipeline (Python) are publicly available on GitHub¹ [125]. The data used for this work are also publicly available² [128].

5.2.2.1 Goodness of model fitting

Parameter estimation of the quantification methods are related to fit a specific model to the DCE-MRI data. Therefore, this section report the goodness of fitting

¹<https://github.com/I2Cvb/lemaître-2016-nov/tree/master>

²<https://zenodo.org/record/61163>

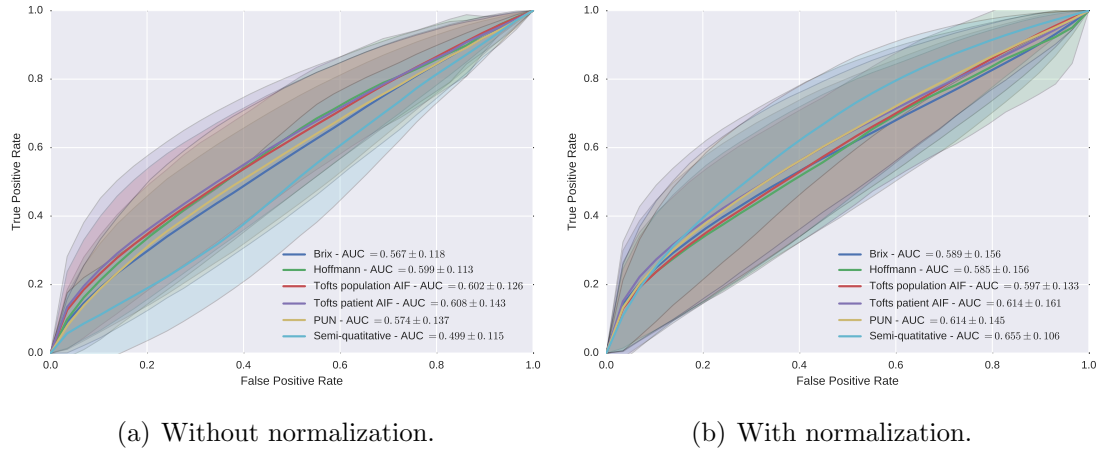


Figure 5.9: ROC analysis using a RF classifier with and without normalization DCE-MRI data for different pharmacokinetic models.

by computing the coefficient of determination R^2 such as in Eq. (5.24)

$$R^2 = 1 - \frac{\sum_{t=1}^T (s_t - \hat{s}_t)^2}{\sum_{t=1}^T (s_t - \bar{s})^2}, \quad (5.24)$$

where s_t and \hat{s}_t are the signal to be fitted and the estimated signal at time t , respectively; \bar{s} is the average signal to be fitted.

Mean and standard-deviation of the coefficient of determination R^2 is reported in Table 5.1 for each quantification model. Brix, Hoffmann, and Tofts models are fitted with a coefficient R^2 superior to 0.80. Additionally, the proposed PUN model does not seem to fit well the data. Data normalization improves the coefficient R^2 for all the methods apart of the Hoffmann model. The large standard deviation for this model might imply that there are some cases where the fitting fails.

5.2.2.2 Detection of CaP using pharmacokinetic parameters

To study the potential benefit of our normalization, CaP are detected at a voxel level using pharmacokinetic parameters estimated from un-normalized and normalized DCE-MRI data. Each individual pharmacokinetic parameter is classified to evaluate their individual discriminative power to detect CaP. Therefore, a Random

5. NORMALIZATION/STANDARDIZATION OF T2W-MRI AND DCE-MRI IMAGES

Table 5.2: AUC (i.e., $\mu (\pm\sigma)$) for each individual pharmacokinetic parameter using a RF classifier.

Features	Un-normalized data	Normalized data
Brix model		
A	0.540 (± 0.069)	0.555 (± 0.080)
k_{el}	0.549 (± 0.062)	0.577 (± 0.093)
k_{ep}	0.506 (± 0.032)	0.497 (± 0.019)
Hoffmann model		
A	0.516 (± 0.020)	0.508 (± 0.031)
k_{el}	0.545 (± 0.066)	0.529 (± 0.065)
k_{ep}	0.550 (± 0.063)	0.545 (± 0.060)
Tofts model with population AIF		
K_{trans}	0.556 (± 0.086)	0.565 (± 0.097)
k_{ep}	0.506 (± 0.026)	0.528 (± 0.038)
v_p	0.533 (± 0.064)	0.548 (± 0.082)
Tofts model with patient AIF		
K_{trans}	0.563 (± 0.077)	0.548 (± 0.060)
k_{ep}	0.492 (± 0.025)	0.491 (± 0.020)
v_p	0.530 (± 0.069)	0.495 (± 0.033)
PUN model		
a_0	0.521 (± 0.040)	0.530 (± 0.045)
r	0.550 (± 0.085)	0.573 (± 0.097)
β	0.531 (± 0.051)	0.549 (± 0.068)
Semi-quantitative analysis		
wash-in	0.587 (± 0.107)	0.533 (± 0.032)
wash-out	0.516 (± 0.037)	0.486 (± 0.035)
IAUC	0.506 (± 0.048)	0.513 (± 0.032)
τ	0.565 (± 0.104)	0.537 (± 0.089)
$S_M - S_0$	0.560 (± 0.083)	0.532 (± 0.029)

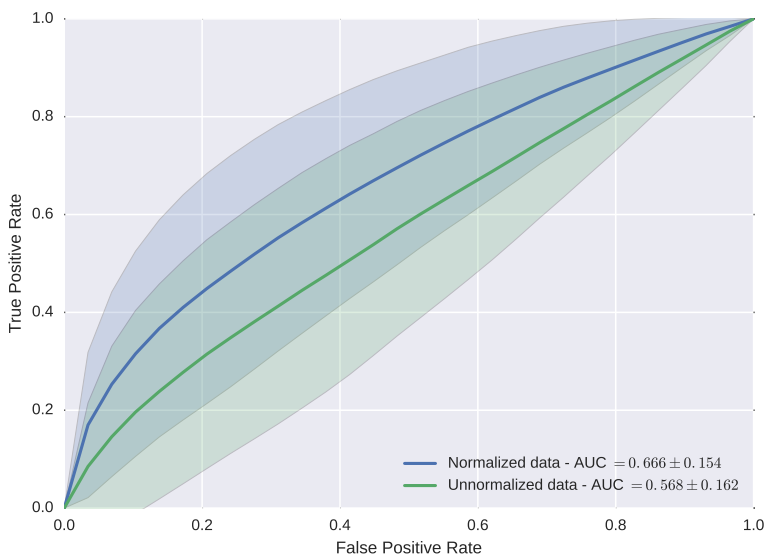


Figure 5.10: ROC analysis using the entire DCE-MRI signal with and without normalization in conjunction with a RF classifier.

Forest (RF) classifier is used in conjunction with a Leave-One-Patient-Out Cross-Validation (LOPO CV). The use of RF is motivated since that it leads to the best performance in the state-of-the-art methods [126, 138]. Results are summarized in Table 5.2 in terms of AUC. Normalization can improve the detection of CaP; however, the benefit of normalization is more obvious by combining together the pharmacokinetic features of a given model (e.g., A , k_{ep} , and k_{el} for Brix model), as previously done in traditional CAD system [126]. For the latter configuration, results are summarized by performing a ROC analysis and computing the AUC, as reported in Fig. 5.9. Quantification using normalized data outperforms quantification using un-normalized data in terms of classification performance apart of Hoffmann and Tofts population-based AIF models. The reasons behind the decrease of the AUC might be related to: (i) a poor fitting as discussed in Sect. ?? (cf., Hoffmann model) and (ii) a small number of patients while estimating some parameters (cf., Tofts model). The best classification performance are obtained using the semi-quantitative approach with an AUC of 0.655.

5.2.2.3 Classification of the entire enhanced DCE-MRI signal

As stated in the introduction, the quantification methods are extracting a set of parameters characterizing the enhancement DCE-MRI signal. However, this extraction might lead to a loss of information. This experiment is performed to assess if making use of the whole DCE-MRI signal instead of the just the pharmacokinetic parameters can improve the classification performance. Therefore, each enhanced DCE-MRI signal, normalized and un-normalized, is classified using a RF classifier in a LOPO CV fashion. The ROC analysis and AUC are reported in Fig. 5.10. Classification without normalization lead to the worst performance, with an AUC of 0.568. However, data normalization in conjunction with the use of the whole DCE-MRI signal is the strategy which outperforms all others, with an AUC of 0.666.

5.2.3 Discussion and conclusion

The experiments conducted in the previous section can give rise to several discussions. In Tofts quantification, two different approaches have been used to infer the pharmacokinetic parameters: using a population-based or a patient-based AIF. The patient-based AIF approach leads to better classification performance. However, there are two shortcomings to take into account while advancing this fact: (i) T_{10} parameter has been fixed and not computed from a T_1 map and (ii) the population-based AIF has been estimated from a cohort of only 17 patients. These two limitations have to be considered while advancing that population-based AIF modelling is outperforming patient-based AIF modelling.

The best classification performance is reached by normalizing the DCE-MRI data and use the whole enhanced signal as feature, emphasizing the fact that a loss of information while extracting quantitative parameters. Furthermore, this normalization is a less complex process than all quantification methods. However, this strategy suffers from one drawback: the training time of the RF classifier increases since that from 3 to 5 features, the feature space becomes a 40 dimensions space.

Nevertheless, this study is performed on a small cohort of patients using a single MRI machine. Generalizing the results of this study on a larger dataset

5.2 Normalization of DCE-MRI images

acquired from different commercial systems have to be considered to study the robustness of the proposed approach.

In this work, we presented a new method for normalizing/standardizing DCE-MRI data. This method aimed at reducing the inter-patient variations occurring during data acquisition. A graph-based approach was used to correct intensity offset in conjunction with a model-based correction to reduce time offset as well as intensity scaling. We show the benefit of our normalization method prior to extract quantitative and semi-quantitative features, with a significant improvement of the classification performance. Nevertheless, we also show that using the whole normalized DCE-MRI signal outperforms all quantitative approaches.

As avenues for future research, this normalization has to be part of a multi-parametric MRI (mp-MRI) CAD system in which DCE-MRI modality needs to be combined with other complementary modalities.

5. NORMALIZATION/STANDARDIZATION OF T2W-MRI AND DCE-MRI IMAGES

References

- [1] I. Agalliu, R. Gern, S. Lanza, and R. D. Burk. Associations of high-grade prostate cancer with BRCA1 and BRCA2 founder mutations. *Clin. Cancer Res.*, 15(3):1112–1120, Feb 2009. 3
- [2] N. Ahmed, T. Natarajan, and K. Rao. Discrete cosine transform. *Computers, IEEE Transactions on*, C-23(1):90–93, 1974. ISSN 0018-9340. 54
- [3] M. A. Aizerman, E. A. Braverman, and L. Rozonoer. Theoretical foundations of the potential function method in pattern recognition learning. In *Automation and Remote Control*, number 25, pages 821–837, 1964. 65
- [4] O. Akin, E. Sala, C. S. Moskowitz, K. Kuroiwa, N. M. Ishill, D. Pucar, P. T. Scardino, and H. Hricak. Transition zone prostate cancers: features, detection, localization, and staging at endorectal MR imaging. *Radiology*, 239(3):784–792, Jun 2006. 10, 11
- [5] D. D. Alexander, P. J. Mink, C. A. Cushing, and B. Sceurman. A review and meta-analysis of prospective studies of red and processed meat intake and prostate cancer. *Nutr J*, 9:50, 2010. 3
- [6] M. Amadasun and R. King. Textural features corresponding to textural properties. *Systems, Man and Cybernetics, IEEE Transactions on*, 19(5):1264–1274, 1989. ISSN 0018-9472. 42
- [7] A. C. American Cancer Society. Cancer Facts and Figures 2010. <http://www.cancer.org/research/cancerfactsfigures>, 2010. URL <http://www.cancer.org/research/cancerfactsfigures>. Accessed: 2013-08-01.

REFERENCES

- [8] A. C. American Cancer Society. Cancer Facts and Figures 2013. <http://www.cancer.org/research/cancerfactsfigures>, 2013. Accessed: 2013-08-01. 3
- [9] D. Ampeliotis, A. Anonakoudi, K. Berberidis, and E. Z. Psarakis. Computer aided detection of prostate cancer using fused information from dynamic contrast enhanced and morphological magnetic resonance images. In *IEEE International Conference on Signal Processing and Communications*, pages 888–891, 2007. 26, 28, 40, 48, 49, 52, 56, 57, 68, 80, 81
- [10] D. Ampeliotis, A. Anonakoudi, K. Berberidis, E. Z. Psarakis, and A. Kounoudes. A computer-aided system for the detection of prostate cancer based on magnetic resonance image analysis. In *International Symposium on Communications, Control and Signal Processing*, 2008. 26, 28, 40, 48, 49, 52, 56, 57, 68, 80, 81, 82
- [11] L. T. Amundadottir, P. Sulem, J. Gudmundsson, A. Helgason, A. Baker, B. A. Agnarsson, A. Sigurdsson, K. R. Benediktsdottir, J. B. Cazier, J. Sainz, M. Jakobsdottir, J. Kostic, D. N. Magnusdottir, S. Ghosh, K. Agnarsson, B. Birgisdottir, L. Le Roux, A. Olafsdottir, T. Blöndal, M. Andressdottir, O. S. Gretarsdottir, J. T. Bergthorsson, D. Gudbjartsson, A. Gylfason, G. Thorleifsson, A. Manolescu, K. Kristjansson, G. Geirsson, H. Isaksson, J. Douglas, J. E. Johansson, K. Balter, F. Wiklund, J. E. Montie, X. Yu, B. K. Suarez, C. Ober, K. A. Cooney, H. Gronberg, W. J. Catalona, G. V. Einarsson, R. B. Barkardottir, J. R. Gulcher, A. Kong, U. Thorsteinsdottir, and K. Stefansson. A common variant associated with prostate cancer in European and African populations. *Nat. Genet.*, 38(6):652–658, Jun 2006. 3
- [12] G. L. Andriole, E. D. Crawford, R. L. Grubb, S. S. Buys, D. Chia, T. R. Church, M. N. Fouad, E. P. Gelmann, P. A. Kvale, D. J. Reding, J. L. Weissfeld, L. A. Yokochi, B. O'Brien, J. D. Clapp, J. M. Rathmell, T. L. Riley, R. B. Hayes, B. S. Kramer, G. Izmirlian, A. B. Miller, P. F. Pinsky, P. C. Prorok, J. K. Gohagan, and C. D. Berg. Mortality results from a randomized Prostate-cancer screening trial. *New England Journal of Medicine*, 360(13):1310–1319, 2009. 4

- [13] T. Antic, Y. Peng, Y. Jiang, M. L. Giger, S. Eggener, and A. Oto. A study of T2-weighted MR image texture features and diffusion-weighted MR image features for computer-aided diagnosis of prostate cancer. In *Proc. SPIE 8670, Medical Imaging 2013: Computer-Aided Diagnosis*, pages 86701H–86701H–6, 2013. 26, 53, 54, 56, 68, 70, 81, 82
- [14] Y. Artan, D. Langer, M. Haider, T. H. Van der Kwast, A. Evans, M. Wernick, and I. Yetik. Prostate cancer segmentation with multispectral MRI using cost-sensitive Conditional Random Fields. In *Biomedical Imaging: From Nano to Macro, 2009. ISBI '09. IEEE International Symposium on*, pages 278–281, 2009. 26, 32, 39, 40, 41, 50, 52, 59, 68, 77, 81, 82, 91
- [15] Y. Artan, M. A. Haider, D. L. Langer, T. H. van der Kwast, A. J. Evans, Y. Yang, M. N. Wernick, J. Trachtenberg, and I. S. Yetik. Prostate cancer localization with multispectral MRI using cost-sensitive support vector machines and conditional random fields. *IEEE Trans Image Process*, 19(9):2444–2455, Sep 2010. 26, 32, 39, 40, 41, 50, 52, 59, 68, 77, 81, 82, 91
- [16] H. M. Awwad, J. Geisel, and R. Obeid. The role of choline in prostate cancer. *Clin. Biochem.*, 45(18):1548–1553, Dec 2012. 10, 20
- [17] J. O. Barentsz, J. Richenberg, R. Clements, P. Choyke, S. Verma, G. Villeirs, O. Rouviere, V. Logager, and J. J. Futterer. ESUR prostate MR guidelines 2012. *Eur Radiol*, 22(4):746–757, Apr 2012. 4, 10, 11, 18, 19, 22
- [18] M. Belkin and P. Niyogi. Laplacian eigenmaps and spectral techniques for embedding and clustering. In *Advances in Neural Information Processing Systems 14*, pages 585–591. MIT Press, 2001. 43, 65
- [19] S. Belongie, J. Malik, and J. Puzicha. Shape matching and object recognition using shape contexts. *Pattern Analysis and Machine Intelligence, IEEE Transactions on*, 24(4):509–522, 2002. ISSN 0162-8828. 56
- [20] A. Benassi, S. Cohen, and J. Istas. Identifying the multifractional function of a Gaussian process. *Statistics & Probability Letters*, 39(4):337 – 345, 1998. ISSN 0167-7152. 54

REFERENCES

- [21] M. A. Bernstein, D. M. Thomasson, and W. H. Perman. Improved detectability in low signal-to-noise ratio magnetic resonance images by means of a phase-corrected real reconstruction. *Medical Physics*, 16(5):813–817, 1989. 93
- [22] C. M. Bishop. *Pattern recognition and machine learning*. Springer-Verlag New York, Inc., Secaucus, NJ, USA, 2006. ISBN 0387310738. 67, 75, 77
- [23] F. L. Bookstein. Principal warps: thin-plate splines and the decomposition of deformations. *Pattern Analysis and Machine Intelligence, IEEE Transactions on*, 11(6):567–585, 1989. ISSN 0162-8828. 42
- [24] B. E. Boser, I. M. Guyon, and V. N. Vapnik. A training algorithm for optimal margin classifiers. In *Proceedings of the Fifth Annual Workshop on Computational Learning Theory*, COLT '92, pages 144–152, New York, NY, USA, 1992. ACM. ISBN 0-89791-497-X. 77
- [25] A. Bourdoumis, A. G. Papatsoris, M. Chrisofos, E. Efstathiou, A. Skolarikos, and C. Deliveliotis. The novel prostate cancer antigen 3 (PCA3) biomarker. *Int Braz J Urol*, 36(6):665–668, 2010. 5
- [26] L. Breiman. Random forests. *Machine Learning*, 45(1):5–32, 2001. 73
- [27] L. Breiman, J. Friedman, R. Olshen, and C. Stone. *Classification and regression trees*. Wadsworth and Brooks, Monterey, CA, 1984. 72, 73
- [28] J. Brenner, A. Chinnaiyan, and S. Tomlins. ETS fusion genes in prostate cancer. In D. J. Tindall, editor, *Prostate Cancer*, volume 16 of *Protein Reviews*, pages 139–183. Springer New York, 2013. ISBN 978-1-4614-6827-1. 5
- [29] G. Brix, W. Semmler, R. Port, L. R. Schad, G. Layer, and W. J. Lorenz. Pharmacokinetic parameters in cns gd-dtpa enhanced mr imaging. *Journal of computer assisted tomography*, 15(4):621–628, 1991. 99, 106
- [30] A. Buades, B. Coll, and J. Morel. A review of image denoising algorithms, with a new one. *Simul*, 4:490–530, 2005. 27

- [31] D. L. Buckley, C. Roberts, G. J. Parker, J. P. Logue, and C. E. Hutchinson. Prostate cancer: evaluation of vascular characteristics with dynamic contrast-enhanced T1-weighted MR imaging—initial experience. *Radiology*, 233(3):709–715, Dec 2004. 14
- [32] R. H. Byrd, P. Lu, J. Nocedal, and C. Zhu. A limited memory algorithm for bound constrained optimization. *SIAM J. Sci. Comput.*, 16(5):1190–1208, Sept. 1995. ISSN 1064-8275. 48, 70
- [33] P. Carmeliet and R. K. Jain. Angiogenesis in cancer and other diseases. *Nature*, 407(6801):249–257, Sep 2000. 14
- [34] C. L. Carroll, F. G. Sommer, J. E. McNeal, and T. A. Stamey. The abnormal prostate: MR imaging at 1.5 T with histopathologic correlation. *Radiology*, 163(2):521–525, May 1987. 3
- [35] P. Castorina, P. P. Delsanto, and C. Guiot. Classification scheme for phenomenological universalities in growth problems in physics and other sciences. *Phys. Rev. Lett.*, 96:188701, May 2006. 60
- [36] H. P. Chan, B. Sahiner, M. A. Helvie, N. Petrick, M. A. Roubidoux, T. E. Wilson, D. D. Adler, C. Paramagul, J. S. Newman, and S. Sanjay-Gopal. Improvement of radiologists' characterization of mammographic masses by using computer-aided diagnosis: an ROC study. *Radiology*, 212(3):817–827, Sep 1999. 6
- [37] I. Chan, W. Wells, R. V. Mulkern, S. Haker, J. Zhang, K. H. Zou, S. E. Maier, and C. M. Tempany. Detection of prostate cancer by integration of line-scan diffusion, T2-mapping and T2-weighted magnetic resonance imaging; a multichannel statistical classifier. *Med Phys*, 30(9):2390–2398, Sep 2003. 26, 52, 54, 68, 70, 77, 81, 82
- [38] J. Chappelow, B. N. Bloch, N. Rofsky, E. Genega, R. Lenkinski, W. DeWolf, and A. Madabhushi. Elastic registration of multimodal prostate MRI and histology via multiattribute combined mutual information. *Med Phys*, 38(4):2005–2018, Apr 2011. 48, 50

REFERENCES

- [39] J. Chen, J. Yao, and D. Thomasson. Automatic determination of arterial input function for dynamic contrast enhanced mri in tumor assessment. In *International Conference on Medical Image Computing and Computer-Assisted Intervention*, pages 594–601. Springer, 2008. doi: 10.1007/978-3-540-85988-8_71. 107
- [40] L. Chen, Z. Weng, L. Goh, and M. Garland. An efficient algorithm for automatic phase correction of {NMR} spectra based on entropy minimization . *Journal of Magnetic Resonance*, 158(12):164 – 168, 2002. ISSN 1090-7807. 35, 36, 38
- [41] Y. J. Choi, J. K. Kim, N. Kim, K. W. Kim, E. K. Choi, and K. S. Cho. Functional MR imaging of prostate cancer. *Radiographics*, 27:63–75, 2007. 2, 14, 15, 17, 18, 19, 21, 22
- [42] R. Chou, J. M. Croswell, T. Dana, C. Bougatsos, I. Blazina, R. Fu, K. Gleitsmann, H. C. Koenig, C. Lam, A. Maltz, J. B. Rugge, and K. Lin. Screening for prostate cancer: a review of the evidence for the U.S. Preventive Services Task Force. *Ann. Intern. Med.*, 155(11):762–771, Dec 2011. 4
- [43] F. V. Coakley and H. Hricak. Radiologic anatomy of the prostate gland: a clinical approach. *Radiol. Clin. North Am.*, 38:15–30, Jan 2000. 2
- [44] R. J. Cohen, B. A. Shannon, M. Phillips, R. E. Moorin, T. M. Wheeler, and K. L. Garrett. Central zone carcinoma of the prostate gland: a distinct tumor type with poor prognostic features. *J. Urol.*, 179(5):1762–1767, May 2008. 3
- [45] R. Coifman and M. Wickerhauser. Entropy-based algorithms for best basis selection. *Information Theory, IEEE Transactions on*, 38(2):713–718, 1992. ISSN 0018-9448. 61
- [46] T. Coleman and Y. Li. An interior trust region approach for nonlinear minimization subject to bounds. Technical report, Cornell University, 1993. 60

- [47] T. F. Cootes, C. J. Taylor, D. H. Cooper, and J. Graham. Active shape models—Their training and application. *Comput. Vis. Image Underst.*, 61(1):38–59, Jan. 1995. ISSN 1077-3142. 42
- [48] C. Cortes and V. Vapnik. Support-Vector networks. *Machine Learning*, 20(3):273–297, 1995. ISSN 0885-6125. 76
- [49] L. C. Costello and R. B. Franklin. The clinical relevance of the metabolism of prostate cancer; zinc and tumor suppression: connecting the dots. *Mol. Cancer*, 5:17, 2006. 10, 20
- [50] M. Cruz, K. Tsuda, Y. Narumi, Y. Kuroiwa, T. Nose, Y. Kojima, A. Okuyama, S. Takahashi, K. Aozasa, J. O. Barentsz, and H. Nakamura. Characterization of low-intensity lesions in the peripheral zone of prostate on pre-biopsy endorectal coil MR imaging. *Eur Radiol*, 12(2):357–365, Feb 2002. 11
- [51] N. Dalal and B. Triggs. Histograms of oriented gradients for human detection. In *Computer Vision and Pattern Recognition, 2005. CVPR 2005. IEEE Computer Society Conference on*, volume 1, pages 886–893 vol. 1, 2005. 56
- [52] J. G. Daugman. Uncertainty relation for resolution in space, spatial frequency, and orientation optimized by two-dimensional visual cortical filters. *J Opt Soc Am A*, 2(7):1160–1169, Jul 1985. 53
- [53] J. C. Dean and C. C. Ilvento. Improved cancer detection using computer-aided detection with diagnostic and screening mammography: prospective study of 104 cancers. *AJR Am J Roentgenol*, 187(1):20–28, Jul 2006. 6
- [54] N. B. Delongchamps, M. Peyromaure, A. Schull, F. Beuvon, N. Bouazza, T. Flam, M. Zerbib, N. Muradyan, P. Legman, and F. Cornud. Prebiopsy magnetic resonance imaging and prostate cancer detection: comparison of random and targeted biopsies. *J. Urol.*, 189(2):493–499, Feb 2013. 5
- [55] C. Delpierre, S. Lamy, M. Kelly-Irving, F. Molinie, M. Velten, B. Tretarre, A. S. Woronoff, A. Buemi, B. Lapotre-Ledoux, S. Bara, A. V. Guizard,

REFERENCES

- M. Colonna, and P. Grosclaude. Life expectancy estimates as a key factor in over-treatment: the case of prostate cancer. *Cancer Epidemiol.*, 37(4):462–468, Aug 2013. 4
- [56] A. Devos, L. Lukas, J. A. Suykens, L. Vanhamme, A. R. Tate, F. A. Howe, C. Majos, A. Moreno-Torres, M. van der Graaf, C. Arus, and S. Van Huffel. Classification of brain tumours using short echo time ^1H MR spectra. *J. Magn. Reson.*, 170(1):164–175, Sep 2004. 37, 38, 39
- [57] D. L. Donoho and J. M. Johnstone. Ideal spatial adaptation by wavelet shrinkage. *Biometrika*, 81(3):425–455, 1994. 27
- [58] K. W. Doo, D. J. Sung, B. J. Park, M. J. Kim, S. B. Cho, Y. W. Oh, Y. H. Ko, and K. S. Yang. Detectability of low and intermediate or high risk prostate cancer with combined T2-weighted and diffusion-weighted MRI. *Eur Radiol*, 22(8):1812–1819, Aug 2012. 19
- [59] B. Efron. Bootstrap methods: Another look at the jackknife. *The Annals of Statistics*, 7(1):1–26, 01 1979. 73
- [60] B. Efron. Estimating the error rate of a prediction rule: Improvement on cross-validation. *Journal of the American Statistical Association*, 78(382): pp. 316–331, 1983. ISSN 01621459. 82
- [61] J. I. Epstein, W. C. Allsbrook, M. B. Amin, and L. L. Egevad. The 2005 International Society of Urological Pathology (ISUP) Consensus Conference on Gleason Grading of Prostatic Carcinoma. *Am. J. Surg. Pathol.*, 29(9):1228–1242, Sep 2005. 4
- [62] R. Etzioni, D. F. Penson, J. M. Legler, D. di Tommaso, R. Boer, P. H. Gann, and E. J. Feuer. Overdiagnosis due to prostate-specific antigen screening: lessons from U.S. prostate cancer incidence trends. *J. Natl. Cancer Inst.*, 94(13):981–990, Jul 2002. 3

- [63] F. M. Fennessy, A. Fedorov, T. Penzkofer, K. W. Kim, M. S. Hirsch, M. G. Vangel, P. Masry, T. A. Flood, M.-C. Chang, C. M. Tempany, et al. Quantitative pharmacokinetic analysis of prostate cancer dce-mri at 3t: comparison of two arterial input functions on cancer detection with digitized whole mount histopathological validation. *Magnetic resonance imaging*, 33(7):886–894, 2015. doi: 10.1016/j.mri.2015.02.008. 107, 109
- [64] J. Ferlay, H. R. Shin, F. Bray, D. Forman, C. Mathers, and D. M. Parkin. Estimates of worldwide burden of cancer in 2008: GLOBOCAN 2008. *Int. J. Cancer*, 127(12):2893–2917, Dec 2010. 2
- [65] I. Fodor. A survey of dimension reduction techniques, 2002. 64
- [66] A. Fred and A. Jain. Combining multiple clusterings using evidence accumulation. *Pattern Analysis and Machine Intelligence, IEEE Transactions on*, 27(6):835–850, 2005. ISSN 0162-8828. 69
- [67] M. L. Freedman, C. A. Haiman, N. Patterson, G. J. McDonald, A. Tandon, A. Waliszewska, K. Penney, R. G. Steen, K. Ardlie, E. M. John, I. Oakley-Girvan, A. S. Whittemore, K. A. Cooney, S. A. Ingles, D. Altshuler, B. E. Henderson, and D. Reich. Admixture mapping identifies 8q24 as a prostate cancer risk locus in African-American men. *Proc. Natl. Acad. Sci. U.S.A.*, 103(38):14068–14073, Sep 2006. 3
- [68] Y. Freund and R. Schapire. A decision-theoretic generalization of on-line learning and an application to boosting. *Journal of Computer and System Sciences*, 55(1):119 – 139, 1997. ISSN 0022-0000. 71
- [69] J. Friedman. Regularized discriminant analysis. *Journal of the American Statistical Association*, 84(405):pp. 165–175, 1989. ISSN 01621459. 69
- [70] J. Friedman, T. Hastie, and R. Tibshirani. Additive logistic regression: a statistical view of boosting. *Annals of Statistics*, 28:2000, 1998. 72
- [71] D. Gabor. Theory of communication. Part 1: The analysis of information. *Electrical Engineers - Part III: Radio and Communication Engineering, Journal of the Institution of*, 93(26):429–441, 1946. 53

REFERENCES

- [72] S. Ghose, A. Oliver, R. Marti, X. Llado, J. C. Vilanova, J. Freixenet, J. Mitra, D. Sidibe, and F. Meriaudeau. A survey of prostate segmentation methodologies in ultrasound, magnetic resonance and computed tomography images. *Comput Methods Programs Biomed*, 108(1):262–287, Oct 2012. 39
- [73] V. Giannini, A. Vignati, S. Mazzetti, M. De Luca, C. Bracco, M. Stasi, F. Russo, E. Armando, and D. Regge. A prostate CAD system based on multiparametric analysis of DCE T1-w, and DW automatically registered images. In *Proc. SPIE 8670, Medical Imaging 2013: Computer-Aided Diagnosis*, pages 86703E–86703E–6, 2013. 26, 49, 50, 59, 60, 68, 71, 81, 82
- [74] V. Giannini, S. Mazzetti, A. Vignati, F. Russo, E. Bollito, F. Porpiglia, M. Stasi, and D. Regge. A fully automatic computer aided diagnosis system for peripheral zone prostate cancer detection using multi-parametric magnetic resonance imaging. *Computerized Medical Imaging and Graphics*, 46: 219–226, 2015. doi: 10.1016/j.compmedimag.2015.09.001. 109
- [75] P. Gibbs, D. J. Tozer, G. P. Liney, and L. W. Turnbull. Comparison of quantitative T2 mapping and diffusion-weighted imaging in the normal and pathologic prostate. *Magn Reson Med*, 46(6):1054–1058, Dec 2001. 10, 13
- [76] M. L. Giger, H. P. Chan, and J. Boone. Anniversary paper: History and status of CAD and quantitative image analysis: the role of Medical Physics and AAPM. *Med Phys*, 35(12):5799–5820, Dec 2008. 6, 23
- [77] E. Giovannucci, Y. Liu, E. A. Platz, M. J. Stampfer, and W. C. Willett. Risk factors for prostate cancer incidence and progression in the health professionals follow-up study. *Int. J. Cancer*, 121(7):1571–1578, Oct 2007. 3
- [78] G. F. Giskeodegard, H. Bertilsson, K. M. Selnaes, A. J. Wright, T. F. Bathen, T. Viset, J. Halgunset, A. Angelsen, I. S. Gribbestad, and M. B. Tessem. Spermine and citrate as metabolic biomarkers for assessing prostate cancer aggressiveness. *PLoS ONE*, 8(4):e62375, 2013. 10, 20, 21, 22

REFERENCES

- [79] D. F. Gleason. *Urologic pathology: The prostate*, chapter The Veteran's Administration Cooperative Urologic Research Group: histologic grading and clinical staging of prostatic carcinoma, page 171198. Lea and Febiger., 1977. 4
- [80] A. Glioza, S. Mazzetti, P. P. Delsanto, D. Regge, and M. Stasi. Phenomenological universalities: a novel tool for the analysis of dynamic contrast enhancement in magnetic resonance imaging. *Physics in medicine and biology*, 56(3):573, 2011. 99, 100, 109
- [81] S. N. Goodman. Toward evidence-based medical statistics. 1: The P value fallacy. *Ann. Intern. Med.*, 130(12):995–1004, Jun 1999. 62
- [82] I. Gribbestad, K. Gjesdal, G. Nilsen, S. Lundgren, M. Hjelstuen, and A. Jackson. An introduction to dynamic contrast-enhanced MRI in oncology. In A. Jackson, D. Buckley, and G. Parker, editors, *Dynamic Contrast-Enhanced Magnetic Resonance Imaging in Oncology*, Medical Radiology, pages 1–22. Springer Berlin Heidelberg, 2005. ISBN 978-3-540-42322-5. 14, 15
- [83] E. Haacke, R. Brown, M. Thompson, and R. Venkatesan. *Magnetic resonance imaging: Physical principles and sequence design*. Wiley, 1999. ISBN 9780471351283. 20, 21
- [84] G. P. Haas, N. B. Delongchamps, R. F. Jones, V. Chandan, A. M. Serio, A. J. Vickers, M. Jumbelic, G. Threatte, R. Korets, H. Lilja, and G. de la Roza. Needle biopsies on autopsy prostates: sensitivity of cancer detection based on true prevalence. *J. Natl. Cancer Inst.*, 99(19):1484–1489, Oct 2007. 5
- [85] T. Hambrock, D. M. Somford, H. J. Huisman, I. M. van Oort, J. A. Witjes, C. A. Hulsbergen-van de Kaa, T. Scheenen, and J. O. Barentsz. Relationship between apparent diffusion coefficients at 3.0-T MR imaging and Gleason grade in peripheral zone prostate cancer. *Radiology*, 259(2):453–461, May 2011. 10, 19

REFERENCES

- [86] T. Hambrock, P. C. Vos, C. A. Hulsbergen-van de Kaa, J. O. Barentsz, and H. J. Huisman. Prostate cancer: computer-aided diagnosis with multiparametric 3-T MR imaging—effect on observer performance. *Radiology*, 266(2):521–530, Feb 2013. 6
- [87] N. Hara, M. Okuizumi, H. Koike, M. Kawaguchi, and V. Bilim. Dynamic contrast-enhanced magnetic resonance imaging (DCE-MRI) is a useful modality for the precise detection and staging of early prostate cancer. *Prostate*, 62(2):140–147, Feb 2005. 4
- [88] R. Haralick, K. Shanmugam, and I. Dinstein. Textural features for image classification. *Systems, Man and Cybernetics, IEEE Transactions on*, SMC-3 (6):610–621, 1973. ISSN 0018-9472. xiii, 53, 55
- [89] J. V. Hegde, R. V. Mulkern, L. P. Panych, F. M. Fennessy, A. Fedorov, S. E. Maier, and C. M. Tempany. Multiparametric MRI of prostate cancer: an update on state-of-the-art techniques and their performance in detecting and localizing prostate cancer. *J Magn Reson Imaging*, 37(5):1035–1054, May 2013. 6, 11
- [90] A. Heidenreich, P. A. Abrahamsson, W. Artibani, J. Catto, F. Montorsi, H. Van Poppel, M. Wirth, and N. Mottet. Early detection of prostate cancer: European Association of Urology recommendation. *Eur. Urol.*, 64(3):347–354, Sep 2013. 4
- [91] M. Heilmann, F. Kiessling, M. Enderlin, and L. R. Schad. Determination of pharmacokinetic parameters in dce mri: consequence of nonlinearity between contrast agent concentration and signal intensity. *Investigative radiology*, 41 (6):536–543, 2006. doi: 10.1097/01.rli.0000209607.99200.53. 99
- [92] C. M. Hoeks, J. O. Barentsz, T. Hambrock, D. Yakar, D. M. Somford, S. W. Heijmink, T. W. Scheenen, P. C. Vos, H. Huisman, I. M. van Oort, J. A. Witjes, A. Heerschap, and J. J. Futterer. Prostate cancer: multiparametric MR imaging for detection, localization, and staging. *Radiology*, 261(1):46–66, Oct 2011. 4, 5, 11, 14, 15, 16, 17, 21

- [93] R. M. Hoffman, F. D. Gilliland, J. W. Eley, L. C. Harlan, R. A. Stephenson, J. L. Stanford, P. C. Albertson, A. S. Hamilton, W. C. Hunt, and A. L. Potosky. Racial and ethnic differences in advanced-stage prostate cancer: the Prostate Cancer Outcomes Study. *J. Natl. Cancer Inst.*, 93(5):388–395, Mar 2001. 3
- [94] U. Hoffmann, G. Brix, M. V. Knopp, T. Heβ, and W. J. Lorenz. Pharmacokinetic mapping of the breast: a new method for dynamic mr mammography. *Magnetic resonance in medicine*, 33(4):506–514, 1995. doi: 10.1002/mrm.1910330408. 106
- [95] H. Hricak, R. D. Williams, D. B. Spring, K. L. Moon, M. W. Hedgcock, R. A. Watson, and L. E. Crooks. Anatomy and pathology of the male pelvis by magnetic resonance imaging. *AJR Am J Roentgenol*, 141(6):1101–1110, Dec 1983. 6, 10, 11
- [96] H. Hricak, G. C. Dooms, J. E. McNeal, A. S. Mark, M. Marotti, A. Avallone, M. Pelzer, E. C. Proctor, and E. A. Tanagho. MR imaging of the prostate gland: normal anatomy. *AJR Am J Roentgenol*, 148:51–58, Jan 1987. 2, 10, 11
- [97] R. A. Huch Boni, J. A. Boner, U. M. Lutolf, F. Trinkler, D. M. Pestalozzi, and G. P. Krestin. Contrast-enhanced endorectal coil MRI in local staging of prostate carcinoma. *J Comput Assist Tomogr*, 19(2):232–237, 1995. 6
- [98] J. Hugosson, S. Carlsson, G. Aus, S. Bergdahl, A. Khatami, P. Lodding, C. G. Pihl, J. Stranne, E. Holmberg, and H. Lilja. Mortality results from the Göteborg randomised population-based prostate-cancer screening trial. *Lancet Oncol.*, 11(8):725–732, Aug 2010. 4
- [99] H. Huisman, P. Vos, G. Litjens, T. Hambrock, and J. Barentsz. Computer aided detection of prostate cancer using T2, DWI and DCE MRI: methods and clinical applications. In *Proceedings of the 2010 international conference on Prostate cancer imaging: computer-aided diagnosis, prognosis, and intervention*, MICCAI’10, pages 4–14, Berlin, Heidelberg, 2010. Springer-Verlag. ISBN 3-642-15988-5, 978-3-642-15988-6. 43

REFERENCES

- [100] H. J. Huisman, M. R. Engelbrecht, and J. O. Barentsz. Accurate estimation of pharmacokinetic contrast-enhanced dynamic mri parameters of the prostate. *Journal of Magnetic Resonance Imaging*, 13(4):607–614, 2001. doi: 10.1002/jmri.1085. 100, 110
- [101] T. A. Huisman. Diffusion-weighted imaging: basic concepts and application in cerebral stroke and head trauma. *Eur Radiol*, 13(10):2283–2297, Oct 2003. 10, 17
- [102] L. Ibanez, W. Schroeder, L. Ng, and J. Cates. The itk software guide. 2005. 112
- [103] Y. Itou, K. Nakanishi, Y. Narumi, Y. Nishizawa, and H. Tsukuma. Clinical utility of apparent diffusion coefficient (ADC) values in patients with prostate cancer: can ADC values contribute to assess the aggressiveness of prostate cancer? *J Magn Reson Imaging*, 33(1):167–172, Jan 2011. 10, 19
- [104] G. J. Jager, E. T. Ruijter, C. A. van de Kaa, J. J. de la Rosette, G. O. Oosterhof, J. R. Thornbury, S. H. Ruijs, and J. O. Barentsz. Dynamic TurboFLASH subtraction technique for contrast-enhanced MR imaging of the prostate: correlation with histopathologic results. *Radiology*, 203(3):645–652, Jun 1997. 16
- [105] I. T. Jolliffe. *Principal Component Analysis*. Springer, second edition, Oct. 2002. ISBN 0387954422. 64
- [106] M. Jungke, W. Von Seelen, G. Bielke, S. Meindl, M. Grigat, and P. Pfannenstiel. A system for the diagnostic use of tissue characterizing parameters in NMR-tomography. In *Proc. of Information Processing in Medical Imaging*, volume 87, pages 471–481, 1987. 29
- [107] Y. Kaji, J. Kurhanewicz, H. Hricak, D. L. Sokolov, L. R. Huang, S. J. Nelson, and D. B. Vigneron. Localizing prostate cancer in the presence of postbiopsy changes on MR images: role of proton MR spectroscopic imaging. *Radiology*, 206(3):785–790, Mar 1998. 21

- [108] Z. Kato and T. Pong. A Markov random field image segmentation model using combined color and texture features. In W. Skarbek, editor, *Computer Analysis of Images and Patterns*, volume 2124 of *Lecture Notes in Computer Science*, pages 547–554. Springer Berlin Heidelberg, 2001. ISBN 978-3-540-42513-7. 80, 81
- [109] Z. Kato and J. Zerubia. *Markov Random Fields in Image Segmentation. Collection Foundation and Trends in Signal Processing*. Now Editor, World Scientific, Sept. 2012. 81
- [110] B. M. Kelm, B. H. Menze, C. M. Zechmann, K. T. Baudendistel, and F. A. Hamprecht. Automated estimation of tumor probability in prostate magnetic resonance spectroscopic imaging: pattern recognition vs quantification. *Magn Reson Med*, 57(1):150–159, Jan 2007. 26, 37, 40, 50, 60, 68, 70, 73, 75, 77, 81, 82
- [111] S. Kety. The theory and applications of the exchange of inert gas at the lungs and tissues. *Pharmacol. Rev.*, 3(1):1–41, Mar 1951. 15
- [112] J. K. Kim, S. S. Hong, Y. J. Choi, S. H. Park, H. Ahn, C. S. Kim, and K. S. Cho. Wash-in rate on the basis of dynamic contrast-enhanced MRI: usefulness for prostate cancer detection and localization. *J Magn Reson Imaging*, 22(5):639–646, Nov 2005. 16
- [113] A. P. Kirkham, M. Emberton, and C. Allen. How good is MRI at detecting and characterising cancer within the prostate? *Eur. Urol.*, 50(6):1163–1174, Dec 2006. 11, 19
- [114] R. Kirsch. Computer determination of the constituent structure of biological images . *Computers and Biomedical Research*, 4(3):315 – 328, 1971. ISSN 0010-4809. 52
- [115] D. M. Koh and D. J. Collins. Diffusion-weighted MRI in the body: applications and challenges in oncology. *AJR Am J Roentgenol*, 188(6):1622–1635, Jun 2007. 16, 17

REFERENCES

- [116] J. Kurhanewicz, D. B. Vigneron, H. Hricak, P. Narayan, P. Carroll, and S. J. Nelson. Three-dimensional H-1 MR spectroscopic imaging of the in situ human prostate with high (0.24-0.7-cm3) spatial resolution. *Radiology*, 198(3):795–805, Mar 1996. 6
- [117] D. L. Langer, T. H. van der Kwast, A. J. Evans, J. Trachtenberg, B. C. Wilson, and M. A. Haider. Prostate cancer detection with multi-parametric MRI: logistic regression analysis of quantitative T2, diffusion-weighted imaging, and dynamic contrast-enhanced MRI. *J Magn Reson Imaging*, 30(2):327–334, Aug 2009. 26, 52, 59, 68, 82, 86
- [118] T. R. Langerak, U. A. van der Heide, A. N. Kotte, M. A. Viergever, M. van Vulpen, and J. P. Pluim. Label fusion in atlas-based segmentation using a selective and iterative method for performance level estimation (simple). *IEEE Transactions on Medical Imaging*, 29(12):2000–2008, 2010. 42
- [119] H. B. Larsson, T. Fritz-Hansen, E. Rostrup, L. Sondergaard, P. Ring, and O. Henriksen. Myocardial perfusion modeling using MRI. *Magn Reson Med*, 35(5):716–726, May 1996. 15
- [120] T. Laudadio, N. Mastronardi, L. Vanhamme, P. V. Hecke, and S. V. Huf-fel. Improved Lanczos algorithms for blackbox {MRS} data quantitation. *Journal of Magnetic Resonance*, 157(2):292 – 297, 2002. ISSN 1090-7807. 37
- [121] D. Le Bihan, E. Breton, D. Lallemand, P. Grenier, E. Cabanis, and M. Laval-Jeantet. MR imaging of intravoxel incoherent motions: application to diffusion and perfusion in neurologic disorders. *Radiology*, 161(2):401–407, Nov 1986. 18
- [122] D. Le Bihan, E. Breton, D. Lallemand, M. L. Aubin, J. Vignaud, and M. Laval-Jeantet. Separation of diffusion and perfusion in intravoxel incoherent motion MR imaging. *Radiology*, 168(2):497–505, Aug 1988. 16
- [123] K. H. Leissner and L. E. Tisell. The weight of the human prostate. *Scand. J. Urol. Nephrol.*, 13(2):137–142, 1979. 1

- [124] G. Lemaître. Absolute quantification at 3 T. Master's thesis, Université de Bourgogne, Heriot-Watt University, Universitat de Girona, 2011. 21, 22
- [125] G. Lemaitre. lemaitre-2016-nov: 0.1.1, Sept. 2016. URL <http://dx.doi.org/10.5281/zenodo.611612>. 112
- [126] G. Lemaitre, R. Marti, J. Freixenet, J. C. Vilanova, P. M. Walker, and F. Meriaudeau. Computer-aided detection and diagnosis for prostate cancer based on mono and multi-parametric mri: A review. *Computers in Biology and Medicine*, 60:8–31, 2015. 99, 106, 115
- [127] G. Lemaitre, M. R. Dastjerdi, J. Massich, J. C. Vilanova, P. M. Walker, J. Freixenet, A. Meyer-Baese, F. Mériudeau, and R. Marti. Normalization of t2w-mri prostate images using rician a priori. In *SPIE Medical Imaging*, pages 978529–978529. International Society for Optics and Photonics, 2016. doi: 10.1117/12.2216072. 101
- [128] G. Lemaitre, R. Martí, and F. Meriaudeau. DCE-MRI prostate images, Aug. 2016. URL <http://dx.doi.org/10.5281/zenodo.61163>. 112
- [129] F. Li, M. Aoyama, J. Shiraishi, H. Abe, Q. Li, K. Suzuki, R. Engelmann, S. Sone, H. Macmahon, and K. Doi. Radiologists' performance for differentiating benign from malignant lung nodules on high-resolution CT using computer-estimated likelihood of malignancy. *AJR Am J Roentgenol*, 183(5):1209–1215, Nov 2004. 6
- [130] H. Li, M. L. Giger, O. I. Olopade, A. Margolis, L. Lan, and M. R. Chinander. Computerized texture analysis of mammographic parenchymal patterns of digitized mammograms. *Acad Radiol*, 12(7):863–873, Jul 2005. 42
- [131] Q. Li, S. Sone, and K. Doi. Selective enhancement filters for nodules, vessels, and airway walls in two- and three-dimensional CT scans. *Med Phys*, 30(8):2040–2051, Aug 2003. 51
- [132] S. Z. Li. Robustizing robust M-estimation using deterministic annealing. *Pattern Recognition*, 29:159–166, 1996. 30

REFERENCES

- [133] C. A. Lieber and A. Mahadevan-Jansen. Automated method for subtraction of fluorescence from biological Raman spectra. *Appl Spectrosc*, 57(11):1363–1367, Nov 2003. 37, 38
- [134] G. P. Liney, A. J. Knowles, D. J. Manton, L. W. Turnbull, S. J. Blackband, and A. Horsman. Comparison of conventional single echo and multi-echo sequences with a fast spin-echo sequence for quantitative T2 mapping: application to the prostate. *J Magn Reson Imaging*, 6(4):603–607, 1996. 13
- [135] G. P. Liney, M. Lowry, L. W. Turnbull, D. J. Manton, A. J. Knowles, S. J. Blackband, and A. Horsman. Proton MR T2 maps correlate with the citrate concentration in the prostate. *NMR Biomed*, 9(2):59–64, Apr 1996. 10, 11, 13
- [136] G. P. Liney, L. W. Turnbull, M. Lowry, L. S. Turnbull, A. J. Knowles, and A. Horsman. In vivo quantification of citrate concentration and water T2 relaxation time of the pathologic prostate gland using ¹H MRS and MRI. *Magn Reson Imaging*, 15(10):1177–1186, 1997. 10, 11
- [137] G. Litjens, O. Debats, W. van de Ven, N. Karssemeijer, and H. Huisman. A pattern recognition approach to zonal segmentation of the prostate on MRI. *Med Image Comput Comput Assist Interv*, 15(Pt 2):413–420, 2012. 41
- [138] G. Litjens, O. Debats, J. Barentsz, N. Karssemeijer, and H. Huisman. Computer-aided detection of prostate cancer in MRI. *Medical Imaging, IEEE Transactions on*, 33(5):1083–1092, May 2014. ISSN 0278-0062. 26, 41, 42, 50, 68, 72, 73, 81, 85, 86, 115
- [139] G. Litjens, R. Toth, W. van de Ven, C. Hoeks, S. Kerkstra, B. van Ginneken, G. Vincent, G. Guillard, N. Birbeck, J. Zhang, R. Strand, F. Malmberg, Y. Ou, C. Davatzikos, M. Kirschner, F. Jung, J. Yuan, W. Qiu, Q. Gao, P. E. Edwards, B. Maan, F. van der Heijden, S. Ghose, J. Mitra, J. Dowling, D. Barratt, H. Huisman, and A. Madabhushi. Evaluation of prostate segmentation algorithms for MRI: the PROMISE12 challenge. *Med Image Anal*, 18(2):359–373, Feb 2014. 42

- [140] G. J. S. Litjens, P. C. Vos, J. O. Barentsz, N. Karssemeijer, and H. J. Huisman. Automatic computer aided detection of abnormalities in multi-parametric prostate MRI. In *Proc. SPIE 7963, Medical Imaging 2011: Computer-Aided Diagnosis*, pages 79630T–79630T–7, 2011. 26, 41, 43, 50, 51, 54, 68, 77, 81, 82, 85
- [141] G. J. S. Litjens, J. O. Barentsz, N. Karssemeijer, and H. J. Huisman. Automated computer-aided detection of prostate cancer in MR images: from a whole-organ to a zone-based approach. In *Proc. SPIE 8315, Medical Imaging 2012: Computer-Aided Diagnosis*, pages 83150G–83150G–6, 2012. 26, 41, 50, 51, 54, 56, 67, 68, 77, 81, 82, 86
- [142] P. Liu, S. Wang, B. Turkbey, K. Grant, P. Pinto, P. and Choyke, B. J. Wood, and R. M. Summers. A prostate cancer computer-aided diagnosis system using multimodal magnetic resonance imaging and targeted biopsy labels. In *Proc. SPIE 8670, Medical Imaging 2013: Computer-Aided Diagnosis*, pages 86701G–86701G–6, 2013. 26, 32, 56, 68, 77, 82, 85, 88
- [143] W. Liu, B. Turkbey, J. Senegas, S. Remmele, S. Xu, J. Kruecker, M. Bernardo, B. J. Wood, P. A. Pinto, and P. L. Choyke. Accelerated T2 mapping for characterization of prostate cancer. *Magn Reson Med*, 65(5):1400–1406, May 2011. 10, 11
- [144] X. Liu, D. L. Langer, M. A. Haider, Y. Yang, M. N. Wernick, and I. S. Yetik. Prostate cancer segmentation with simultaneous estimation of Markov random field parameters and class. *IEEE Trans Med Imaging*, 28(6):906–915, Jun 2009. 26, 50, 52, 59, 68, 81, 82
- [145] R. Lopes, A. Ayache, N. Makni, P. Puech, A. Villers, S. Mordon, and N. Bebtouri. Prostate cancer characterization on MR images using fractal features. *Med Phys*, 38(1):83–95, Jan 2011. 26, 28, 40, 50, 54, 57, 68, 72, 77, 82
- [146] G. L. Lu-Yao, P. C. Albertsen, D. F. Moore, W. Shih, Y. Lin, R. S. DiPaola, M. J. Barry, A. Zietman, M. O’Leary, E. Walker-Corkery, and S. L. Yao. Outcomes of localized prostate cancer following conservative management. *JAMA*, 302(11):1202–1209, Sep 2009. 3

REFERENCES

- [147] D. Lv, X. Guo, X. Wang, J. Zhang, and J. Fang. Computerized characterization of prostate cancer by fractal analysis in MR images. *J Magn Reson Imaging*, 30(1):161–168, Jul 2009. 26, 31, 33, 40, 57, 67, 68, 82, 92
- [148] R. W. Ma and K. Chapman. A systematic review of the effect of diet in prostate cancer prevention and treatment. *J Hum Nutr Diet*, 22(3):187–199, Jun 2009. 3
- [149] A. Madabhushi and J. K. Udupa. New methods of MR image intensity standardization via generalized scale. *Med Phys*, 33(9):3426–3434, Sep 2006. 34
- [150] A. Madabhushi, J. Udupa, and A. Souza. Generalized scale: Theory, algorithms, and application to image inhomogeneity correction . *Computer Vision and Image Understanding*, 101(2):100 – 121, 2006. ISSN 1077-3142. 31
- [151] J. B. Maintz and M. A. Viergever. A survey of medical image registration. *Med Image Anal*, 2(1):1–36, Mar 1998. 45
- [152] S. Mallat. *A wavelet tour of signal processing, Third Edition: The sparse way*. Academic Press, 3rd edition, 2008. ISBN 0123743702, 9780123743701. 28
- [153] J. V. Manjon, J. Carbonell-Caballero, J. J. Lull, G. Garcia-Marti, L. Marti-Bonmati, and M. Robles. MRI denoising using non-local means. *Med Image Anal*, 12(4):514–523, Aug 2008. 27
- [154] L. Matulewicz, J. F. Jansen, L. Bokacheva, H. A. Vargas, O. Akin, S. W. Fine, A. Shukla-Dave, J. A. Eastham, H. Hricak, J. A. Koutcher, and K. L. Zakian. Anatomic segmentation improves prostate cancer detection with artificial neural networks analysis of ^1H magnetic resonance spectroscopic imaging. *Journal of Magnetic Resonance Imaging*, pages n/a–n/a, 2013. ISSN 1522-2586. 26, 39, 41, 50, 56, 60, 68, 79, 82

- [155] S. Mazzetti, M. De Luca, C. Bracco, A. Vignati, V. Giannini, M. Stasi, F. Russo, E. Armando, S. Agliozzo, and D. Regge. A CAD system based on multi-parametric analysis for cancer prostate detection on DCE-MRI. In *Proc. SPIE 7963, Medical Imaging 2011: Computer-Aided Diagnosis*, pages 79633Q–79633Q–7, 2011. 26, 50, 59, 60, 68, 71, 81, 82
- [156] J. E. McNeal. The zonal anatomy of the prostate. *Prostate*, 2:35–49, 1981. 2
- [157] J. E. McNeal, E. A. Redwine, F. S. Freiha, and T. A. Stamey. Zonal distribution of prostatic adenocarcinoma. Correlation with histologic pattern and direction of spread. *Am. J. Surg. Pathol.*, 12(12):897–906, Dec 1988. 3
- [158] R. Meng, S. D. Chang, E. C. Jones, S. L. Goldenberg, and P. Kozlowski. Comparison between population average and experimentally measured arterial input function in predicting biopsy results in prostate cancer. *Academic radiology*, 17(4):520–525, 2010. doi: 10.1016/j.acra.2009.11.006. 107, 109
- [159] C. E. Metz. Receiver operating characteristic analysis: a tool for the quantitative evaluation of observer performance and imaging systems. *J Am Coll Radiol*, 3(6):413–422, Jun 2006. 83
- [160] J. Mitra. *Multimodal image registration applied to magnetic resonance and ultrasound prostatic images*. PhD thesis, Universitat de Girona and Université de Bourgogne, 2012. 48
- [161] J. Mitra, R. Marti, A. Oliver, X. Llado, J. C. Vilanova, and F. Meriaudeau. A comparison of thin-plate splines with automatic correspondences and B-splines with uniform grids for multimodal prostate registration. In *Society of Photo-Optical Instrumentation Engineers (SPIE) Conference Series*, volume 7964 of *Society of Photo-Optical Instrumentation Engineers (SPIE) Conference Series*, Mar. 2011. 46
- [162] J. Mitra, Z. Kato, R. Marti, A. Oliver, X. Llado, D. Sidibe, S. Ghose, J. C. Vilanova, J. Comet, and F. Meriaudeau. A spline-based non-linear diffeomorphism for multimodal prostate registration. *Med Image Anal*, 16(6):1259–1279, Aug 2012. 46

REFERENCES

- [163] J. Mohan, V. Krishnaveni, and Y. Guo. A survey on the magnetic resonance image denoising methods. *Biomedical Signal Processing and Control*, 9(0): 56 – 69, 2014. ISSN 1746-8094. 27
- [164] C. M. Moore, A. Ridout, and M. Emberton. The role of MRI in active surveillance of prostate cancer. *Curr Opin Urol*, 23(3):261–267, May 2013. 5
- [165] R. Morgan, A. Boxall, A. Bhatt, M. Bailey, R. Hindley, S. Langley, H. C. Whitaker, D. E. Neal, M. Ismail, H. Whitaker, N. Annels, A. Michael, and H. Pandha. Engrailed-2 (EN2): a tumor specific urinary biomarker for the early diagnosis of prostate cancer. *Clin. Cancer Res.*, 17(5):1090–1098, Mar 2011. 5
- [166] E. Niaf, O. Rouvire, and C. Lartizien. Computer-aided diagnosis for prostate cancer detection in the peripheral zone via multisequence MRI. In *Proc. SPIE 7963, Medical Imaging 2011: Computer-Aided Diagnosis*, 2011. xi, 26, 34, 39, 40, 41, 52, 53, 56, 59, 61, 62, 64, 67, 68, 70, 71, 77, 81, 82, 87
- [167] E. Niaf, O. Rouviere, F. Mege-Lechevallier, F. Bratan, and C. Lartizien. Computer-aided diagnosis of prostate cancer in the peripheral zone using multiparametric MRI. *Phys Med Biol*, 57(12):3833–3851, Jun 2012. xi, 26, 34, 39, 40, 41, 52, 53, 56, 59, 61, 62, 64, 67, 68, 70, 71, 77, 81, 82, 87
- [168] M. Noguchi, T. A. Stamey, J. E. McNeal, and C. M. Yemoto. Relationship between systematic biopsies and histological features of 222 radical prostatectomy specimens: lack of prediction of tumor significance for men with nonpalpable prostate cancer. *J. Urol.*, 166(1):104–109, Jul 2001. 5
- [169] R. Nowak. Wavelet-based Rician noise removal for magnetic resonance imaging. *Image Processing, IEEE Transactions on*, 8(10):1408–1419, 1999. ISSN 1057-7149. 25, 28
- [170] L. G. Nyul and J. K. Udupa. On standardizing the MR image intensity scale. *Magn Reson Med*, 42(6):1072–1081, Dec 1999. 32

- [171] L. G. Nyul, J. K. Udupa, and X. Zhang. New variants of a method of MRI scale standardization. *IEEE Trans Med Imaging*, 19(2):143–150, Feb 2000. xi, 33, 92
- [172] T. Ojala, M. Pietikäinen, and D. Harwood. A comparative study of texture measures with classification based on featured distributions. *Pattern Recognition*, 29(1):51–59, Jan. 1996. ISSN 00313203. 42, 56
- [173] M. Osorio-Garcia, A. Croitor Sava, D. M. Sima, F. Nielsen, U. Himmelreich, and S. Van Huffel. *Magnetic Resonance Spectroscopy*, chapter Quantification improvements of ^1H MRS Signals, pages 1–27. InTech, March 2012. 35, 37, 38
- [174] G. Oster, L. Lamerato, A. G. Glass, K. E. Richert-Boe, A. Lopez, K. Chung, A. Richhariya, T. Dodge, G. G. Wolff, A. Balakumaran, and J. Edelsberg. Natural history of skeletal-related events in patients with breast, lung, or prostate cancer and metastases to bone: a 15-year study in two large US health systems. *Support Care Cancer*, 21(12):3279–3286, Dec 2013. 3
- [175] S. Ozer, M. Haider, D. L. Langer, T. H. Van der Kwast, A. Evans, M. Wernick, J. Trachtenberg, and I. Yetik. Prostate cancer localization with multispectral MRI based on Relevance Vector Machines. In *Biomedical Imaging: From Nano to Macro, 2009. ISBI '09. IEEE International Symposium on*, pages 73–76, 2009. 26, 27, 32, 39, 40, 41, 50, 59, 68, 77, 81, 82, 91
- [176] S. Ozer, D. L. Langer, X. Liu, M. A. Haider, T. H. van der Kwast, A. J. Evans, Y. Yang, M. N. Wernick, and I. S. Yetik. Supervised and unsupervised methods for prostate cancer segmentation with multispectral MRI. *Med Phys*, 37(4):1873–1883, Apr 2010. 26, 27, 32, 39, 40, 41, 50, 59, 68, 77, 81, 82, 85, 91
- [177] A. R. Padhani. Dynamic contrast-enhanced MRI in clinical oncology: current status and future directions. *J Magn Reson Imaging*, 16(4):407–422, Oct 2002. 14

REFERENCES

- [178] A. R. Padhani. Integrating multiparametric prostate MRI into clinical practice. *Cancer Imaging*, 11 Spec No A:27–37, 2011. 18
- [179] S. Parfait. *Classification de spectres et recherche de biomarqueurs en spectroscopie par résonnance magnétique nucléaire du proton dans les tumeurs prostatiques*. PhD thesis, Université de Bourgogne, 2010. 1, 2, 4, 20, 21
- [180] S. Parfait, P. Walker, G. Change, X. Tizon, and J. Mitran. Classification of prostate magnetic resonance spectra using Support Vector Machine . *Biomedical Signal Processing and Control*, 7(5):499 – 508, 2012. ISSN 1746-8094. 26, 35, 37, 38, 39, 40, 50, 60, 68, 77, 79, 81, 82
- [181] G. J. Parker, C. Roberts, A. Macdonald, G. A. Buonaccorsi, S. Cheung, D. L. Buckley, A. Jackson, Y. Watson, K. Davies, and G. C. Jayson. Experimentally-derived functional form for a population-averaged high-temporal-resolution arterial input function for dynamic contrast-enhanced mri. *Magnetic resonance in medicine*, 56(5):993–1000, 2006. doi: 10.1002/mrm.21066. 109
- [182] K. Pearson. On lines and planes of closest fit to systems of points in space. *Philosophical Magazine*, 2(6):559–572, 1901. 42
- [183] H. Peng, F. Long, and C. Ding. Feature selection based on mutual information criteria of max-dependency, max-relevance, and min-redundancy. *Pattern Analysis and Machine Intelligence, IEEE Transactions on*, 27(8):1226–1238, 2005. ISSN 0162-8828. 63
- [184] Y. Peng, Y. Jiang, C. Yang, J. Brown, T. Antic, I. Sethi, C. Schmid-Tannwald, M. Giger, S. Eggener, and A. Oto. Quantitative analysis of multiparametric prostate MR images: differentiation between prostate cancer and normal tissue and correlation with Gleason score—a computer-aided diagnosis development study. *Radiology*, 267(1):787–796, June 2013. 10, 19, 26, 54, 56, 68, 77, 81, 82, 86
- [185] N. Petrick, M. Haider, R. M. Summers, S. C. Yeshwant, L. Brown, E. M. Iuliano, A. Louie, J. R. Choi, and P. J. Pickhardt. CT colonography with

- computer-aided detection as a second reader: observer performance study. *Radiology*, 246(1):148–156, Jan 2008. 6
- [186] W. Pijnappel, A. van den Boogaart, R. de Beer, and D. van Ormondt. SVD-based quantification of magnetic resonance signals . *Journal of Magnetic Resonance (1969)*, 97(1):122 – 134, 1992. ISSN 0022-2364. 37
- [187] A. Pizurica. *Image denoising using wavelets and spatial context modeling*. PhD thesis, Universiteit Gent, 2002. 28
- [188] A. Pizurica, W. Philips, I. Lemahieu, and M. Acheroy. A versatile wavelet domain noise filtration technique for medical imaging. *IEEE Trans Med Imaging*, 22(3):323–331, Mar 2003. 28
- [189] J. Pluim, J. Maintz, and M. Viergever. Mutual-information-based registration of medical images: a survey. *IEEE Transcations on Medical Imaging*, 22(8):986–1004, 2003. 47
- [190] J. Prewitt. *Picture processing and psychohistories*, chapter Object enhancement and extraction. Academic Press, 1970. 52
- [191] S. W. Provencher. Estimation of metabolite concentrations from localized in vivo proton NMR spectra. *Magn Reson Med*, 30(6):672–679, Dec 1993. 60
- [192] P. Puech, N. Betrouni, N. Makni, A. S. Dewalle, A. Villers, and L. Lemaitre. Computer-assisted diagnosis of prostate cancer using DCE-MRI data: design, implementation and preliminary results. *Int J Comput Assist Radiol Surg*, 4(1):1–10, Jan 2009. 26, 39, 41, 67, 68, 70, 81
- [193] J. Quinlan. Induction of decision trees. *Machine Learning*, 1(1):81–106, 1986. ISSN 0885-6125. 72
- [194] J. Quinlan. *C4.5: Programs for machine learning*. Morgan Kaufmann Publishers Inc., San Francisco, CA, USA, 1993. ISBN 1-55860-238-0. 72

REFERENCES

- [195] J. Quinonero-Candela, A. Girard, and C. Rasmussen. Prediction at an Uncertain Input for Gaussian processes and relevance vector machines application to Multiple-Step ahead time-series forecasting. Technical report, DTU Informatics, 2002. 77
- [196] L. E. Quint, J. S. Van Erp, P. H. Bland, S. H. Mandell, E. A. Del Buono, H. B. Grossman, G. M. Glazer, and P. W. Gikas. Carcinoma of the prostate: MR images obtained with body coils do not accurately reflect tumor volume. *AJR Am J Roentgenol*, 156(3):511–516, Mar 1991. 11
- [197] C. Rasmussen and C. Williams. *Gaussian processes for machine learning*. The MIT Press, 2005. ISBN 026218253X. 75
- [198] H. Ratiney, M. Sdika, Y. Coenradie, S. Cavassila, D. van Ormondt, and D. Graveron-Demilly. Time-domain semi-parametric estimation based on a metabolite basis set. *NMR Biomed*, 18(1):1–13, Feb 2005. 60
- [199] I. Rish. An empirical study of the naive Bayes classifier. In *IJCAI 2001 workshop on empirical methods in artificial intelligence*, volume 3, pages 41–46, 2001. 71
- [200] C. Rodriguez, S. J. Freedland, A. Deka, E. J. Jacobs, M. L. McCullough, A. V. Patel, M. J. Thun, and E. E. Calle. Body mass index, weight change, and risk of prostate cancer in the Cancer Prevention Study II Nutrition Cohort. *Cancer Epidemiol. Biomarkers Prev.*, 16(1):63–69, Jan 2007. 3
- [201] A. B. Rosenkrantz, A. Sabach, J. S. Babb, B. W. Matza, S. S. Taneja, and F. M. Deng. Prostate cancer: comparison of dynamic contrast-enhanced MRI techniques for localization of peripheral zone tumor. *AJR Am J Roentgenol*, 201(3):W471–478, Sep 2013. 15
- [202] S. T. Roweis and L. K. Saul. Nonlinear dimensionality reduction by locally linear embedding. *Science*, 290(5500):2323–2326, 2000. 66
- [203] D. Rueckert, L. I. Sonoda, C. Hayes, D. L. Hill, M. O. Leach, and D. J. Hawkes. Nonrigid registration using free-form deformations: application to breast MR images. *IEEE Trans Med Imaging*, 18(8):712–721, Aug 1999. 49

- [204] D. E. Rumelhart, G. E. Hinton, and R. J. Williams. Learning internal representations by error propagation. In J. A. Anderson and E. Rosenfeld, editors, *Neurocomputing: foundations of research*, chapter Learning Internal Representations by Error Propagation, pages 673–695. MIT Press, Cambridge, MA, USA, 1988. ISBN 0-262-01097-6. 79
- [205] Y. Saeys, I. Inza, and P. Larrañaga. A review of feature selection techniques in bioinformatics. *Bioinformatics*, 23(19):2507–2517, 2007. 61
- [206] M. C. Schabel and D. L. Parker. Uncertainty and bias in contrast concentration measurements using spoiled gradient echo pulse sequences. *Physics in medicine and biology*, 53(9):2345, 2008. doi: 10.1088/0031-9155/53/9/010. 108
- [207] J. Scheidler, H. Hricak, D. B. Vigneron, K. K. Yu, D. L. Sokolov, L. R. Huang, C. J. Zaloudek, S. J. Nelson, P. R. Carroll, and J. Kurhanewicz. Prostate cancer: localization with three-dimensional proton MR spectroscopic imaging–clinicopathologic study. *Radiology*, 213(2):473–480, Nov 1999. 21
- [208] J. Scheidler, R. Petsch, U. Muller-Lisse, A. Heuck, and M. Reiser. Echo-planar diffusion-weighted MR imaging of the prostate. In *Proceedings of the 7th Annual Meeting of ISMRM Philadelphia*, page 1103, 1999. 6, 11, 16
- [209] H. P. Schlemmer, J. Merkle, R. Grobholz, T. Jaeger, M. S. Michel, A. Werner, J. Rabe, and G. van Kaick. Can pre-operative contrast-enhanced dynamic MR imaging for prostate cancer predict microvessel density in prostatectomy specimens? *Eur Radiol*, 14(2):309–317, Feb 2004. 16
- [210] F. H. Schroder, H. B. Carter, T. Wolters, R. C. van den Bergh, C. Gosselaar, C. H. Bangma, and M. J. Roobol. Early detection of prostate cancer in 2007. Part 1: PSA and PSA kinetics. *Eur. Urol.*, 53(3):468–477, Mar 2008. 4
- [211] F. H. Schröder, J. Hugosson, M. J. Roobol, T. L. Tammela, S. Ciatto, V. Neulen, M. Kwiatkowski, M. Lujan, H. Lilja, M. Zappa, L. J. Denis, F. Recker,

REFERENCES

- A. Pez, L. Määttänen, C. H. Bangma, G. Aus, S. Carlsson, A. Villers, X. Rebillard, T. van der Kwast, P. M. Kujala, B. G. Blijenberg, U.-H. Stenman, A. Huber, K. Taari, M. Hakama, S. M. Moss, H. J. de Koning, and A. Auvinen. Prostate-cancer mortality at 11 years of follow-up. *New England Journal of Medicine*, 366(11):981–990, 2012. 4
- [212] D. Shanbhag, S. N. Gupta, K. Rajamani, Y. Zhu, and R. Mullick. A generalized methodology for detection of vascular input function with dynamic contrast enhanced perfusion data. In *ISMRM*, volume 12, page 10, 2012. 107
- [213] L. G. Shapiro and G. C. Stockman. *Computer vision*. Prentice Hall, Upper Saddle River, NJ, 2001. ISBN 0-13-030796-3. 31
- [214] J. Shi and J. Malik. Normalized cuts and image segmentation. *Pattern Analysis and Machine Intelligence, IEEE Transactions on*, 22(8):888–905, 2000. ISSN 0162-8828. 43, 65
- [215] R. Shimofusa, H. Fujimoto, H. Akamata, K. Motoori, S. Yamamoto, T. Ueda, and H. Ito. Diffusion-weighted imaging of prostate cancer. *J Comput Assist Tomogr*, 29(2):149–153, 2005. 18
- [216] R. Siegel, D. Naishadham, and A. Jemal. Cancer statistics, 2013. *CA Cancer J Clin*, 63(1):11–30, Jan 2013. 3
- [217] J. G. Sled, A. P. Zijdenbos, and A. C. Evans. A nonparametric method for automatic correction of intensity nonuniformity in MRI data. *IEEE Trans Med Imaging*, 17(1):87–97, Feb 1998. 30, 31
- [218] I. Sobel. Camera models and machine perception. Technical report, DTIC Document, 1970. 52
- [219] D. M. Somford, J. J. Futterer, T. Hambrock, and J. O. Barentsz. Diffusion and perfusion MR imaging of the prostate. *Magn Reson Imaging Clin N Am*, 16(4):685–695, Nov 2008. 17

- [220] D. C. Sorensen. Newton's method with a model trust region modification. *SIAM Journal on Numerical Analysis*, 19(2):409–426, 1982. doi: 10.1137/0719026. 109, 111
- [221] D. F. Specht. Probabilistic neural networks for classification, mapping, or associative memory. In *Neural Networks, 1988., IEEE International Conference on*, pages 525–532 vol.1, 1988. 79
- [222] A. Srivastava, E. Klassen, S. Joshi, and I. Jermyn. Shape analysis of elastic curves in euclidean spaces. *Pattern Analysis and Machine Intelligence, IEEE Transactions on*, 33(7):1415–1428, July 2011. 94, 95
- [223] K. S. St Lawrence and T. Y. Lee. An adiabatic approximation to the tissue homogeneity model for water exchange in the brain: I. Theoretical derivation. *J. Cereb. Blood Flow Metab.*, 18(12):1365–1377, Dec 1998. 15
- [224] T. A. Stamey, A. N. Donaldson, C. E. Yemoto, J. E. McNeal, S. Sozen, and H. Gill. Histological and clinical findings in 896 consecutive prostates treated only with radical retropubic prostatectomy: epidemiologic significance of annual changes. *J. Urol.*, 160(6 Pt 2):2412–2417, Dec 1998. 3
- [225] G. D. Steinberg, B. S. Carter, T. H. Beaty, B. Childs, and P. C. Walsh. Family history and the risk of prostate cancer. *Prostate*, 17(4):337–347, 1990. 3
- [226] S. Strum and D. Pogliano. What every doctor who treats male patients should know. PCRI Insights vol. 8, no. 2, May 2005. 3
- [227] M. Styner and G. Gerig. Evaluation of 2D/3D bias correction with 1+1ES-optimization. Technical report, ETH Zürich, 1997. 30
- [228] M. Styner, C. Brechbuhler, G. Szckely, and G. Gerig. Parametric estimate of intensity inhomogeneities applied to MRI. *Medical Imaging, IEEE Transactions on*, 19(3):153–165, 2000. ISSN 0278-0062. 28, 29

REFERENCES

- [229] Y. S. Sung, H. J. Kwon, B. W. Park, G. Cho, C. K. Lee, K. S. Cho, and J. K. Kim. Prostate cancer detection on dynamic contrast-enhanced MRI: computer-aided diagnosis versus single perfusion parameter maps. *AJR Am J Roentgenol*, 197(5):1122–1129, Nov 2011. 26, 50, 59, 68, 77, 82
- [230] M. G. Swanson, D. B. Vigneron, T. K. Tran, N. Sailasuta, R. E. Hurd, and J. Kurhanewicz. Single-voxel oversampled J-resolved spectroscopy of in vivo human prostate tissue. *Magn Reson Med*, 45(6):973–980, Jun 2001. 6
- [231] A. V. Taira, G. S. Merrick, R. W. Galbreath, H. Andreini, W. Taubenslag, R. Curtis, W. M. Butler, E. Adamovich, and K. E. Wallner. Performance of transperineal template-guided mapping biopsy in detecting prostate cancer in the initial and repeat biopsy setting. *Prostate Cancer Prostatic Dis.*, 13(1):71–77, Mar 2010. 5
- [232] M. Tipping. Sparse Bayesian learning and the relevance vector machine. *Journal of Machine Learning Research*, 1:211–244, 2001. 77
- [233] P. Tiwari, A. Madabhushi, and M. Rosen. A hierarchical unsupervised spectral clustering scheme for detection of prostate cancer from magnetic resonance spectroscopy (MRS). *Med Image Comput Comput Assist Interv*, 10(Pt 2):278–286, 2007. 26, 50, 60, 62, 65, 68, 69, 87
- [234] P. Tiwari, M. Rosen, and A. Madabhushi. Consensus-locally linear embedding (C-LLE): application to prostate cancer detection on magnetic resonance spectroscopy. *Med Image Comput Comput Assist Interv*, 11(Pt 2):330–338, 2008. 26, 50, 62, 64, 67, 68, 69, 82, 87
- [235] P. Tiwari, M. Rosen, and A. Madabhushi. A hierarchical spectral clustering and nonlinear dimensionality reduction scheme for detection of prostate cancer from magnetic resonance spectroscopy (MRS). *Med Phys*, 36(9):3927–3939, Sep 2009. 26, 41, 43, 50, 60, 62, 64, 65, 68, 69, 81, 82, 87
- [236] P. Tiwari, M. Rosen, G. Reed, J. Kurhanewicz, and A. Madabhushi. Spectral embedding based probabilistic boosting tree (ScEPTre): classifying high dimensional heterogeneous biomedical data. *Med Image Comput Comput Assist Interv*, 11(Pt 2):339–347, Sep 2008. 26, 50, 62, 64, 67, 68, 69, 82, 87

Assist Interv, 12(Pt 2):844–851, 2009. 26, 50, 52, 53, 54, 60, 62, 65, 74, 81, 82, 86

- [237] P. Tiwari, J. Kurhanewicz, M. Rosen, and A. Madabhushi. Semi supervised multi kernel (SeSMiK) graph embedding: identifying aggressive prostate cancer via magnetic resonance imaging and spectroscopy. *Med Image Comput Comput Assist Interv*, 13(Pt 3):666–673, 2010. 26, 50, 52, 53, 54, 60, 62, 68, 74, 81, 82, 87
- [238] P. Tiwari, S. Viswanath, J. Kurhanewicz, A. Sridhar, and A. Madabhushi. Multimodal wavelet embedding representation for data combination (MaWERiC): integrating magnetic resonance imaging and spectroscopy for prostate cancer detection. *NMR Biomed*, 25(4):607–619, Apr 2012. 26, 38, 40, 50, 53, 57, 61, 64, 68, 73, 74, 77, 81, 82, 86, 87
- [239] P. Tiwari, J. Kurhanewicz, and A. Madabhushi. Multi-kernel graph embedding for detection, Gleason grading of prostate cancer via MRI/MRS. *Med Image Anal*, 17(2):219–235, Feb 2013. 26, 50, 52, 53, 54, 60, 65, 68, 73, 81, 82, 85, 86, 87
- [240] P. Tofts. T1-weighted DCE imaging concepts: modelling, acquisition and analysis. In *Magneton Flash*. Siemens, 2010. 10, 15
- [241] P. S. Tofts. Modeling tracer kinetics in dynamic Gd-DTPA MR imaging. *J Magn Reson Imaging*, 7(1):91–101, 1997. 15, 59
- [242] P. S. Tofts, B. Berkowitz, and M. D. Schnall. Quantitative analysis of dynamic gd-dtpa enhancement in breast tumors using a permeability model. *Magnetic Resonance in Medicine*, 33(4):564–568, 1995. doi: 10.1002/mrm.1910330416. 99
- [243] R. Toth, J. Chappelow, M. Rosen, S. Pungavkar, A. Kalyanpur, and A. Madabhushi. Multi-attribute non-initializing texture reconstruction based active shape model (MANTRA). *Med Image Comput Comput Assist Interv*, 11(Pt 1):653–661, 2008. 42, 46

REFERENCES

- [244] R. Toth, S. Doyle, S. Pungavkar, A. Kalyanpur, and A. Madabhushi. A boosted ensemble scheme for accurate landmark detection for active shape models. In *SPIE Medical Imaging*, volume 7260, Orlando, FL, 2009. 43, 46
- [245] Z. Tu. Probabilistic boosting-tree: learning discriminative models for classification, recognition, and clustering. In *Computer Vision, 2005. ICCV 2005. Tenth IEEE International Conference on*, volume 2, pages 1589–1596 Vol. 2, 2005. 73
- [246] J. D. Tucker, W. Wu, and A. Srivastava. Generative models for functional data using phase and amplitude separation. *Computational Statistics & Data Analysis*, 61:50–66, 2013. 96
- [247] B. Turkbey and P. L. Choyke. Multiparametric MRI and prostate cancer diagnosis and risk stratification. *Curr Opin Urol*, 22(4):310–315, Jul 2012. 9
- [248] M. van der Graaf, R. G. Schipper, G. O. Oosterhof, J. A. Schalken, A. A. Verhofstad, and A. Heerschap. Proton MR spectroscopy of prostatic tissue focused on the detection of spermine, a possible biomarker of malignant behavior in prostate cancer. *MAGMA*, 10(3):153–159, Jul 2000. 10, 20, 21
- [249] C. G. van Niekerk, J. A. van der Laak, M. E. Borger, H. J. Huisman, J. A. Witjes, J. O. Barentsz, and C. A. Hulsbergen-van de Kaa. Computerized whole slide quantification shows increased microvascular density in pT2 prostate cancer as compared to normal prostate tissue. *Prostate*, 69(1):62–69, Jan 2009. 14
- [250] C. G. van Niekerk, J. A. Witjes, J. O. Barentsz, J. A. van der Laak, and C. A. Hulsbergen-van de Kaa. Microvascularity in transition zone prostate tumors resembles normal prostatic tissue. *Prostate*, 73(5):467–475, Apr 2013. 14, 16
- [251] L. Vanhamme, A. van den Boogaart, and S. Van Huffel. Improved method for accurate and efficient quantification of MRS data with use of prior knowledge. *J. Magn. Reson.*, 129:35–45, 1997. 60
- [252] V. Vapnik and A. Lerner. Pattern Recognition using Generalized Portrait Method. *Automation and Remote Control*, 24, 1963. 76

- [253] S. Verma, A. Rajesh, J. J. Futterer, B. Turkbey, T. W. Scheenen, Y. Pang, P. L. Choyke, and J. Kurhanewicz. Prostate MRI and 3D MR spectroscopy: how we do it. *AJR Am J Roentgenol*, 194(6):1414–1426, Jun 2010. 10
- [254] S. Verma, B. Turkbey, N. Muradyan, A. Rajesh, F. Cornud, M. A. Haider, P. L. Choyke, and M. Harisinghani. Overview of dynamic contrast-enhanced MRI in prostate cancer diagnosis and management. *AJR Am J Roentgenol*, 198(6):1277–1288, Jun 2012. 10, 15, 16
- [255] J. C. Vilanova, J. Comet, C. Barceló-Vidal, J. Barceló, E. López-Bonet, A. Maroto, M. Arzoz, À. Moreno, and J. Areal. Peripheral zone prostate cancer in patients with elevated PSA levels and low free-to-total PSA ratio: detection with MR imaging and MR spectroscopy. *Radiology*, 253(1):135–143, 2009. 21
- [256] A. Villers, A. Steg, and L. Boccon-Gibod. Anatomy of the prostate: review of the different models. *Eur. Urol.*, 20:261–268, 1991. 2
- [257] P. Viola and W. M. Wells, III. Alignment by maximization of mutual information. *Int. J. Comput. Vision*, 24(2):137–154, Sept. 1997. ISSN 0920-5691. 48
- [258] S. Viswanath, B. N. Bloch, E. Genega, N. Rofsky, R. Lenkinski, J. Chappelow, R. Toth, and A. Madabhushi. A comprehensive segmentation, registration, and cancer detection scheme on 3 Tesla in vivo prostate DCE-MRI. *Med Image Comput Comput Assist Interv*, 11(Pt 1):662–669, 2008. 26, 41, 42, 49, 50, 52, 53, 54, 57, 60, 62, 69, 82, 87
- [259] S. Viswanath, P. Tiwari, M. Rosen, and A. Madabhushi. A meta-classifier for detecting prostate cancer by quantitative integration of *In Vivo* magnetic resonance spectroscopy and magnetic resonance imaging. In *Medical Imaging 2008: Computer-Aided Diagnosis*, volume 6915. SPIE, 2008. 26, 50, 52, 53, 54, 57, 62, 65, 69, 82, 87
- [260] S. Viswanath, B. N. Bloch, M. Rosen, J. Chappelow, R. Toth, N. Rofsky, R. Lenkinski, E. Genega, A. Kalyanpur, and A. Madabhushi. Integrating

REFERENCES

- structural and functional imaging for computer assisted detection of prostate cancer on multi-protocol in vivo 3 Tesla MRI. In *Society of Photo-Optical Instrumentation Engineers (SPIE) Conference Series*, volume 7260 of *Society of Photo-Optical Instrumentation Engineers (SPIE) Conference Series*, Feb. 2009. 26, 29, 34, 40, 41, 42, 49, 50, 68, 73, 81, 82
- [261] S. Viswanath, B. N. Bloch, J. Chappelow, P. Patel, N. Rofsky, R. Lenkinski, E. Genega, and A. Madabhushi. Enhanced multi-protocol analysis via intelligent supervised embedding (EMPrAvISE): detecting prostate cancer on multi-parametric MRI. In *Proc. SPIE 7963, Medical Imaging 2011: Computer-Aided Diagnosis*, 2011. 26, 34, 40, 41, 49, 50, 52, 53, 54, 62, 66, 68, 74, 80, 81, 82, 85, 86
- [262] S. E. Viswanath, N. B. Bloch, J. C. Chappelow, R. Toth, N. M. Rofsky, E. M. Genega, R. E. Lenkinski, and A. Madabhushi. Central gland and peripheral zone prostate tumors have significantly different quantitative imaging signatures on 3 Tesla endorectal, in vivo T2-weighted MR imagery. *J Magn Reson Imaging*, 36(1):213–224, Jul 2012. 26, 30, 34, 40, 43, 50, 53, 54, 64, 68, 70, 81, 82, 86, 87, 92
- [263] P. C. Vos, T. Hambrock, J. O. Barenstz, and H. J. Huisman. Combining T2-weighted with dynamic MR images for computerized classification of prostate lesions. In *Medical Imaging 2008: Computer-Aided Diagnosis*, volume 6915. SPIE, 2008. 26, 39, 41, 49, 54, 62, 68, 77, 81, 82
- [264] P. C. Vos, T. Hambrock, C. A. Hulsbergen-van de Kaa, J. J. Futterer, J. O. Barentsz, and H. J. Huisman. Computerized analysis of prostate lesions in the peripheral zone using dynamic contrast enhanced MRI. *Med Phys*, 35(3):888–899, Mar 2008. 26, 39, 41, 54, 68, 77, 82
- [265] P. C. Vos, T. Hambrock, J. O. Barenstz, and H. J. Huisman. Computer-assisted analysis of peripheral zone prostate lesions using T2-weighted and dynamic contrast enhanced T1-weighted MRI. *Phys Med Biol*, 55(6):1719–1734, Mar 2010. 26, 41, 49, 51, 54, 68, 77, 81, 82

- [266] P. C. Vos, J. O. Barentsz, N. Karssemeijer, and H. J. Huisman. Automatic computer-aided detection of prostate cancer based on multiparametric magnetic resonance image analysis. *Phys Med Biol*, 57(6):1527–1542, Mar 2012. 26, 41, 43, 50, 51, 54, 62, 63, 68, 70, 77, 81, 82
- [267] U. Vovk, F. Pernus, and B. Likar. A review of methods for correction of intensity inhomogeneity in MRI. *Medical Imaging, IEEE Transactions on*, 26(3):405–421, 2007. ISSN 0278-0062. 29
- [268] P. Walker, G. Crehange, S. Parfait, A. Cochet, P. Maignon, L. Cormier, and F. Brunotte. Absolute quantification in ^1H MRSI of the prostate at 3T. In *ISMRM Annual Meeting 2010*, 2010. 22
- [269] L. Wang, Y. Mazaheri, J. Zhang, N. M. Ishill, K. Kuroiwa, and H. Hricak. Assessment of biologic aggressiveness of prostate cancer: correlation of MR signal intensity with Gleason grade after radical prostatectomy. *Radiology*, 246(1):168–176, Jan 2008. 10, 11
- [270] S. K. Warfield, K. H. Zou, and W. M. Wells. Simultaneous truth and performance level estimation (STAPLE): an algorithm for the validation of image segmentation. *IEEE Trans Med Imaging*, 23(7):903–921, Jul 2004. 41
- [271] M. Wiart, L. Curiel, A. Gelet, D. Lyonnet, J. Y. Chapelon, and O. Rouviere. Influence of perfusion on high-intensity focused ultrasound prostate ablation: a first-pass MRI study. *Magn Reson Med*, 58(1):119–127, Jul 2007. 35
- [272] L. Ye, H. G. Kynaston, and W. G. Jiang. Bone metastasis in prostate cancer: molecular and cellular mechanisms (Review). *Int. J. Mol. Med.*, 20(1):103–111, Jul 2007. 3
- [273] B. Zelhof, M. Lowry, G. Rodrigues, S. Kraus, and L. Turnbull. Description of magnetic resonance imaging-derived enhancement variables in pathologically confirmed prostate cancer and normal peripheral zone regions. *BJU Int.*, 104(5):621–627, Sep 2009. 16

REFERENCES

- [274] G. Zhao, T. Ahonen, J. Matas, and M. Pietikainen. Rotation-Invariant Image and Video Description With Local Binary Pattern Features. *Image Processing, IEEE Transactions on*, 21(4):1465–1477, 2012. ISSN 1057-7149. 56
- [275] H. Zhu, R. Ouwerkerk, and P. B. Barker. Dual-band water and lipid suppression for MR spectroscopic imaging at 3 Tesla. *Magn Reson Med*, 63(6):1486–1492, Jun 2010. 37
- [276] Y. Zhu, M.-C. Chang, and S. Gupta. Automated determination of arterial input function for dce-mri of the prostate. In *SPIE Medical Imaging*, pages 79630W–79630W. International Society for Optics and Photonics, 2011. doi: 10.1117/12.878213. 107
- [277] B. Zitová and J. Flusser. Image registration methods: a survey. *Image and Vision Computing*, 21(11):977 – 1000, 2003. ISSN 0262-8856. 45

Declaration

I herewith declare that I have produced this paper without the prohibited assistance of third parties and without making use of aids other than those specified; notions taken over directly or indirectly from other sources have been identified as such. This paper has not previously been presented in identical or similar form to any other German or foreign examination board.

The thesis work was conducted from XXX to YYY under the supervision of PI at ZZZ.

CITY,